This is to certify that the

dissertation entitled

PHASE TRANSFORMATION IN CARBON COATED TiNi ALLOY, WITH APPLICATION TO THE DESIGN OF A PROSTHESIS FOR THE RECONSTRUCTION OF THE ANTERIOR CRUCIATE LIGAMENT

presented by

ASSEM REDA HEDAYAT

has been accepted towards fulfillment
of the requirements for

Ph.D degree in MATERIALS SCIENCE

Kali Mukherjee
Major professor

Date November 8, 1989

MSU is an Affirmative Action/Equal Opportunity Institution

O-12771

PHASE TRANSFORMATION IN CARBON COATED TiNi ALLOY, WITH APPLICATION TO THE DESIGN OF A PROSTHESIS FOR THE RECONSTRUCTION OF THE ANTERIOR CRUCIATE LIGAMENT

By

ASSEM HEDAYAT

A DISSERTATION

Submitted to Michigan State University
in partial fulfillment of the requirements
for the degree of

DOCTOR OF PHILOSOPHY

Department of Metallurgy, Mechanics, and Materials Science

1989

ABSTRACT

PHASE TRANSFORMATION IN CARBON COATED TiNi ALLOY, WITH APPLICATION TO THE DESIGN OF A PROSTHESIS FOR THE RECONSTRUCTION OF THE ANTERIOR CRUCIATE LIGAMENT

By

Assem Hedayat

The objective of this research is to study the effect of surface constraint on the phase transformation of a near-equiatomic nickel-titanium (50.1 at.% Ni - 49.9 at.% Ti) shape memory alloy, Nitinol. Ultra-low temperature isotropic (ULTI) carbon was vapour deposited on the shape memory alloy as part of a design of a composite prosthesis for the reconstruction of the anterior cruciate ligament.

X-ray diffraction and surface analytical techniques indicated the formation of TiC at the carbon/Nitinol interface. Differential scanning calorimetry studies showed a marked decrease in the austenitic starting (A_s) and the martensitic finishing (M_f) temperatures of the surface constrained alloy during phase transformation. A model that describes this phenomenon is presented.

Cross-sectional specimens of the vapour deposited ULTI carbon on Nitinol substrates were examined with transmission electron microscopy. The phase transformation of the surface constrained Nitinol was studied in-situ. It is proposed that during martensitic transformation, the last

martensite plates to form were close to the constrained surface, and these are first to disappear during reverse transformation. A model to calculate the strain energy associated with the phase transformation of the surface constrained Nitinol is proposed.

The development of the composite prosthesis for the reconstruction of the anterior cruciate ligament required testing of the new material in-vivo. The objective was to study the growth of collagenous tissue on carbon coated Nitinol. Thus, Nitinol filaments on which ULTI carbon was vapour deposited were implanted in canine knees. Scanning electron microscopy examination of the harvested filaments revealed islands of reticular collagen on the surface of the carbon coated filament.

To my mother and to the memory of my father.

ACKNOWLEDGEMENTS

The author would like to express his indebtedness to both his advisors Dr. Kalinath Mukherjee and Dr. James Rechtien for their inspiring guidance and counceling throughout the development of this thesis.

Sincere gratitude is extended to Dr. Terrance Braden for performing the surgery required in this study and for serving as a member of the graduate guidance committee.

Special thanks is expressed to Dr. Dahsin Liu for serving as a member of the guidance committee.

In addition, appreciation is expressed to Mr. Charles Hovey of U.S. Nitinol for supplying the nickel-titanium alloy, and to Dr. Axel Haubold and Mr. Al Beavan of Carbomedics, Inc. for performing the vapour deposition of carbon on the Nitinol substrates.

Thanks also is extended to Ms. Jane Walsh for performing the histological work, and for her unlimited aid throughout the various stages of the experimental work.

Most of all, the author would like to express special recognition and indebtedness to his brother Mr. Sherin Hedayat for his genuine friendship and overwhelming support.

Moreover, the author owes much to his sister Mrs. Amina Khalil, and brother-in-law Dr. Hassan Khalil for their continuous encouragement and sincere advice.

Furthermore, the author wishes to express his appreciation to Ms. Brenda Robinson for the effort she has put into typing this thesis.

Finally, gratitude is expressed to the Composite Materials and Structures Center at Michigan State University for the financial support under account number 91-1006.

TABLE OF CONTENTS

LIST OF TABLES

APPENDIX 1

APPENDIX 2

APPENDIX 3

APPENDIX 4

LIST OF FIGURES

I. INTRODUCTION

The near-equiatomic nickel-titanium alloy, Nitinol, belongs to a class of alloys that exhibits the shape memory effect. This class includes binary alloys like Cu-Zn, Cu-Sn, Au-Cd, Ni-Al, as well as ternary systems such as Cu-Al-Ni, Cu-Zn-Si, and Ni-Ti-Cu [1]. These alloys change their shape repeatedly with heating and cooling. Consequently, they have been used in a variety of applications ranging from aircraft pipe couplings to orthodontic dental arch wires [1].

Of all the shape memory alloys, Nitinol is most commonly used in biomedical applications. This is attributed to the fact that this material fulfills the two requirements of a bio-implantable material, namely biocompatibility and biofunctionability. With regards to biocompatibility, in-vivo testing of Nitinol showed that the material is biologically nontoxic. Not only does its presence fail to generate allergic or carcinogenic responses, there is also no clinical evidence of body rejection or inflammation following its implantation [2]. On the other hand, prosthetic devices made of Nitinol proved to be biofunctionable. This is due to the material's outstanding fatigue and corrosion properties. Fatigue tests showed that while bearing a load equal to four times their yield strength, Nitinol specimens can be cycled thermally or

mechanically for 10^7 cycles without failure. Moreover, Nitinol has an excellent corrosion resistence in saline solutions, and is not susceptible to either stress corrosion or crevice corrosion [2].

The success of Nitinol as a biomaterial, encouraged both engineers and physicians to use it in developing new prosthetic devices. For example, Nitinol is being considered for use in the treatment of scoliosis. A Nitinol Herrington rod is programmed to have bends along its length. Following its insertion, external heat to produce a temperature change of about 3 to 5° C above body temperature could be applied after a few days and periodically thereafter without producing further trauma. The rod gains its undeformed shape, gradually over a period of time, and corrects the spinal deformity without the need for further surgical procedure [1,2]. The same concept is applicable in the area of dentistry where a Nitinol wire could be used as an orthodontic dental arch to straighten out dental malocclusions [1]. Another biomedical application of Nitinol is in the area of orthopedics where Nitinol bone plates for fracture fixation were developed. The advantage of these plates is that they promote rapid healing of the fracture. This is attributed to the fact that when the shape memory effect is triggered by body temperature, the bone plate shrinks to a desired length, and the fractured surfaces are brought together by a compressive load that keeps the fixation rigid [1].

In this research, a new application for Nitinol in the biomedical field is proposed. The alloy will be used in the development of a prosthetic device for the reconstruction of the anterior cruciate ligament. The prosthesis is designed to eliminate the problems associated with an earlier technique that uses carbon fibers for the same application. Carbon fibers were utilized in the other technique because of their ability of bio-conduction of collagenous tissue [3-12]. However, carbon fibers are follicular, extremely brittle, and highly vulnerable to shearing forces. Thus, it is difficult to anchor them to tissues and bones, as they will not tolerate being knotted or stapled. Moreover, not only do fragments of the broken fibers travel to the lymph nodes, but also the process of fragmentation exposes new surfaces of carbon that bio-conduct the growth of more tissue, leading to an uncontrolled growth of the ligament [3].

The prosthesis design suggested in this research, for the reconstruction of the anterior crucite ligament, is mainly made of Nitinol strips and filaments. A new anchoring technique of the prosthesis to the tibia and femur is proposed. The technique is based on the unique property of Nitinol to change its shape with heating and cooling. Moreover, ultra-low temperature isotropic (ULTI) carbon is vapour depositd on the Nitinol filaments to induce the growth of collagenous tissue.

Following the implantation of the prosthesis in the knee joint, the carbon coated filaments will act as a

temporary replacement of the anterior cruciate ligament until growth of the ligament is complete. At this stage, the filaments will be subjected to cyclic loading during physical activities involving the knee joint. The external stresses will cause the Nitinol filaments to experience phase transformation from austenite to martensite. This phenomenon is called stress induced martensite [14]. When the stress is removed, the body temperature will transform the martensite into austenite once again if the austenite finish temperature is less than or equal to 35^{o} C.

Phase transformation of Nitinol has been a subject of great interest to materials scientists. However, none of the studies conducted in this area has dealt with the transformation of surface constrained Nitinol (or other shape memory alloys). It is the the objective of this research to study the effect of surface constraint, represented by a thin (ULTI) carbon film, on the phase transformation of Nitinol. Some preliminary in-vivo canine studies are also conducted with carbon coated TiNi filaments to observe the nature of collagenous tissue growth on them.

II. LITERATURE SURVEY

A. The Anterior Cruciate Ligament

1. Anatomy:

The anterior cruciate ligament is a fibrous connective tissue that links two bones in the knee: the femur and the tibia (Figure 1 and 2) [15]. The ligament originates at the surface of the lateral femoral condyle and inserts 15mm posterior to the anterior edge of the tibial plateau. It is made up of cells called fibrocytes, and is called cruciate because it crosses with the posterior cruciate ligament [16].

The fibers constituting the ligament are not all parallel and longitudinal. Actually, some fibers are arranged spirally. Fibers emerging from the extreme anterior and distal region of the femoral origin insert into the extreme posterolateral region of the tibial attachment. On the other hand, fibers arising from the most posterior and proximal region of the lateral femoral condyle insert into the extreme anterior and medial region of the tibia. The ligament is narrowest at its most proximal region near the femoral origin and fans out as it approaches the tibial attachment. Accordingly, a portion of the anterior cruciate ligament remains taut at all degrees of flexion [16]. Figure

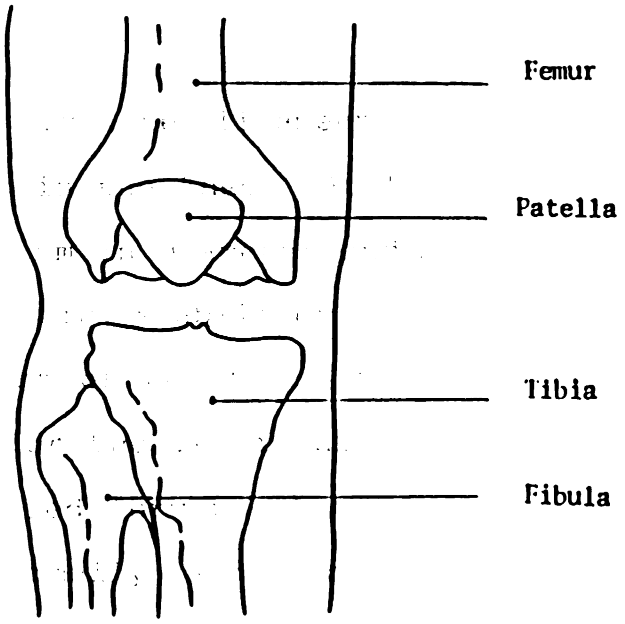

Figure 1. Bones of the knee [15]

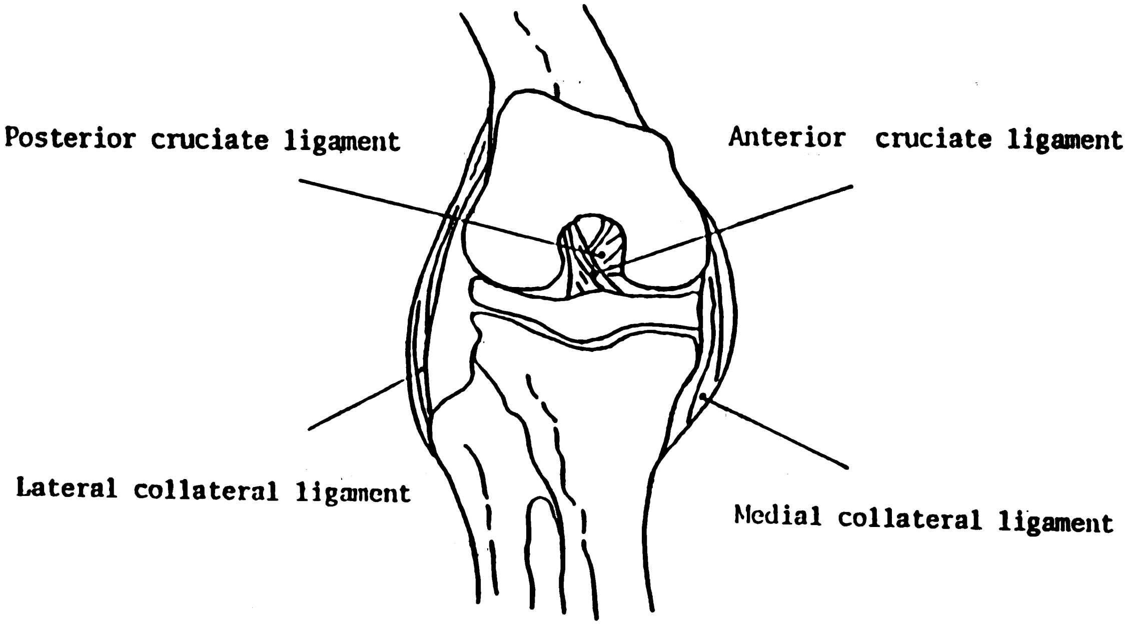

Figure 2. Ligaments of the knee [15]

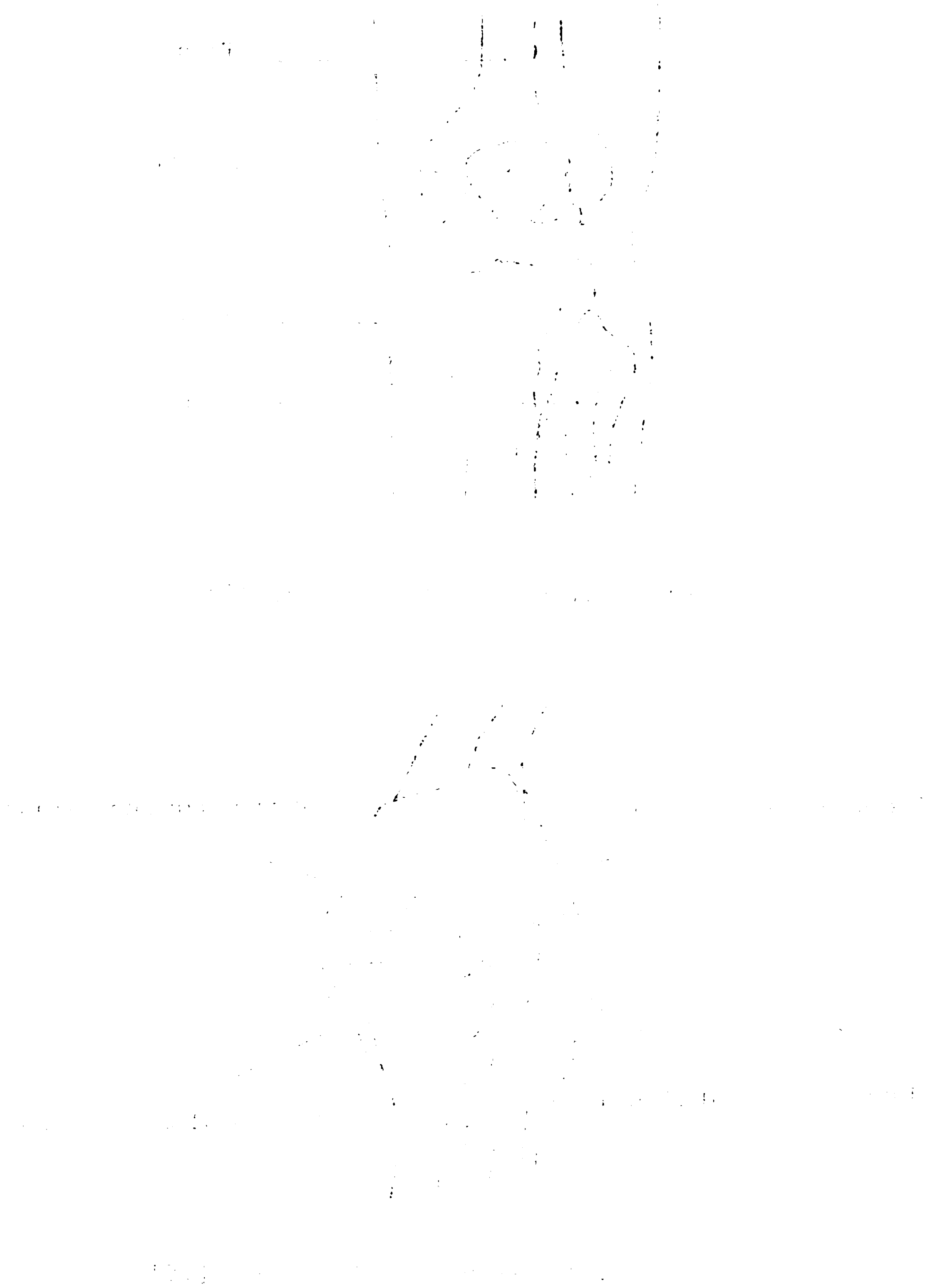

3 is a diagramatic representation of the anterior cruciate ligament during extension and flexion.

2. Function:

The anterior cruciate ligament is one of the most important ligaments in the knee. It has average dimensions of approximately 10 mm in diameter and 40 mm in length, and is the primary static stabilizer of the knee against anterior displacement of the tibia on the femur. Not only is it responsible for the restraining force that keeps the knee from being pulled forward, but also it keeps the knee from rotating abnormally and from being pulled to the outside [16].

3. Biomechanical Properties:

a. Tensile Behavior:

The characteristic tensile load versus extension behavior of the knee ligament is shown in figure 4. Although the elongation is of an elastic nature over a wide range, the elastic line does not pass through the origin. This is attributed to the fact that the fibrous structure of the relaxed ligament does not have all the fibers pulled straight and parallel. Actually, the fibers are buckled into a wavy configuration. Therefore, for a small load, the fibers are being straightened and aligned rather than extended. The application of loads beyond the elastic limit will lead to the deformation and rupture of the ligament

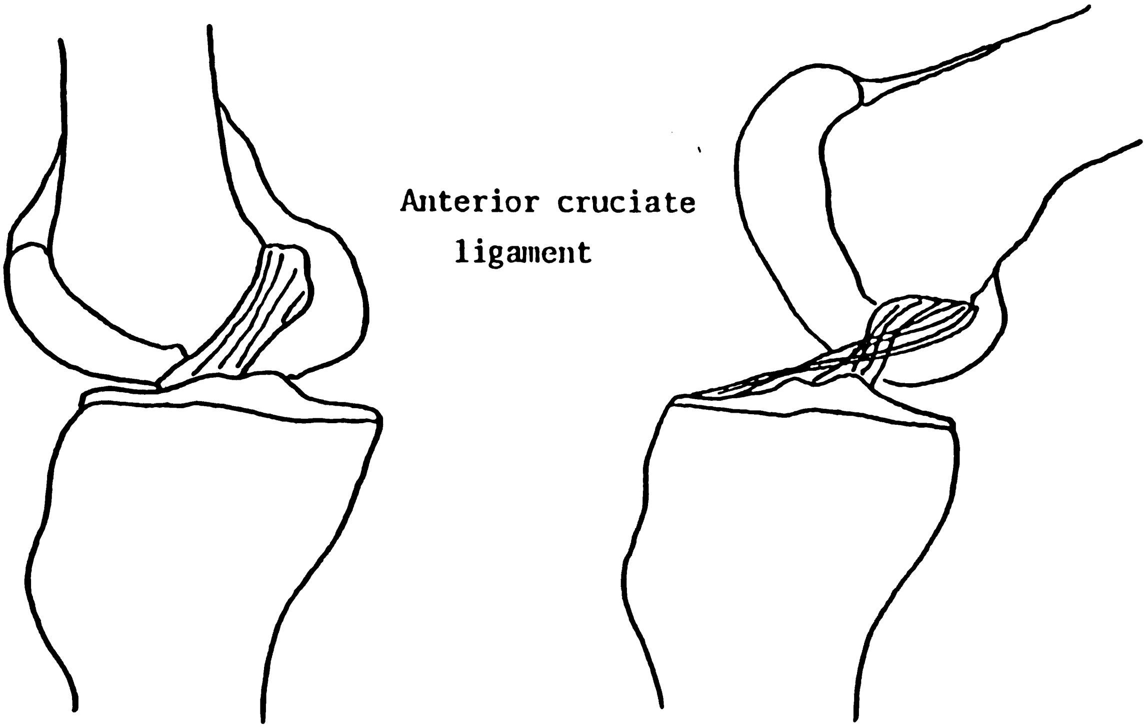

Extension Flexion

Figure 3. Diagramatic representation of the anterior cruciate ligament during extension and flexion [16]

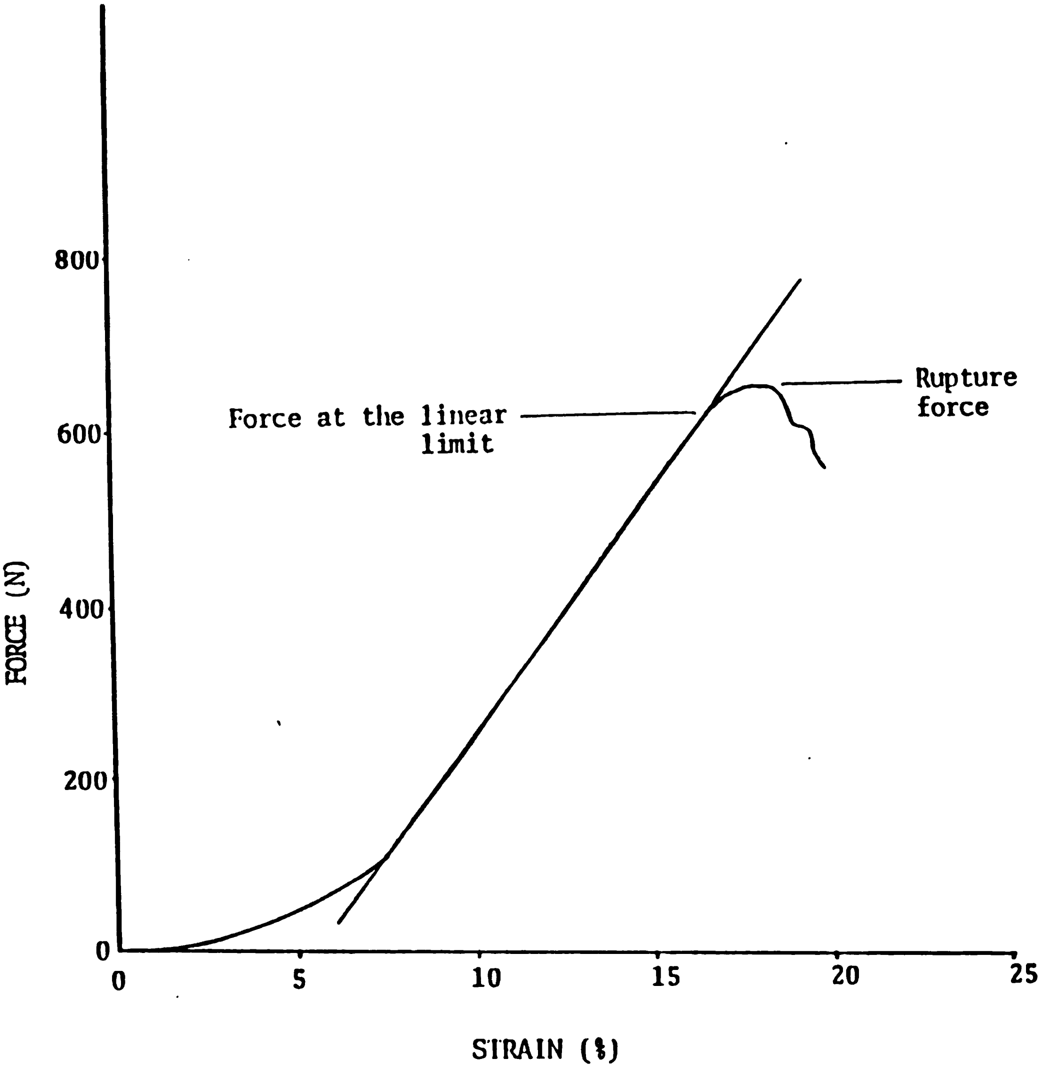

Figure 4. Characteristic force-strain diagram of a tensile test on a human knee ligament [18]

[18].

b. Viscoelastic Effect:

Similar to bones, ligaments exhibit viscoelastic behavior. This behavior is characterized by the dependence of the material properties on time. For example, if a ligament is subjected to a strain which is applied suddenly and held constant, the stress will decrease with time. On the other hand, if the ligament is subjected to a stress which is applied suddenly and held constant, the strain will increase with time [19].

B. Drawbacks of the Available Techniques Used in the Replacement or Reconstruction of the Anterior Cruciate Ligament:

1. Background

The anterior cruciate ligament is an important structure in the knee. Athletes with ruptured anterior cruciate ligaments are usually unable to resume their athletic activities. For some athletes, the anterior cruciate ligament rupture and the knee instability associated with it may prove disabling. This disability may range from the knee catching and giving out with virtually every step, to occasional swelling and pain if any sort of athletics is attempted [15].

There are three major techniques employed in the restoration of the ligament which are: replacement of the ligament using autografts or allografts, ligament

substitution with an artificial polymeric material, and reconstruction of the ligament using carbon fibers. Unfortunately, these methods proved suboptimal due to limitations in both application and design.

a. Replacement of the Anterior Cruciate Ligament Using Autografts and Allografts

The autograft technique [20-23] makes the use of the patient's own fibrous tissue taken from the patellar tendon, or iliotibial band. The harvested fibrous tissue is placed into surgically produced tunnels in the femur and tibia in a geometry consistent with the anterior cruciate function. A more recent approach utilizes allografts of freeze dried cadaver fascia lata or Achilles tendon or, possibly, even anterior cruciate ligament available at tissue banks to replace the ruptured ligament. The autograft technique is suboptimal because the accurate length and position of the reconstruction is difficult to achieve, and even when ideal, the reconstruction might fail for lack of an adequate blood supply [24-26]. Moreover, the structure from which the autograft is taken becomes weaker. An example of that is the patellar tendon of which the middle third is often used as an autograft for the replacement of the anterior cruciate ligament. Experimental studies involving the patellar tendons of canines indicate that the structural stiffness of the remaining two thirds of the tendon was diminished significantly post-surgery [27]. The allograft techniques

are still too new to provide definite failure data but, clearly, these techniques will require significant additional research before becoming an entirely satisfactory solution. One can speculate that they too will lack adequate circulation and will face the same problems that bone replacements from tissue banks encounter with infectious disease transmission [28].

b. Replacement of the Anterior Cruciate Ligament with an Artificial Polymeric Material

Considerable research is being conducted to develop an acceptable artificial ligament. The problem of the anterior cruciate ligament implant design is indeed a challenging one to the bioengineer. The artificial material used should imitate the natural mechanical properties of the biological structure. Not only should the material be biocompatible, but also it should be durable. Furthermore, some form of fixation augmentation by tissue ingrowth must be provided for long-term function. Finally, the prosthetic ligament should possess acceptable mechanical properties which are essential for proper function. Such properties which must be similar to that of the ligament are mainly yield strength, creep, elongation recovery time, fatigue life and modulus of elasticity [29-32].

Several investigators proposed different material design for the prosthetic ligament. Dacron fabrics in either woven, knitted, or velour form were used to replace

the anterior cruciate ligament [33-34]. Bicomponent brands of dacron-kevlar or dacron-lykra were proposed as a new design concept for anterior cruciate ligament replacement. The strength of the braid can be adjusted by the incorporation of chemically different bicomponent materials, the composition of the bicomponents, the helix angle of the sheath, and the core material [35]. Moreover, a composite prosthesis, which consists of a compressible inner core around which a dacron fiber is woven in a helical fashion, was devised to replace the anterior cruciate ligament [36]. It is worth mentioning that artificial prostheses are commercially available. Examples of these prostheses are the Gortex graft [37], and the Richards Polyflex ligament [38].

Long term results of the replacement of the anterior cruciate ligament with an artificial polymeric material are often unsatisfactory. This is attributed to the insufficient strength of the materials, and the variability in placement of the prosthesis. Usually, the artificial ligaments fail by a fatigue mode [39].

c. Reconstruction of the Anterior Cruciate Ligament Using Carbon Fibers

The ideal solution to the reconstruction of the anterior cruciate ligament would be regrowth of the ligament with its required blood supply since the appropriate strength and other properties would be ideal for the

ligament's function. Carbon fibers are known to bioconduct the formation of ligaments and tendons in both humans and animals [3-12] and this has led to numerous research attempts to construct a ligament prosthesis from carbon fibers (Figures 5 and 6). The carbon fibers' supporting function is gradually replaced by new ligament formation which is particularly prolific in the milieu created by the active healing process in the vicinity of the original injury. Carbon, in general, is, among the most biocompatible materials [40], but numerous difficulties have prevented the success of this approach. The fibers are extremely brittle and tend to break off, not only during surgical implantation but also over a period of time, *in vivo*. The latter process produces small fragments which either produce local joint pain or migrate to the regional lymph nodes [12]. The surgical anchoring of the pure carbon fibers is also made difficult by their brittleness and stapling attempts have failed [41]. Excessive ligament regrowth usually occurs producing a new ligament six times the optimal size [19]. Further, the new tissue fibers generated tend to be straight and lack the spiral geometry that allows the natural ligament to remain taut in multiple configurations [3]. Thus, none of the current technologies has produced a well accepted solution to the anterior cruciate ligament injury problem.

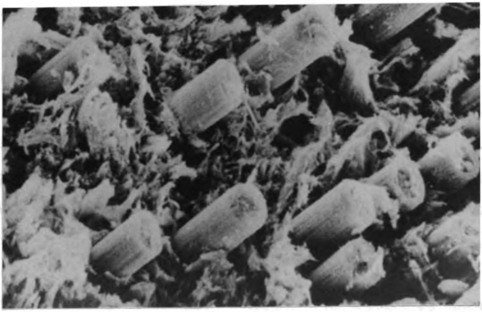

Fig. 5. SEM photomicrograph of collagenous tissue growth around carbon fibers (X 1000) as shown by Weiss, et al., Clin. Orthop. Rel. Res., V. 196, (1985):77 [42]

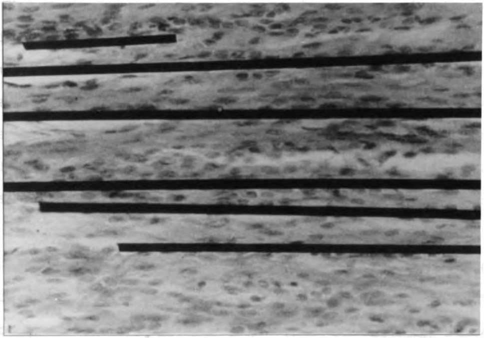

Fig. 6. Light micrograph of a longitudinal section of collagenous tissue growth around carbon fibers (X 120) as shown by Claes, L., et al., Clin. Orthop. Rel. Res., V. 196, (1985):99 [43]

C. The Phase Transformations of Nitinol

1. Introduction

The near-equiatomic nickel-titanium alloy is one that exhibits the shape memory effect. This is a characteristic by which the alloy can change its shape repeatedly, reversibly, and substantially with heating and cooling [1]. The thermal cycling causes phase transformation to proceed from one ordered structure to the other reversibly. This transformation does not take place by diffusional mixing of atoms. Instead, it occurs by shear displacement of crystal segments. Although other alloys like steels undergo diffusionless or martensitic transformations, they do not exhibit the shape memory effect. The reason is that the martensitic transformation in steel is non-thermoelastic [44].

Thermoelastic and non-thermoelastic phase transformation can be contrasted with respect to the mechanisms of transformation as well as the microstructural changes associated with them. In thermoelastic phase transformations, the shape recovery is attributed to the fact that the strain introduced is reversible. Although a shape change takes place, no permanent damage is made on the microstructural scale. As a matter of fact, the microstructure deforms by a mechanism of shearing regions of the parent phase to martensite, or by detwinning within individual martensite plates. These mechanisms are

different from the usual irreversible mechanisms of plastic deformation experienced in non-thermoelastic transformations such as slip and dislocation motion [44]. In shape memory alloys, which exhibit thermoelastic phase transformation, plates of martensite form continuously with cooling. If the cooling is stopped and then resumed, the martensitic plates will continue to grow because the interface between the parent and the martensitic phase is glissile. Growth will only stop when the plates impinge with each other or with grain boundaries. On heating, the plates will shrink and completely revert to the orientation of the parent phase. In the case of non-thermoelastic phase transformation, on the other hand, plates of martensite will also form on cooling. However, they will not grow beyond a certain size because the interface becomes sessile. Moreover, on heating, the plates will not shrink. Instead, the parent phase will nucleate within them and grow by a diffusion process, and the plate as a whole will not revert to the orientation of the parent phase. The mechanism is governed by the kinetics of the reaction, and involves nucleation and growth [45].

The reversibility of thermoelastic martensite is attributed to the inherently low elastic strains associated with the change in the crystal structure of a shape memory alloy. Thus, the elastic limit of the matrix of the parent phase is not exceeded, and irreversible plastic deformation does not take place. Moreover, as the martensite plates

grow, they are arranged in a mutually accommodating fashion, and effectively cancel the distortions so that strains do not accumulate. The martensite plate groups usually consist of simple alternating stacks of platelets where cancellation of strain vectors between neighboring platelets take place. Moreover, the individual martensite plates are internally faulted or twinned to accommodate the strains resulting from the transformation. This is in contrast to non-thermoelastic martensitic transformations in which high inherent strains are associated with the martensitic phase. These strains are too great to be accommodated, and this renders the transformation irreversible [44].

During phase transformation of shape memory alloys, the difference in the chemical free energy between the two phases, which is the driving energy of the transformation, and the elastic energy developed are in balance with each other at all times. The interfacial energy is very small. Consequently, either cooling or application of stress assist the transformation to proceed in one direction, while heating and releasing the stress will reverse it. The mechanical analogue to the athermal (heating-cooling) formation and reversion of martensite in shape memory alloys is known as pseudoelastic behavior. This behavior is characterized by the formation of martensite as the stress increases. When the stress is removed, the transformation reverses along the same microstructural path, and the shape is recovered. Both the shape memory effect and

pseudoelasticity are complimentary to one another. For example, on deforming a shape memory alloy, a fraction of the strain is recovered on unloading (pseudoelastic behavior), and the rest is recovered on heating (shape memory effect) [44].

In Nitinol, the high temperature phase, which is called the austenitic or the parent phase, has the structure of a CsCl ordered lattice. In space group notation, the lattice is denoted by B2, and has the lattice parameter $a = 3.01\ A^{o}$ [46]. The low temperature phase is called martensite. The unit cell of that phase is monoclinic, with the c-axis slightly inclined ($= 97.78^{o}$). For a near-equiatomic TiNi alloy, the unit cell structure has the space group of B19' [47], and the lattice parameters are [64]:

$$a = 2.989\ A^{o}$$

$$b = 4.108\ A^{o}$$

$$c = 4.646\ A^{o}$$

As the phase transformation of Nitinol proceeds in one direction, abrupt changes in the physical properties of the alloy can be observed. These changes include mechanical properties such as the yield strength, Young's modulus and electrical resistivity. While the yield strength and Young's modulus increase with the martensitic transformation [48], electrical resistivity drops [49]. Moreover, the transformation from austenite to martensite is characterized as being exothermic, and the reverse transformation is

endothermic [14]. Thus, several experimental techniques based on the measured changes of these properties are utilized to study the phase transformation of Nitinol and other shape memory alloys. The main parameters used to describe the transformation are the martensitic starting and finishing temperatures as well as the austenite starting and finishing temperatures; M_s, M_f, A_s, and A_f, respectively.

2. The R-Phase

As the transformation proceeds from austenite to martensite, the Nitinol experiences a premartensitic transition just above M_s. The lattice undergoes a rhombohedral distortion which is the reason for referring to the transition as the "R-phase" [50].

The R-phase can be detected in every experimental technique used to study the martensitic transformation of Nitinol. Electrical resistivity tests show an increase in resistivity following thermal cycling of the alloy [49, 51, 52]. In addition, differential scanning calorimetry measurements of thermally cycled Nitinol show the R-phase as a separate exothermic peak just prior to the martensitic peak [53]. Moreover, besides existing as diffuse streaks in x-ray diffraction [46, 54], the R-phase is represented by extra reflections located at one third positions in electron diffraction patterns [52, 55]. Furthermore, the R-phase can be detected also by its anomolous behavior in elasticity

[56, 57], magnetic properties [58], internal friction [57] and heat capacity [59, 60].

The process by which the premartensitic phase, the R-phase, forms is not completely understood. However, efforts were made to interpret the transformation as a charge density wave transition as follows. As the transformation proceeds from the parent phase to the martensitic phase, a periodic lattice distortion occurs giving rise to a three-dimensional charge density wave. This wave forms on two stages. First, an incommensurate transition from the B2 phase occurs with the decrease in temperature. Then, as the temperature is decreased further, the incommensurate phase locks into the commensurate phase, which is the R-phase. While the nomenclature incommensurate refers to a status where the wave length is not a multiple of the lattice parameter, commensurate denotes equality between them. It is worth mentioning that while the transition from the B2 phase to the incommensurate phase is of the second order, that from the incommensurate to the commensurate is of the first order [50].

The R-phase has been studied extensively. Major findings were that the commensurate R-phase corresponds to a rhombohedral lattice with space group notation P31m [63]. Moreover, the history of the material including heat and deformation affects the R-phase. The more residual stress is present in the material, the more pronounced is the R-phase [65]. Furthermore, the R-phase has four distinct

variants or orientations that can be correlated with each other by twinning relationships [50, 66, 67]. These variants are self accommodating and they produce a zero macroscopic strain [66, 67]. This is in contrast to the cubic parent phase to martensite transformation which has 24 variants [68].

3. Thermodynamics of the phase transformations in TiNi alloys

The solid-state martensitic phase transformation in Nitinol is categorized as being athermal. This type of transformation is a function of temperature and not time. The reaction proceeds only with the change in temperature. If the temperature is held constant, the transformation will not proceed with time. Accordingly, shape memory alloys are studied thermodynamically rather than kinetically.

As mentioned earlier, during phase transformation, the chemical free energy between the parent phase and the martensitic phase is in balance at all times with non-chemical energy, such as elastic energy and surface energy [44, 45]. Since the interface between the martensite and the parent phase is coherent in a thermoelastic transformation, the surface energy is small. Thus, the opposing non-chemical energy is mainly the elastic energy. The phase transformation from the parent phase to the martensitic phase, or visa versa, can be represented by the following equation:

$$\Delta G = \Delta G_c + \Delta G_{nc} \qquad (1)$$

where ΔG_c is the chemical free energy or driving energy

and ΔG_{nc} is non-chemical energy.

For a first order phase transformation, a parent phase is in equilibrium with the martensitic phase at an equilibrium temperature T_o. This temperature corresponds to $\Delta G_c = 0$ and is equivalent to $(A_s + M_s)/2$ [69]. For Nitinol and other alloys that undergo thermoelastic transformations, two equilibrium temperatures were suggested. The first denoded by T_o corresponding $\Delta G_c = 0$ and is equivalent to $(M_s + A_f)/2$. The other is T_o' where $\Delta G_c + \Delta G_{nc} = 0$ and is equivalent to $(M_f + A_s)/2$ [70]. Moreover, for unstressed samples, the ratio of non-chemical free energy ΔG_{nc} to the enthalpy of the transformation ΔQ could be estimated using the following formula [71]:

$$\Delta G_{nc}/\Delta Q = (T_o - T_o')/T_o \qquad (2)$$

Similarly, the ratio of energy change ΔG associated with the cooling of an unstressed sample from M_s to M_f, to the change in the entropy of transformation was given as [72]:

$$\Delta G/\Delta S = 1/2\ (M_f - M_s) \qquad (3)$$

where $\Delta S = \Delta Q/M_s$

Differential scanning calorimetry (DSC) and differential thermal analysis (DTA) are two common calorimetric techniques used in studying the phase transformations of shape memory alloys [73-77]. While the first technique measures the difference in energy between the alloy and a reference material as a function of temperature, the latter measures the difference in temperature.

Using the DSC, thermodynamic quantities like enthalpy, heat capacity, and temperatures of transformations could be measured. Thus, it is usually preferred. The entropy of the reaction could also be calculated from DSC data using the relation $\Delta S = \Delta H/T_o$ where T_o is sometimes estimated as the average temperature of A_s and M_s [78] or as the average temperature of A_f and M_s when A_s is below M_s [70]. Selected values of these parameters for a near equiatomic Nitinol are given in Table 1. It is clear that the values may vary although the composition of the alloy and its history might be the same. The variation is attributed to the difference in experimental conditions. The sensitivity of the apparatus used is crucial in thermodynamic measurements. The rate of cooling and heating at which transformation occurs also affects the transformation temperatures [83].

Calorimetric studies of the phase transformation of shape memory alloys using DSC, clarified some of the thermodynamical characteristics of the parent phase to martensite reaction and vice versa. During cooling of

Table 1

Thermodynamic Data of Selected Shape Memory Effect Alloys

System	NiTi							
Composition (atomic %)	49Ni-51Ti	49.8Ni-50.2Ti	50Ni-50Ti	50.1Ni-49.9Ti	50.4Ni-49.6Ti	50.5Ni-49.5Ti	51Ni-49Ti	55Ni-45Ti
Enthalpy of transformation ΔH (j/g)	33.05[79]	29.04[80]	20.08[79] 24.2[78]	19.41[14]	32.1[81]	24.4[81]	24.18[46]	22.1[82]
Average heat capacity C_p (j/g.1)	0.47[79]	——	0.47[78,79]	0.58[14]	——	——	0.483[49]	0.46[82]
Temperature T_o(k) = 1/2 (A_s + M_s)	——	366[80]	290[78] 318[81]	——	308[81]	283.6[81]	——	——
Entropy of transformation ΔS (j/g.k)	——	0.079[80]	0.101[81]	——	0.104[81]	0.086[81]	——	——
Reported density P (g/cm^3)	——	——	6.4[78]	——	——	——	6.45[49]	——
Calculated density P (g/cm^3)	6.48	6.49	6.49	6.49	6.50	6.50	6.50	6.56

Nitinol, as the B2 phase transforms into martensite, two exothermic peaks result. The sum of enthalpy changes of the two peaks is equal to the enthalpy change of the single endothermic peak occurring with the martensite to B2 phase reaction [14]. Moreover, for the thermoelastic transformation of Nitinol, there is a linear relationship between ΔH and $T_o = 1/2\ (A_s + M_s)$ [81]. In addition, the fraction of phase transformed as a function of temperature was given by the formula [84]:

$$f(T) = 1/\Delta H \int_{T}^{M_s, A_f} \partial \Delta H /\ T\ dT \qquad (4)$$

Furthermore, for a surface constrained single crystal of a Cu-Al-Ni alloy undergoing martensitic phase transformation, surface nucleation is inhibited. This results in supercooling to lower temperatures for volume nucleation to take place [85]. Finally, while complete cycling of Nitinol substantially changes the transformation temperatures of the alloy, incomplete cycling does not [86].

D. Vapour Deposition of Thin Carbon Films

Carbon coatings can be prepared by a variety of vacuum processes. These processes include ion plating [87, 88], sputtering [89], and laser evaporation [90]. The structure of the carbon film, and its properties, depend on the technique used in the deposition process. Thus, carbon films with an amorphous, crystalline, diamond like, or turbostratic structures can be prepared [91]. The latter is

a subcrystalline structure in which no order exists between the hexagonal layers of carbon as there is in graphite [92].

Of all the carbon films, those with a turbostratic structure have been singled out to be utilized in biomedical applications. This is attributed to the outstanding biomechanical properties of this class of carbon. The complete randomness of the hexagonal carbon layers render the material strong and tough. This is in comparison to diamond like carbon films which are strong and stiff, and to graphite films which are weak and flexible. Furthermore, cyclic loading does not degrade the strength of turbostratic carbons, and failure does not occur by a fatigue mode [91].

In this research, an ultra-low temperature isotropic (ULTI) carbon is vapour deposited on the Nitinol substrates. The ULTI carbon, which has a turbostratic structure, is known commercially as Biolite$^{(R)}$. It is prepared in a hybrid vacuum process where a carbon-bearing gaseous precursor in the presence of a catalyst is used to deposit impermeable, isotropic carbon at high rates on cold substrates. The advantage of this process is that the deposition is performed at low pressure and ambient temperature. Thus, the carbon can also be deposited on low-melting-point materials such as polymers. During deposition, the density, crystallite size and orientation of the coating can be varied. Moreover, the carbon film is less than one micron thick, and thus doesn't affect the surface topography or the mechanical properties of the substrate [92].

Besides being biocompatible, ULTI carbon (Biolite$^{(R)}$) is not susceptible to fluid friction erosion in either turbulent or laminar flow. This property of the material is indispensable in applications where it is exposed to fluid flow. An example of that type of application is the Biolite$^{(R)}$ coatings applied to heart valves [91].

The adhesion of Biolite$^{(R)}$ to substrates of different materials was investigated. Studies show that Biolite$^{(R)}$ adheres best to carbide forming [88, 93, 94] metallic materials like titanium and stainless steel. For example, the bond strength between biolite and stainless steel was found to be greater than 4700 psi [93]. Auger electron spectroscopy (AES) indicated the formation of titanium carbide at the titanium/Biolite$^{(R)}$ interface [91, 93], and iron carbide at the stainless steel/Biolite$^{(R)}$ interface [88]. Moreover, Biolite$^{(R)}$ bonds well to polyamides. Average bond strengths of 3000 psi were measured between Biolite$^{(R)}$ and vespel which is a polyamide. It was speculated that carbon-carbon type bonding could have occurred between the carbon film and the polyamide substrate [94].

III. MATERIALS AND METHODS

The experimental work in this study was divided into two parts: (1) phase transformation studies of carbon coated TiNi, and (2) a preliminary biologic evaluation of the carbon coated Nitinol. The materials research focused mainly on the effect of surface constraint, represented by a thin film of ULTI carbon, on the phase transformation of Nitinol. The biological study, on the other hand, involved actual implantation of the composite material in a canine's knee. The objective of the implantation was to evaluate the growth of fibroblasts, the constituent cells of collagen, on the carbon coated filaments. The results from both studies could possibly generate a design of a prosthetic device for the replacement of the anterior cruciate ligament.

A. Materials Analysis

1. Materials

a. Nitinol

A near-equiatomic nickel-titanium (50.1 at % Ni - 49.9 at % Ti) shape memory alloy, Nitinol, was supplied by the U.S. Nitinol, Saratoga, California. The alloy was produced in the plate form, 2.5 mm thick, as well as in filament form, 0.076 and 0.0152 mm in diameter. While Nitinol in the plate form was used in the materials research, the Nitinol filaments were used in the biological study.

b. Ultra-Low Temperature Isotropic (ULTI) Carbon

The ULTI carbon, which has the commercial name of Biolite$^{(R)}$, was vapour deposited on the Nitinol substrates at Carbomedics, Inc., Austin, Texas at a low pressure in a hybrid process. A catalyst was used to deposit the biolite at high rates from a carbon-bearing gaseous precursor, and the temperature of the substrate was about 80^{o}C. Thus, the carbon was vapour deposited on austenitic Nitinol. Two thicknesses of carbon films were applied to two different batches of Nitinol samples. The film thicknesses were 1500 A^{o} and 3000 A^{o}.

2. Methods

a. Film Thickness Measurements

Film thickness measurements were done using a Dektak IIA surface profile analyzer. Among every batch of Nitinol substrates to be carbon coated, there was one specimen that was partly covered with a heat resistant plastic tape. Following vapour deposition, the plastic tape was removed, creating a step between the coated and uncoated areas of the sample. The surface profile analyzer measured the thickness of that step which was actually the thickness of the carbon film. The measurements showed that the thicknesses of the

films were roughly equal to those measured at Carbomedics, Inc.

b. Differential Scanning Calorimetry (DSC) Measurements

To prepare samples for DSC measurements, the thickness of the Nitinol plates was reduced from 2.5 mm to 0.6 mm using a Fenn rolling machine. Due to the explosive nature of fracturing of Nitinol on cold working, the plates were hot rolled. The samples were wet ground through 600 grit SiC paper, and then cut with a shearing device to small pieces, each weighing 25 mgm on the average. The samples were placed in an alumina crucible and vacuum annealed at 550°C for one hour in a Centorr vacuum furnace, model (M60 - 3 x 8 - W - D - 04S4 - A - 20). They were rinsed in acetone ultrasonically. Only one half of the samples were coated with carbon. The film thicknesses were 1500 A° and 3000 A°. Moreover, in order to promote the interfacial bond between the ULTI carbon and the Nitinol, and to magnify the effect of the surface constraint, some of the coated samples were heat treated in vacuum at 700°C for three hours and others for six hours. Uncoated samples were subjected to the same heat treatments to establish a reference for the comparison of experimental results between coated and uncoated samples tested by DSC.

DSC measurements of the coated and uncoated samples were performed using a DuPont Instruments 910 Differential Scanning Calorimeter that is equipped with a 9900

Computer/Thermal analyzer. The samples were placed in DuPont Instruments 900786-901 aluminum pans and covered with 900779-901 aluminum lids. Moreover, pure cathodic nickel, which has approximately the same thermal mass of the Nitinol samples, was used as the reference material.

Coated and uncoated Nitinol samples with identical thermomechanical histories were tested using DSC. The samples were thermally cycled between -40^{o}C to 80^{o}C. The temperature stability was maintained by using a liquid nitrogen cold stage. The ramp of heating and cooling for all samples was fixed at 5^{o}C/min.

c. X-ray Analysis

A General Electric model XRD-5 x-ray diffractometer was used to identify the phases present in the coated and the uncoated Nitinol samples. A copper target was used at 25 KV and 22 mA. The diffraction pattern was recorded for the 20 angle from 15^{o} to 95^{o} at a scanning rate of two degrees per minute.

The Nitinol samples used in x-ray analysis were prepared following the same procedure applied to the DSC samples. However, the samples used in the x-ray study had a larger area. Coated and uncoated samples with the same thermomechanical histories were heat treated in vacuum at 700^{o}C for one hour, three hours, and six hours prior to being analyzed using the x-ray diffraction technique. It was ensured by the vacuum annealing that all samples, coated and uncoated, were fully transformed into austenite.

d. Microhardness Measurements

To confirm the formation of TiC at the carbon/Nitinol interface as a result of heat treatment, microhardness measurements were performed. Coated specimens identical to those used in DSC measurements were used. Coated samples that were heat treated in vacuum at 700°C for one hour, three hours, and six hours, together with a coated sample that was not heat treated, were tested. A Buehler microindenter in the HV Vicker microhardness mode was used. An 0.3 kgm force was applied for 15 seconds at a loading speed of 50 microns/second.

e. Scanning Electron Microscopy of the Carbon Coated TiNi Alloy

Scanning electron microscopy was used to study the topography of the vapour deposited ULTI carbon on the Nitinol substrates. Nitinol substrates were cut from a 2.5mm thick plate using a Buehler Isomet low speed diamond saw. The samples were wet ground through 600 grit SiC paper and then polished through 0.3 micron alumina. The samples were then rinsed in acetone ultrasonically, dried, and ULTI carbon was vapour deposited on them. The surfaces of coated specimens that were not heat treated, together with other coated specimens that were vacuum heat treated at 700°C for one hour, three hours, and six hours, were examined using the scanning electron microscope. The microscope used was a Hitachi S-415A, and was operated at 25 KV.

f. Auger Electron Spectroscopy

The study of the characteristics of the surfaces and interfaces of the carbon coated Nitinol samples was accomplished with Auger electron spectroscopy (AES). Coated specimens, identical in their thermomechanical histories, were analyzed with using a Perkin-Elmer PHI 660 Scanning Auger microprobe equipped with a PHI 04-303 Sputter Ion Gun. The analysis was performed on coated samples that were not heat treated as well as on coated samples which were heat treated in vacuum at 700^{o}C for one hour, three hours, and six hours.

The AES was operated, not only to characterize the elements present at the surfaces and interfaces, but also to give information of whether the elements are present in the free or combined form. Depth profiling technique was applied to determine the chemical profiles normal to the surface of the carbon coated substrates. The AES was operated at a base vacuum of 2 x 10^{-10}mbar, an electron beam voltage of 30 KV, and an ion beam voltage of 3.5 KV. Argon was used to sputter an area of 2 x 2mm at a sputter pressure of 1 x 10^{-8}mbar. Moreover, the sputter rate was calibrated using a SiO_2 on Si standard, and was established to be about 80 A^{o}/min. The data was analyzed using an Apollo 3500 workstation equipped with PHI AES software.

g. Transmission Electron Microscopy

Among the experimental methods used to study the effect of surface constraint on the phase transformation of Nitinol was the transmission electron microscope (TEM). Since the material under study consisted of a thin carbon film vapour deposited on Nitinol substrates, with TiC at the interface, conventional preparation of TEM foils was inappropriate. The preparation had to be pursued as outlined by the cross-sectional transmission electron microscopy techniques [95, 96].

The preparation of TEM foils of the composite material used in this study involved several stages. Nitinol samples, 2.5 mm thick, 2.5 mm wide, and 20 mm long were cut using a Buehler Isomet low speed diamond saw. The samples were wet ground through 600 grit SiC paper, polished through 0.3 micron alumina, and then ultrasonically rinsed in acetone. The samples were vacuum annealed at 550°C for one hour, and ULTI carbon was vapour deposited on their surfaces. The carbon coated samples were then heat treated in vacuum at 700°C for three hours, and every two samples were glued together along their 20 mm length using super glue. Three hundred microns thick cross-sections were then cut using a diamond saw.

The next step involved spark cutting of 3mm diameter discs of the cross-sections. The diameter of the discs was selected to coincide with the space separating the two carbon coated surfaces of Nitinol facing each other. This

configuration is illustrated in Figure 7. Spark cutting was preferred to conventional mechanical techniques primarily because it does not cause stress induced martensite to form in the Nitinol samples. The cutting was performed using an Agie electrical discharge (EDM) machine equipped with a 3mm diameter graphite electrode, and operated at 100 volts and 9 amperes.

Preparation of the TEM foils required reduction of the thicknesses of the cross-sectional samples. After an ultrasonic acetone rinse, the discs were glued to Cu/Rh grids, having 2 x 1 mm slits, using super glue. The discs were then wet ground through 600 grit SiC paper to a thickness of 80 microns. The foil thickness was measured using a Gatan precision dimple grinder, model 656. The dimpler was also used to grind the central area of the foil down to 20 microns.

Two different transmission electron microscopes were used in examining the cross-sectional foils to study the effect of surface constraint on the phase transformation of Nitinol. One of the microscopes was a Hitachi H-800 electron microscope. It was operated at 200 KV, which corresponds to an electron wavelength (λ) of 0.0251 A^o, and had a camera length of 160 cm. The other microscope was a Jeol 100 CX II electron microscope equipped with a cold stage. It was mainly used to examine the foils at cryogenic temperatures where the Nitinol is fully transformed into martensite. The microscope was operated at 120 KV,

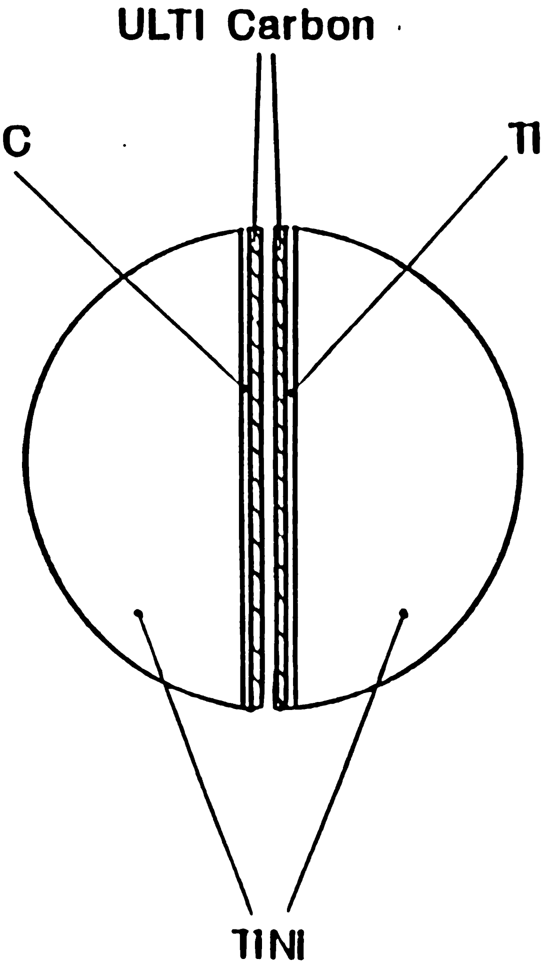

Figure 7. Illustration of the different layers of a cross-sectional TEM specimen following spark cutting

which corresponds to an electron wavelength (λ) of 0.0335 A^o, and had a camera length of 55 cm.

B. Biological Testing

As part of the design of a prosthesis for the reconstruction of the anterior cruciate ligament, biolite (ULTI carbon) was vapour deposited on Nitinol substrates. The objective of the vapour deposition of carbon was to induce the growth of collagenous tissue over the carbon coated surfaces. Review of the literature indicated that such a composite material has never been tested either in-vitro or in-vivo. Thus, carbon coated Nitinol filaments were tested by actual implantation in canine pelvic knees. Although the study is aimed at reconstructing the human anterior cruciate ligament, direct extrapolation of the results from canines to humans is acceptable.

1. Surgical Procedure

Nitinol filaments, 0.076 mm in diameter, were annealed in vacuum at 550°C for one hour. The filaments were rinsed ultrasonically in acetone, and then a thin film (3000 A^o) of ULTI carbon was vapour deposited on them. Moreover, the coated filaments were sterilized by gaseous ethylene oxide before their introduction into the canine's knee joint.

The surgical technique was similar to that followed to stabilize ruptured cruciate knees using fascia lata tissue in the dog. The canine which was a female large breed, 52 lb. in weight, was conditioned for one month prior to

surgery. One stifle joint was asceptically surgically approached. Tunnels were drilled in the condyles of the tibia and femur. A long band of fascia lata tissue was cut from the lateral side of the thigh and pulled through the tunnels in the femur and tibia. Prior to the placement of the tissue through the bone, carbon coated filaments were incorporated with it in such a manner that the filaments would be located in the stifle joint. After the tissue was pulled out of the tibia anteriorly, it was anchored to the patellar ligament. The wound was closed and the operated knee joint was then wrapped in soft padded bandage. After surgery, the canine was housed in a ward with no restriction to its motion. It was then euthanized 30 days post-operatively with a T-61 intravenous injection, and the knee joint was harvested [97, 98].

2. Scanning Electron Microscopy of Collagenous Tissue

Scanning electron microscopy was used to study the growth of collagenous tissue on the carbon coated Nitinol filaments following harvesting them from the canine's knee. To stop any degeneration of the harvested knee joint, it was immersed in 10% formalin for three days.

Cross-sectional and longitudinal cuts of the coated filaments adjacent to the patellar tendon and the surrounding tissue were made. The sections were dehydrated at room temperature in a series of ethyl alcohol/water mixtures with increasing concentrations of alcohol. The starting concentration was 70% alcohol by volume and the

final was 100% with 10% increments. The specimens were immersed in each concentration for one hour. Treatment of the tissue with the 100% alcohol concentration was repeated three times to make sure that dehydration was complete. At this stage, the tissue with the embedded filaments had to be critically dried to remove any water present. Thus, a critical point dryer using CO_2 gas was employed. The filaments and annexed tissue were then cut to smaller pieces and glued to aluminum SEM stubs using super glue. Since the tissue is non-conductive, it had to be sputter coated with gold before examination. The microscope used was a Hitachi S-415A scanning electron microscope, and was operated at 20 KV.

3. Histological Evaluation

Tissue sections of the canine's knee joint in which the carbon coated Nitinol filaments were incorporated were prepared for histological testing. The objective of this test was also to study the growth of collagenous tissue on the coated filaments. Longitudinal sections of the filaments adjacent to the patellar tendon, and transverse section of the filaments inserted in the tibia were made. These sections were first dehydrated following the same procedure used for the SEM specimens. The sections were then embedded in a Polaron embedding medium which is glycol methacrylate (GMA). Like dehydration, the embedding also was performed on stages. The first embedding was in a mixed solution of ethyl alcohol and GMA in the ratio of 1:1 by

volume. The second embedding was in a 1:3 solution and the third was in pure GMA. In each stage the tissue was embedded in the solution for 24 hours. Once the last stage of embedding was complete, benzoyl peroxide, which is a catalyst, was added to the solution to polymerize and harden the GMA under vacuum. At this stage, the tissue was embedded in a hard casing of GMA and sections as thick as 30 microns could be cut with the diamond saw. Finally, the sections were stained and then examined using a biological microscope [99].

IV. EXPERIMENTAL RESULTS

A. Phase Transformation Studies of Carbon Coated TiNi

Experimental results of the phase transformation studies of carbon coated TiNi were categorized with respect to the techniques used in the study. These techniques were differential scanning calorimetry (DSC), x-ray analysis, microhardness measurements, scanning electron microscopy (SEM), Auger electron spectroscopy (AES), and transmission electron microscopy (TEM).

1. Differential Scanning Calorimetry (DSC) Measurements:

A typical DSC curve of a TiNi shape memory alloy annealed for one hour at 550°C is illustrated in Figure 8 (a) and (b). The cooling cycle, which is shown in Figure 8(a), is exothermic, and is characterized by a martensitic start and finish temperatures. The heating cycle, on the other hand, is shown in Figure 8(b). This cycle is endothermic and is characterized by an austenitic start and finish temperatures. In both cases, the area under the curves is the enthalpy of the transformation, and is denoted by ΔH. Table 2 summarizes the data for the NiTi alloy under study, which has a composition of 50.1 at % Ni - 49.9 at % Ti. It is noted that the enthalpy of transformation of the

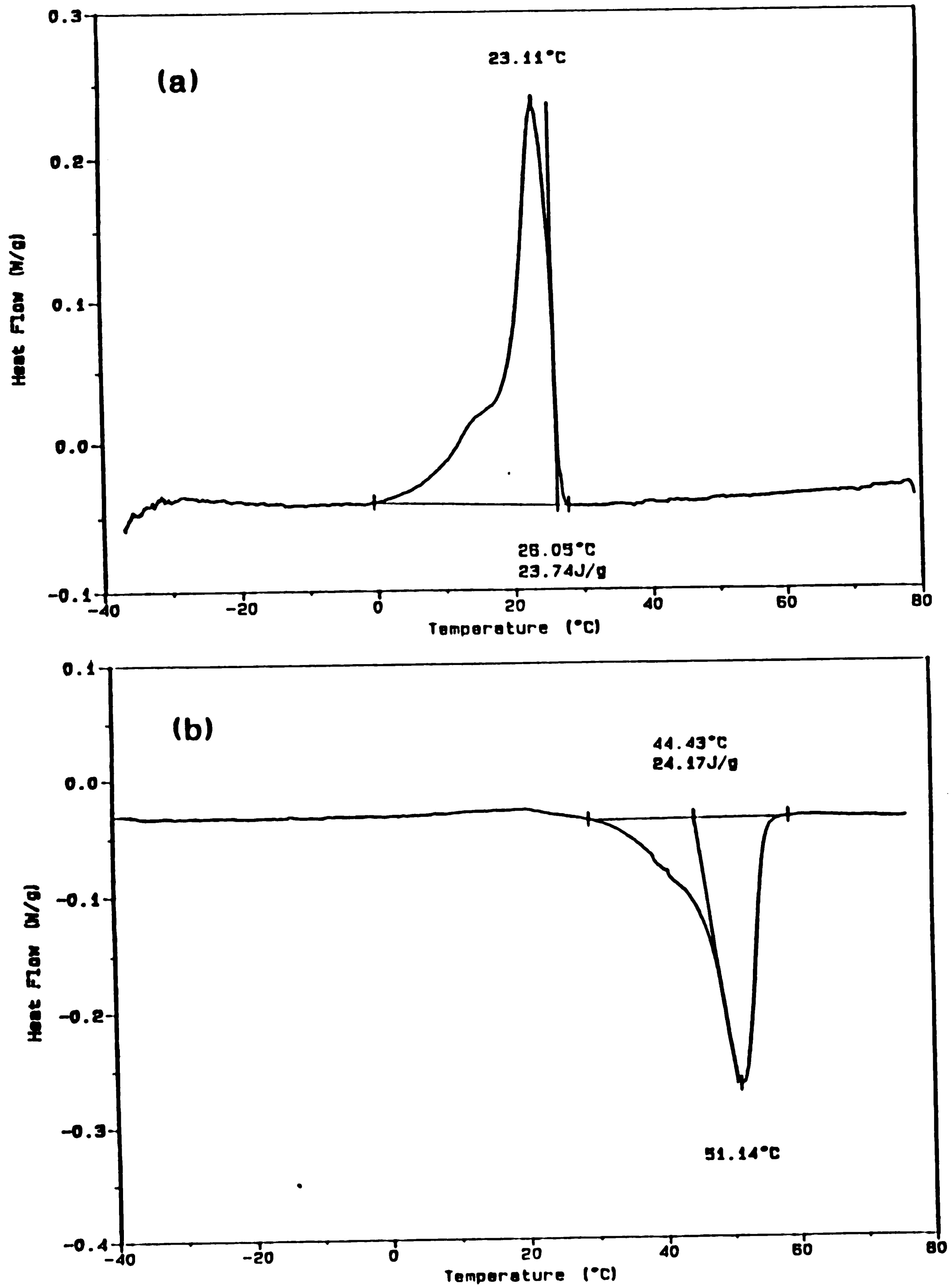

Figure 8. DSC of Nitinol (50.1 at % Ni - 49.9 % Ti) (a) First cooling cycle, (b) First heating cycle.

Table 2

Thermodynamic Data of a Near-Equiatomic NiTi Alloy (50.1 at % Ni - 49.9 at % Ti)

M_s = 300 K
M_f = 271 K
A_s = 296 K
A_f = 327 K
$\Delta H_{cooling}$ = 23.74 J/gm
$\Delta H_{heating}$ = 24.17 J/gm

cooling cycle is almost equal to the enthalpy of transformation of the heating cycle.

Figure 9 (a), (b), and (c) illustrates the difference in the cooling cycle for Nitinol as it was cycled one, ten, and forty times, respectively. In the first cycle, the martensitic transformation is characterized by a single exothermic peak. In the tenth cycle, Figure 9(b), two exothermic peaks are formed. The first peak to appear is associated with the premartensitic reaction and the formation of the R-phase, while the second one is associated with the martensitic phase. In the fortieth cycle, Figure 9(c), the premartensitic phase is characterized by a separate exothermic peak that precedes the martensitic transformation. However, the martensitic transformation starts at a lower temperature, compared to that in the tenth cycle.

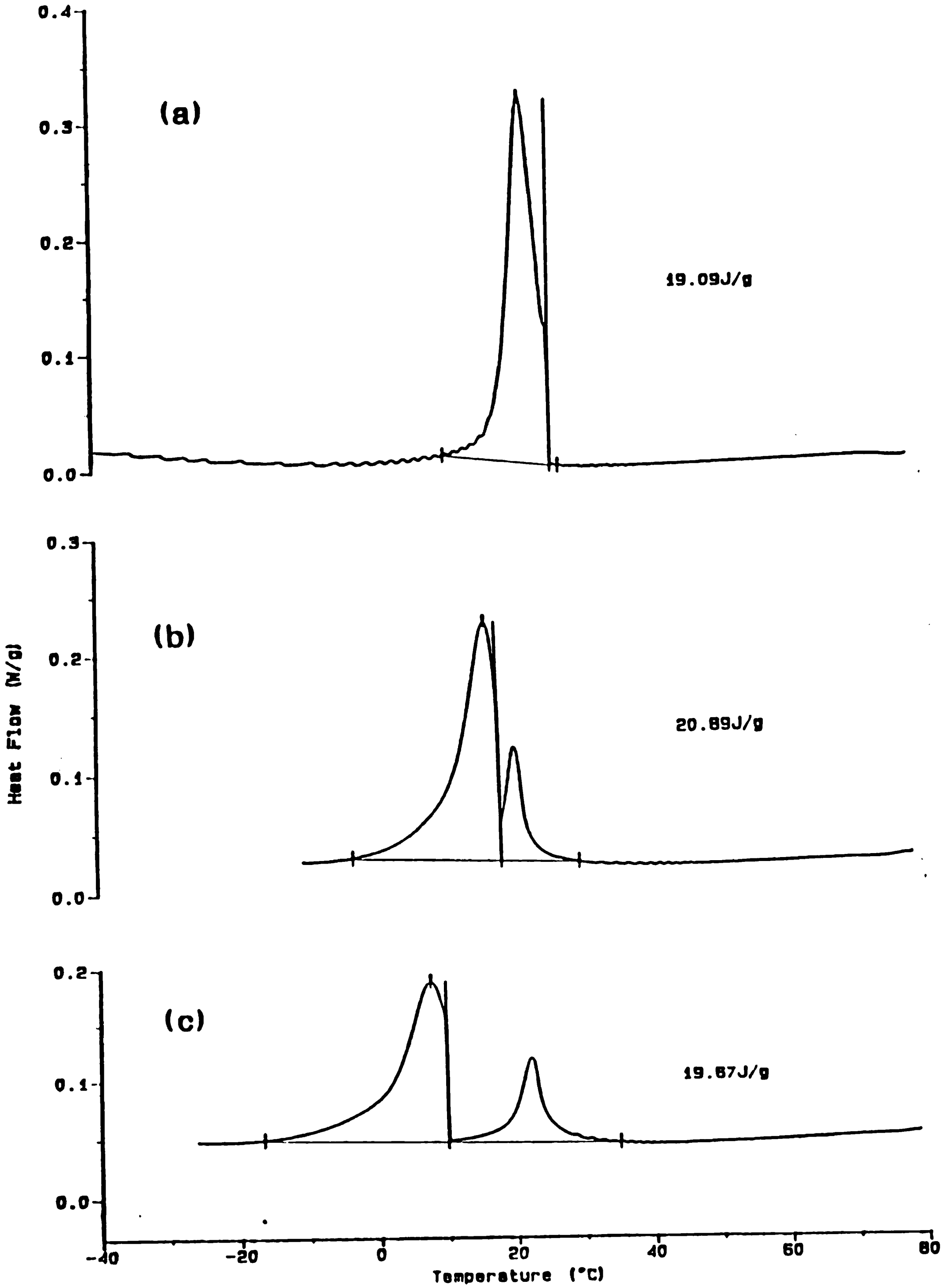

Figure 9. DSC of Nitinol (50.1 at % Ni - 49.9 at % Ti) in the cooling cycle. (a) First cycle (b) Tenth cycle (c) Fortieth cycle.

Although coating the Nitinol with carbon did not cause any changes in the transformation temperatures of the Nitinol, changes in the heats of transformation in both the heating and cooling cycles were noticed. Variation of the thicknesses of the coatings did not affect the transformation temperatures of Nitinol. Figure 10 (a) and (b) shows the exothermic peaks of uncoated and coated Nitinol samples, respectively, in the first cooling cycle. Figure 11 (a) and (b) shows the endothermic peaks of the uncoated and coated samples, respectively, in the first heating cycle. The heats of transformation (ΔH) of uncoated and coated Nitinol are given in Table 3. The data is given for two different thicknesses of Biolite$^{(R)}$, 1500 A^{o} and 3000 A^{o}. For the coated samples, two distinct characteristics are associated with the phase transformation. The first is that the carbon coating does not inhibit the formation of the R-phase as shown in Figure 12(a) and (b). The second is that thermal cycling of the coated Nitinol caused parts of the coating to flake out. This meant that the carbon coating vapour deposited without subsequent annealing was poorly bonded to the Nitinol substrates. This led to the idea of annealing the carbon coated Nitinol to enhance the bond at the carbon/Nitinol interface.

The objective of annealing the coated samples was to promote the interfacial bond between the TiNi and the ULTI carbon coating, and to magnify the effect of the surface constraint of Nitinol. To establish a reference for the

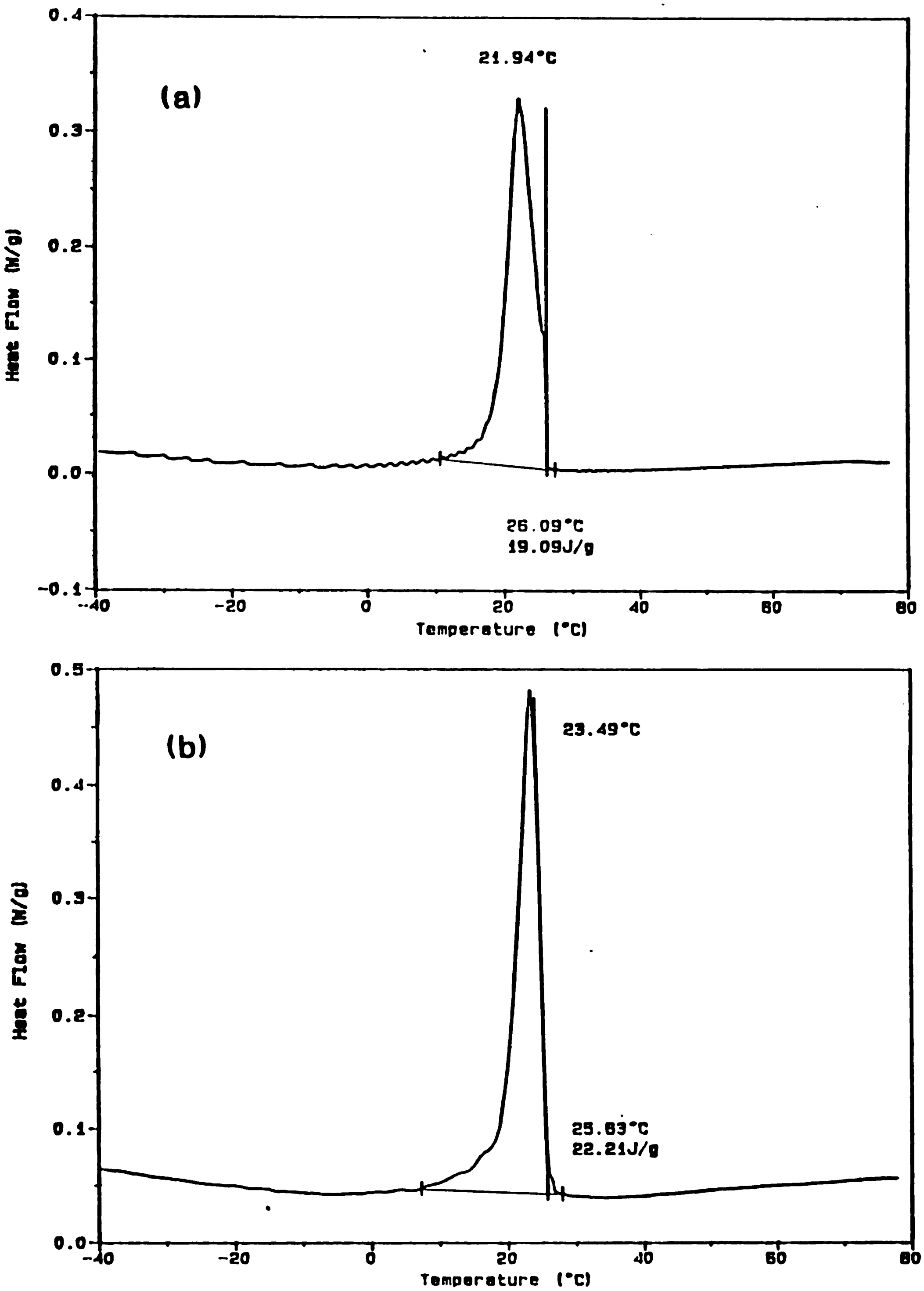

Figure 10. DSC cooling curves of Nitinol (first cycle) (a) Uncoated (b) Coated with a 3000 A^o carbon film.

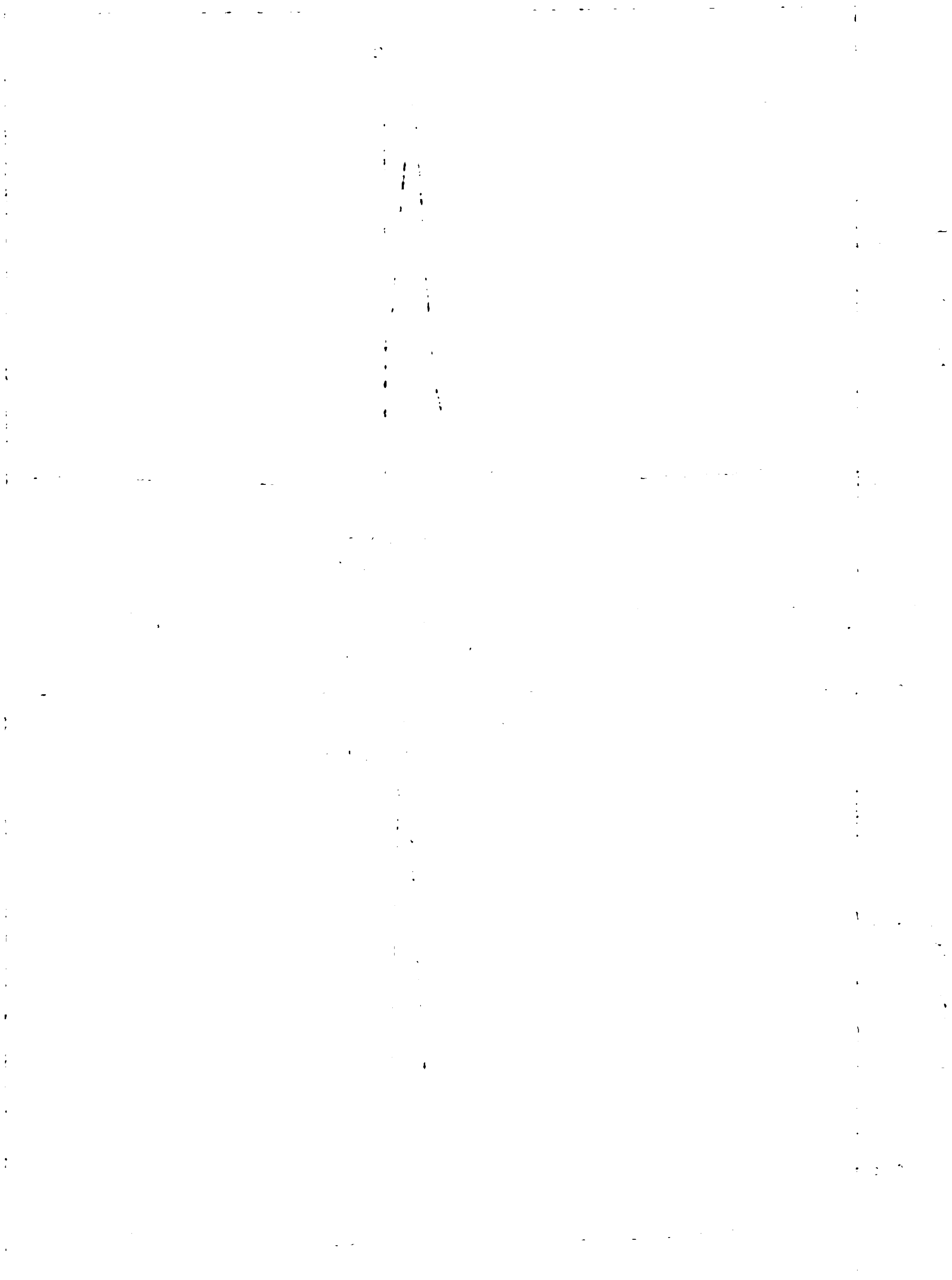

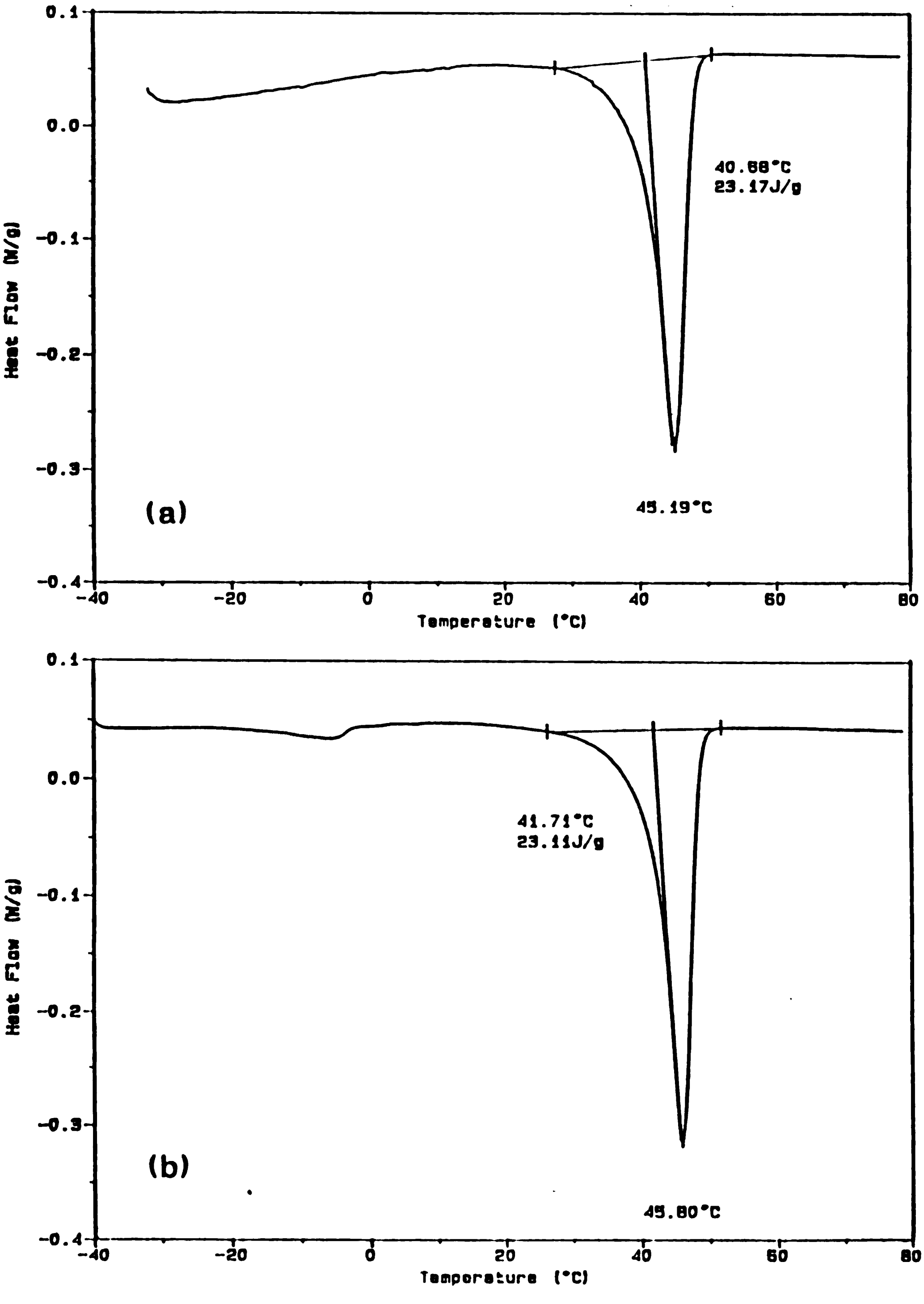

Figure 11. DSC heating curves of Nitinol (first cycle) (a) Uncoated (b) Coated with a 3000 A^{O} carbon film.

TABLE 3

Heats of Transformation (ΔH) of Coated and Uncoated Nitinol in the Unannealed State (J/gm)

(Substrate thickness = 600 μm)

	Uncoated		Coated			
			1500 A^{o}		3000 A^{o}	
Cycle	Cooling	Heating	Cooling	Heating	Cooling	Heating
1st	20.09	19.53	23.54	23.32	24.12	24.32
10th	20.00	22.16	23.30	23.30	23.61	22.49
20th	19.81	22.76	22.70	22.70	23.0	21.76
30th	19.14	22.65	22.80	22.80	23.03	20.96
40th	18.82	22.77	22.59	22.59	23.01	20.90

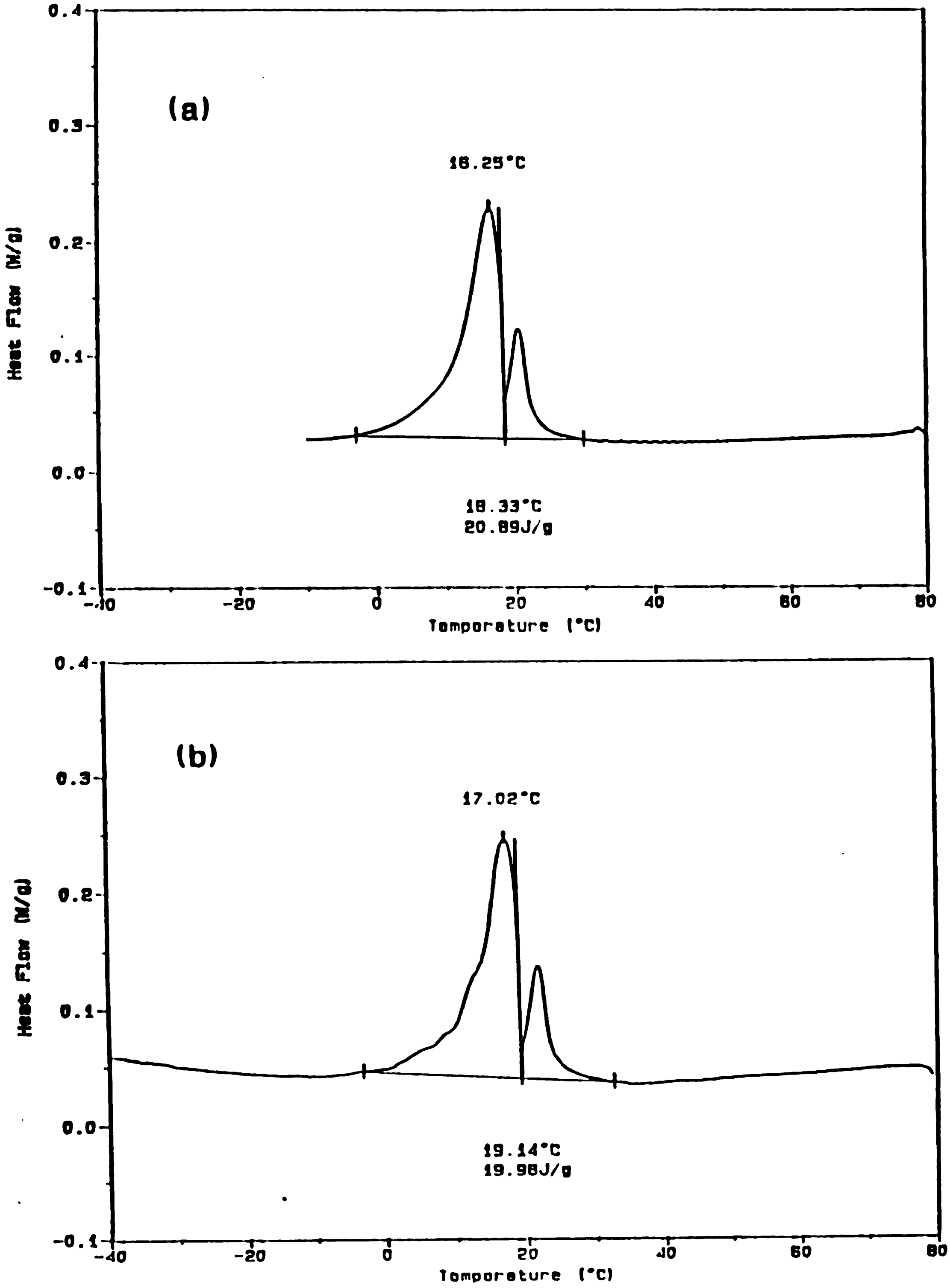

Figure 12. DSC cooling curves of Nitinol (tenth cycle) (a) Uncoated (b) Coated with a 3000 A^{O} carbon film.

comparison of the DSC measurements of the coated samples, uncoated Nitinol samples were subjected to the same heat treatment, and tested using DSC. Figure 13 (a) and (b) show the DSC curve in the first cooling cycle for an uncoated 3000 A^o carbon coated samples, respectively, that were each heat treated three hours at 700^oC. It is shown that although the M_s temperature remains the same for both the coated and uncoated samples, the M_f temperature for the coated and annealed sample dropped by about 20^oC in comparison to the uncoated sample. Figure 14 (a) and (b) shows the DSC curve of the first heating cycle of an uncoated Nitinol sample and a 3000 A^o carbon coated sample, respectively, each heat treated for three hours at 700^oC. It is shown that the A_f temperature for the coated and uncoated samples remains unchanged. However, in case of the coated sample, the A_s temperature dropped by about 20^oC in comparison to the uncoated one. Moreover, both Figures 15 and 16 demonstrate how the surface constraint of Nitinol inhibits the formation of R-phase. Figure 15 (a) and (b) show the formation of the R-phase in the uncoated and the 3000 A^o carbon coated Nitinol samples, respectively, in the tenth cooling cycle. Figure 16 (a) and (b) show the same effect for the uncoated and coated samples, respectively, in the fortieth cooling cycle.

When DSC measurements were run for uncoated and 3000 A^o carbon coated samples, annealed at 700^oC for six hours, similar results were obtained. Figure 17 (a) and (b) show the DSC cooling curve of the first cycle for uncoated and

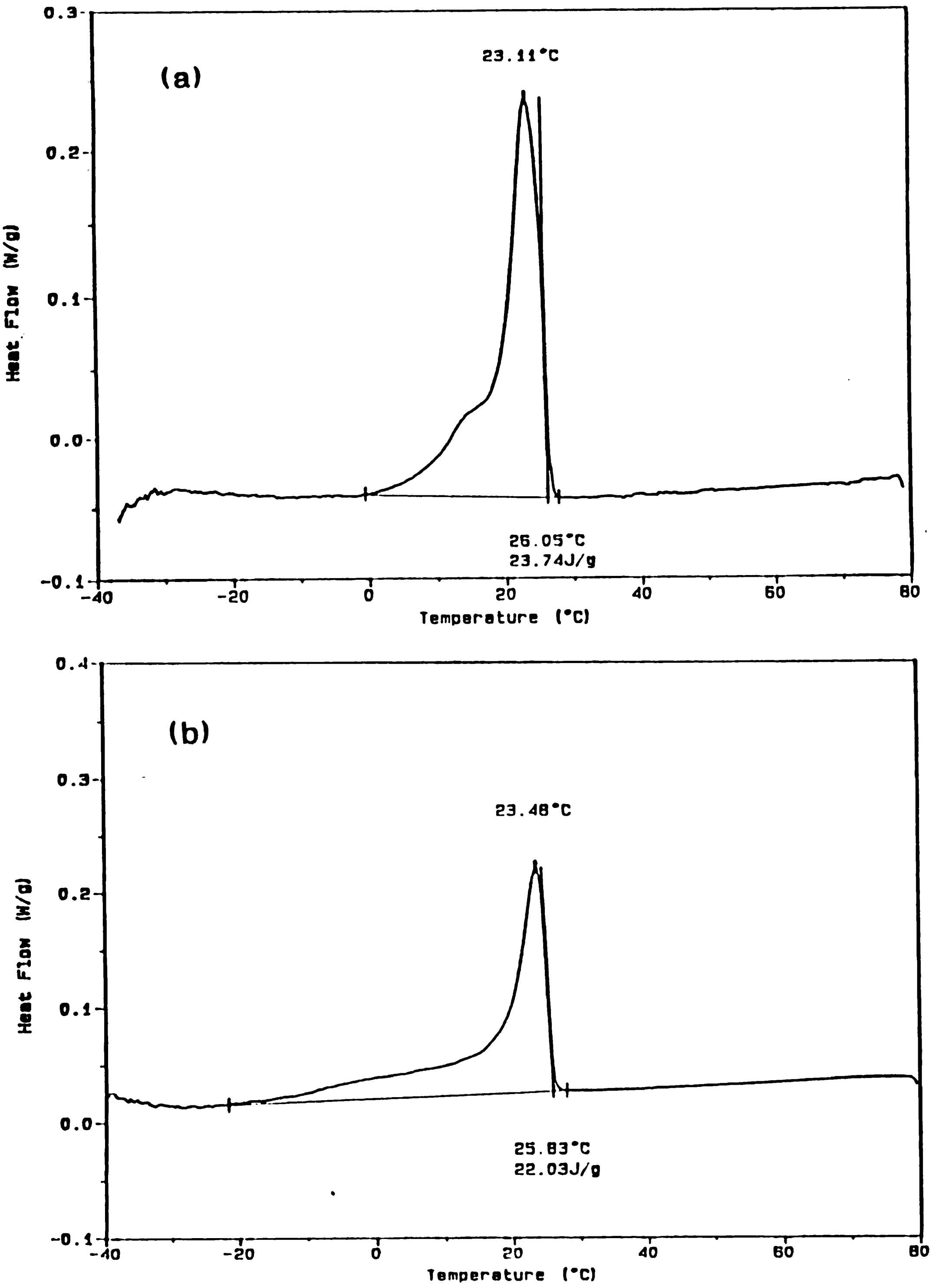

Figure 13. DSC curves of the first cooling cycle of Nitinol samples. (a) Uncoated and annealed at 700°C for 3 hours (b) Coated with a 3000 A° carbon film and annealed at 700°C for 3 hours.

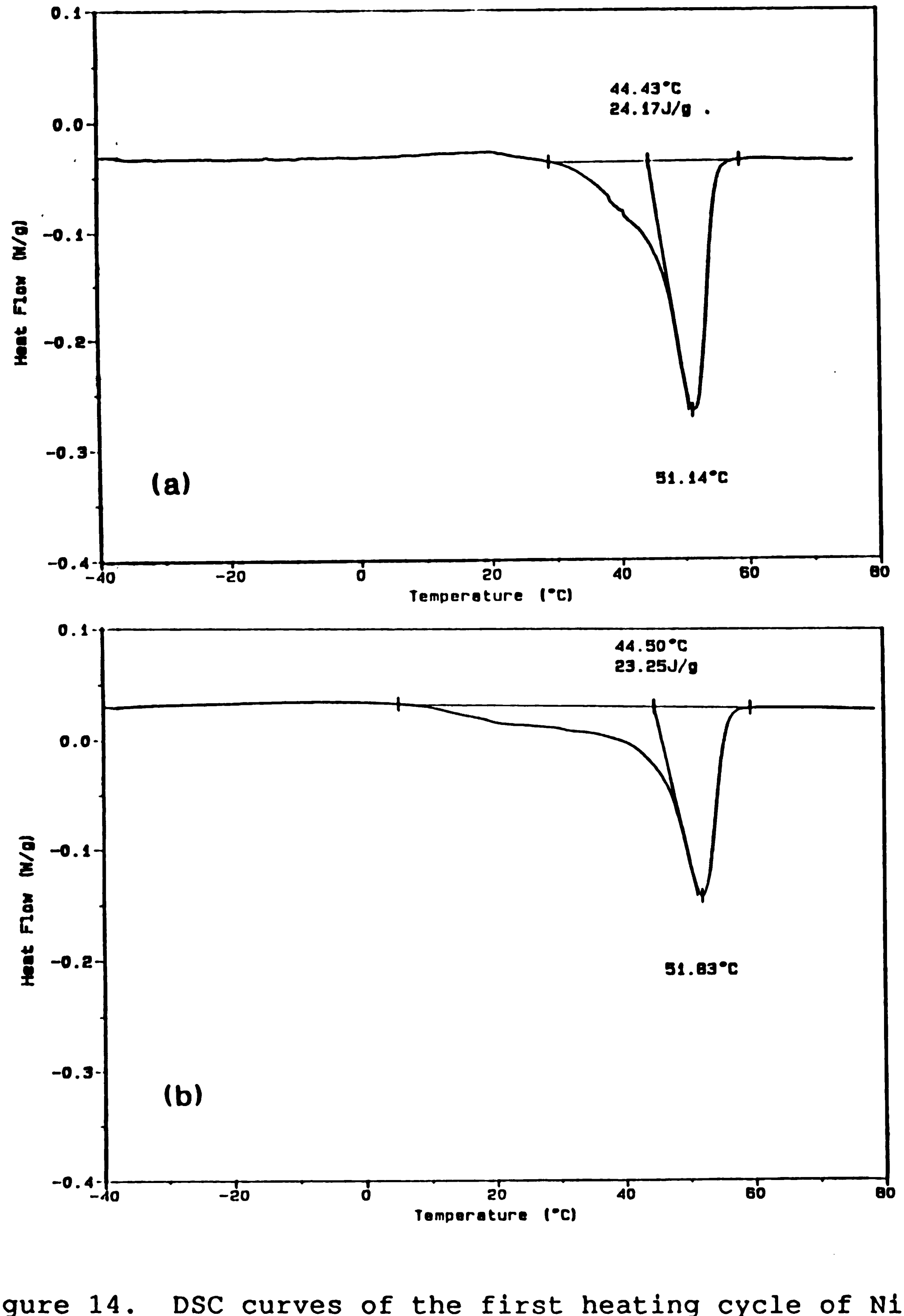

Figure 14. DSC curves of the first heating cycle of Nitinol samples. (a) Uncoated and annealed at 700°C for 3 hours (b) Coated with a 3000 A° carbon film and annealed at 700°C for 3 hours.

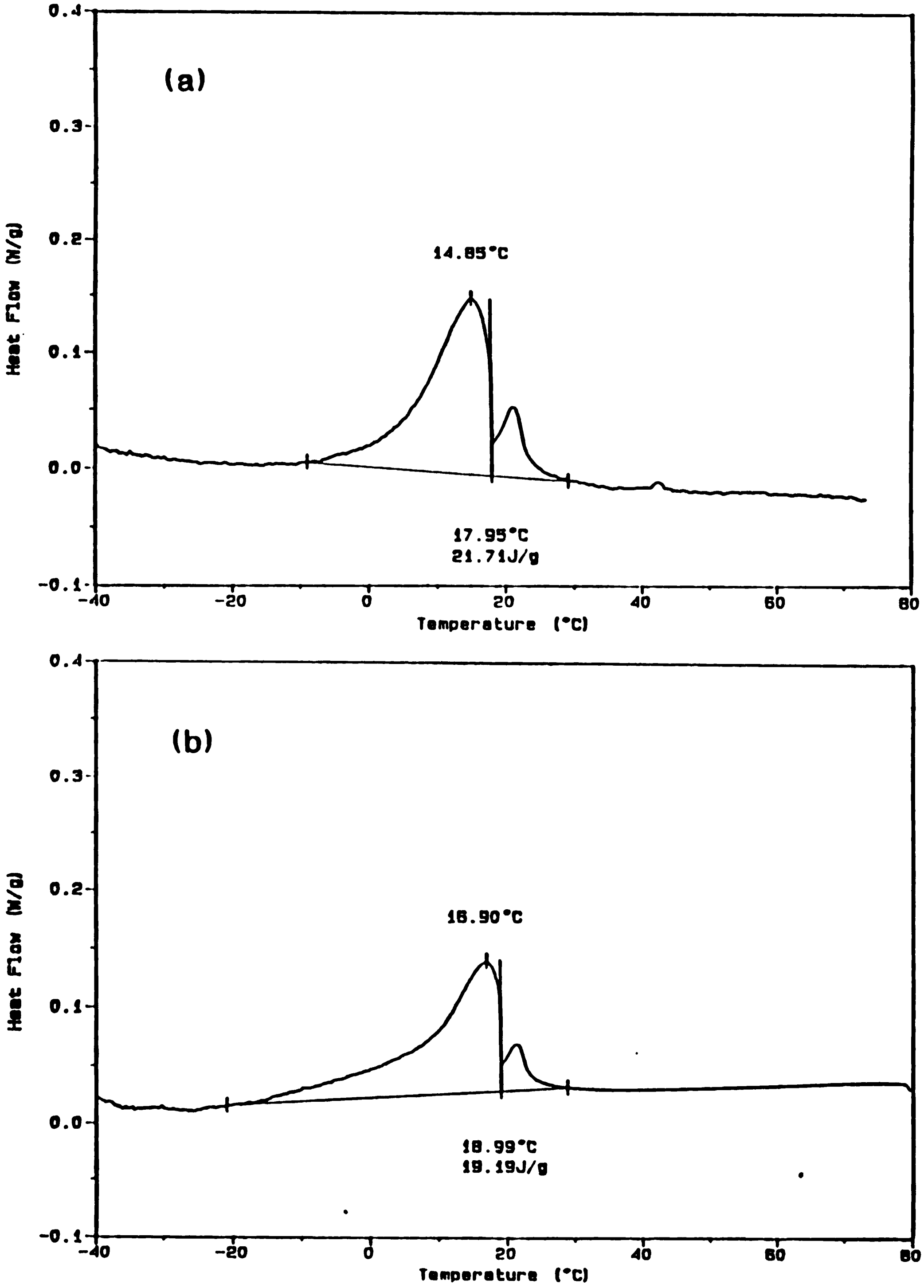

Figure 15. DSC curves of the 10th cooling cycle of Nitinol samples. (a) Uncoated and annealed at 700°C for 3 hours (b) Coated with a 3000 A° carbon film and annealed at 700°C for 3 hours.

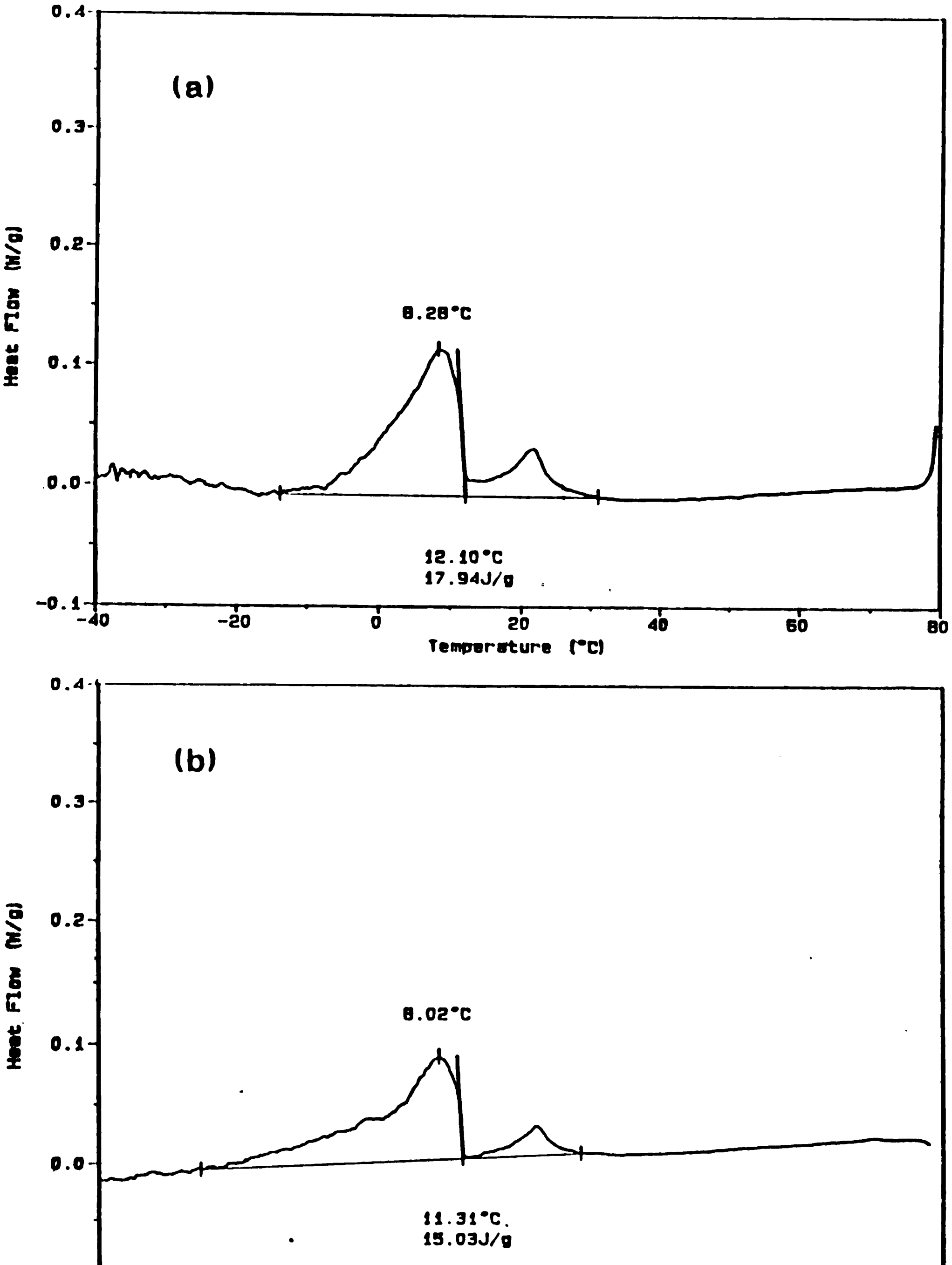

Figure 16. DSC curves of the 40th cooling cycle of Nitinol. (a) Uncoated and annealed at 700°C for 3 hours (b) Coated with a 3000 A° carbon film and annealed at 700°C for 3 hours.

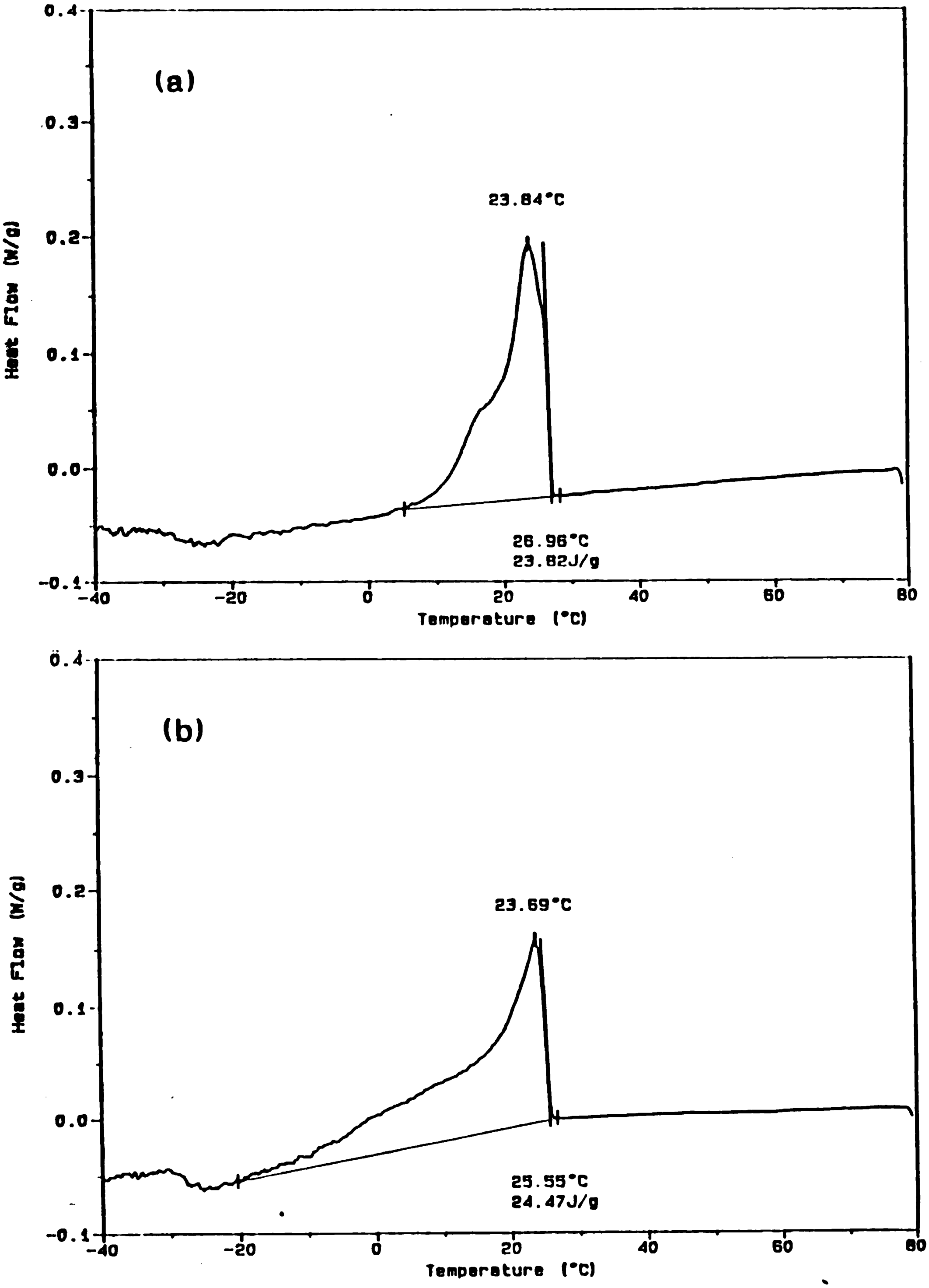

Figure 17. DSC curves of the first cooling cycle of Nitinol samples. (a) Uncoated and annealed at 700°C for 6 hours (b) coated with a 3000 A° carbon film and annealed at 700°C for 6 hours.

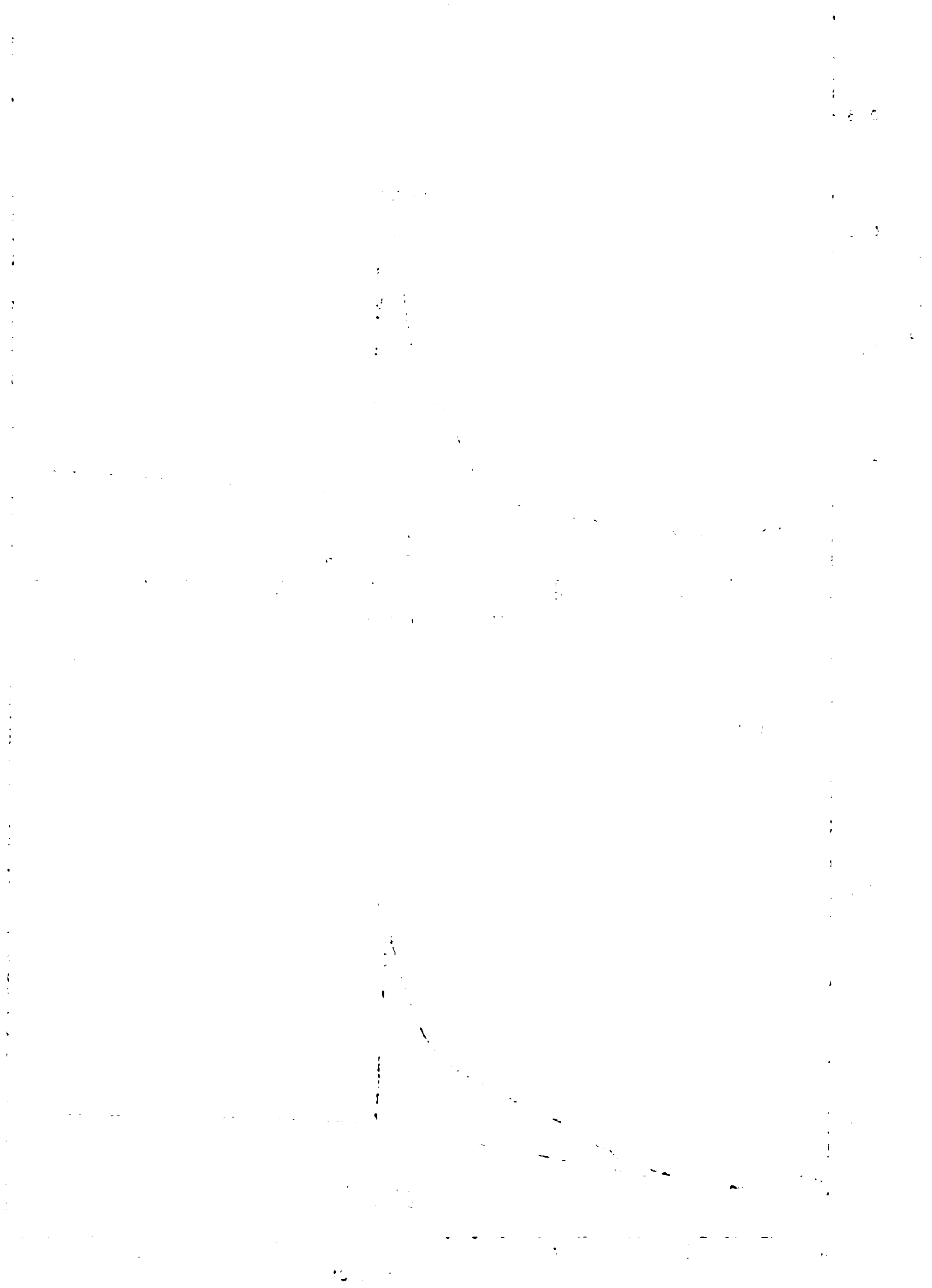

coated Nitinol samples, respectively. Figure 18 (a) and (b) shows the DSC curves for the heating cycle. From both Figures 17 and 18 it is shown that for the constrained samples, the M_f and A_s temperatures dropped markedly, while the M_s and A_f temperatures were unchanged.

Cycling the uncoated and coated samples that were heat treated at 700°C for six hours was performed to study the effect of surface constraint on the R-phase. It was found out that the heat treatment promoted the surface constraint and inhibited the formation of the R-phase. This is shown in Figures 19 and 20, where the uncoated and coated samples were cycled ten and forty times, respectively.

2. X-Ray Analysis:

X-ray analysis was made for the uncoated and 3000 A° carbon coated Nitinol. The structure of the carbon coating is turbostratic, which is a semicrystalline structure. Thus, no peaks were recorded from the carbon film. This is illustrated in Figure 21 (a) and (b) which show the x-ray diffraction pattern of uncoated and carbon coated Nitinol, respectively.

On annealing the carbon coated Nitinol, the thickness of TiC formed at the carbon/Nitinol interface increases. Consequently, peaks of TiC appear in the x-ray diffraction pattern of annealed carbon coated Nitinol. Fig. 22 shows the diffraction pattern of a 3000 A° carbon coated sample that was annealed for three hours at 700°C. The intensities of the TiC peaks are small in comparison to the TiNi peaks.

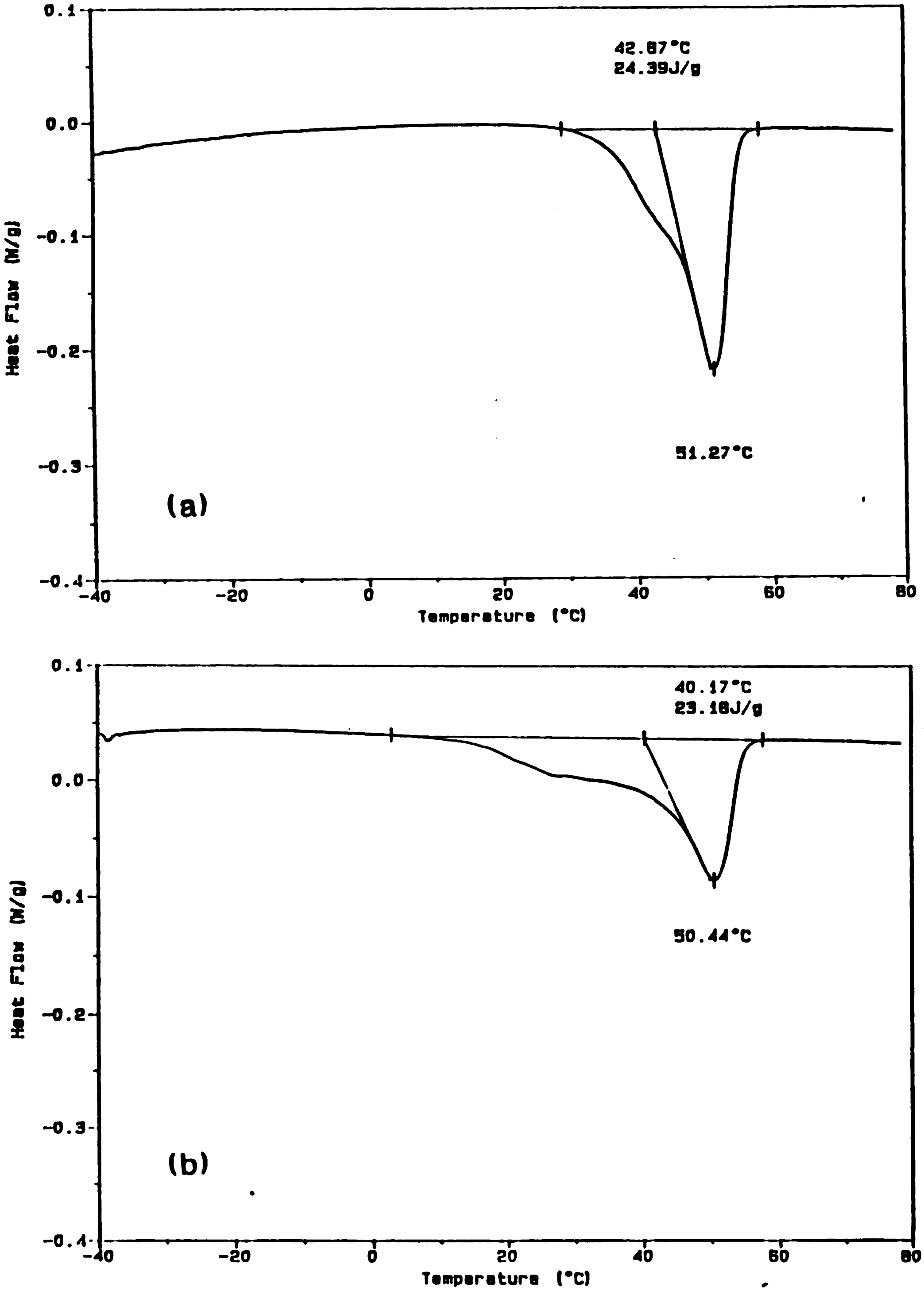

Figure 18. DSC curves of the first cooling cycle of Nitinol samples. (a) Uncoated and annealed at 700°C for 6 hours (b) coated with a 3000 A^{o} carbon film and annealed at 700°C for 6 hours.

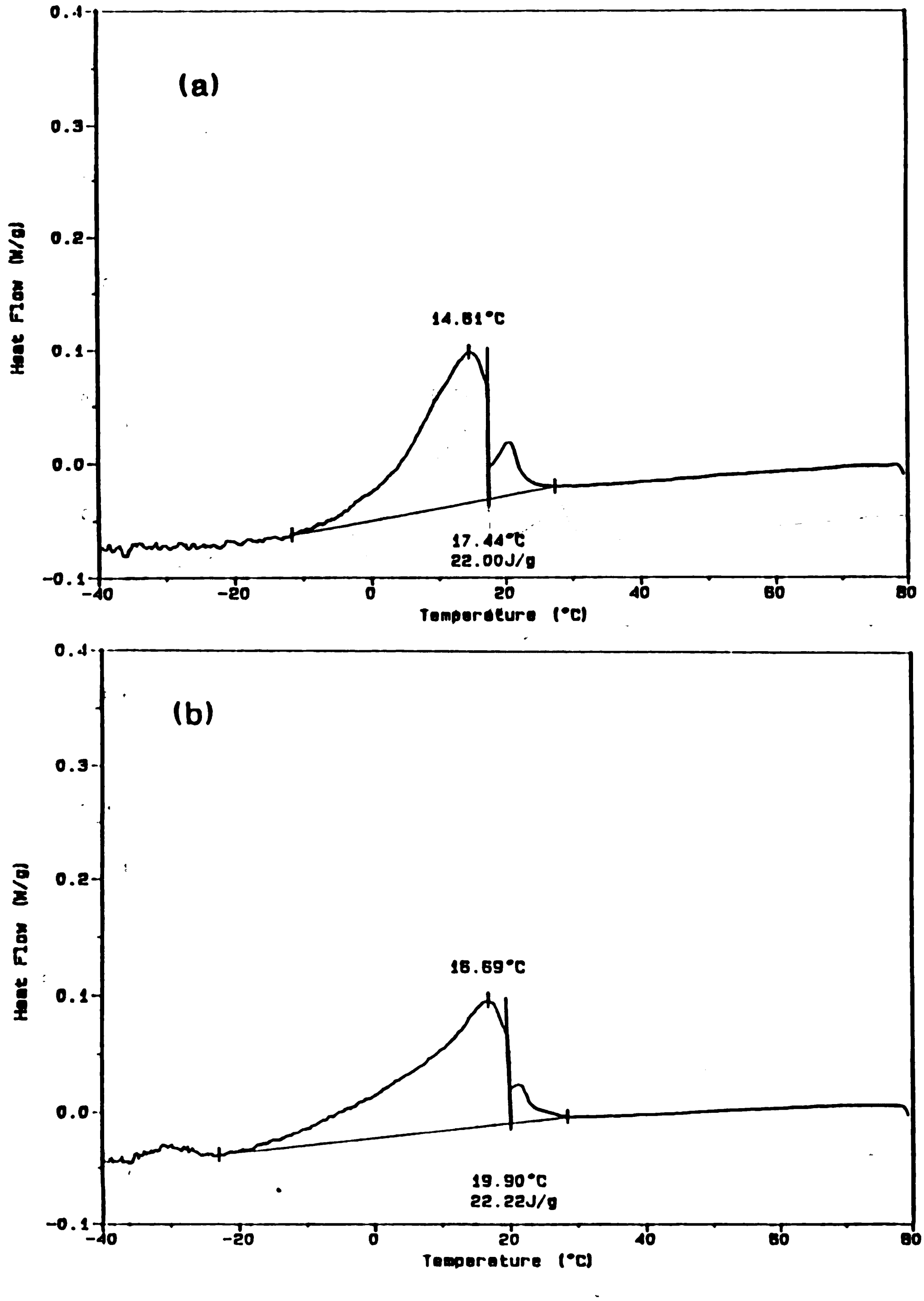

Figure 19. DSC curves of the 10th cooling cycle of Nitinol samples. (a) Uncoated and annealed at 700°C for 6 hours (b) Coated with 3000 A^o carbon film and annealed at 700°C for 6 hours.

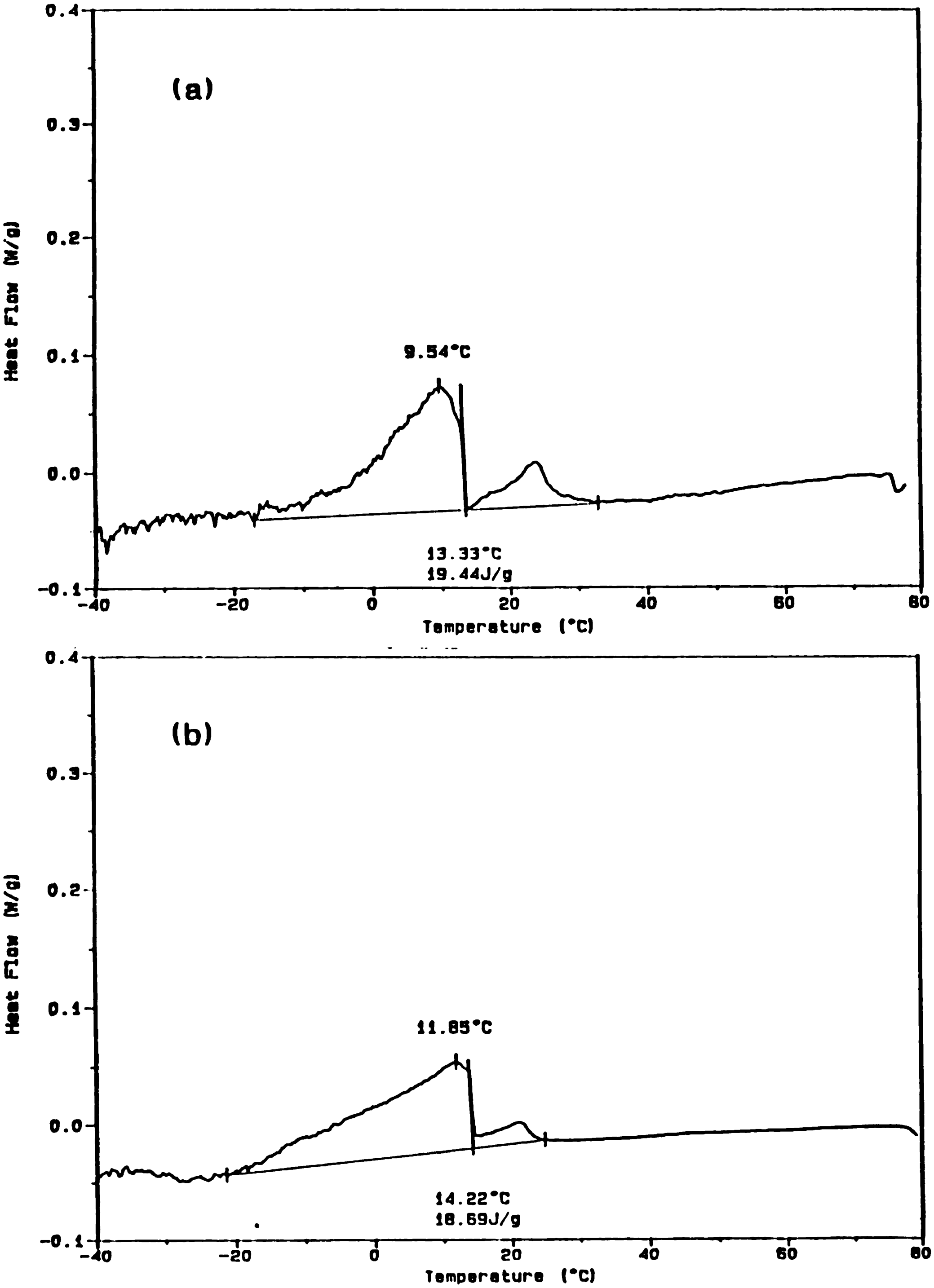

Figure 20. DSC curves of the 40th cooling cycle of Nitinol samples. (a) Uncoated and annealed at 700°C for 6 hours (b) Coated with 3000 A^o carbon film and annealed at 700°C for 6 hours.

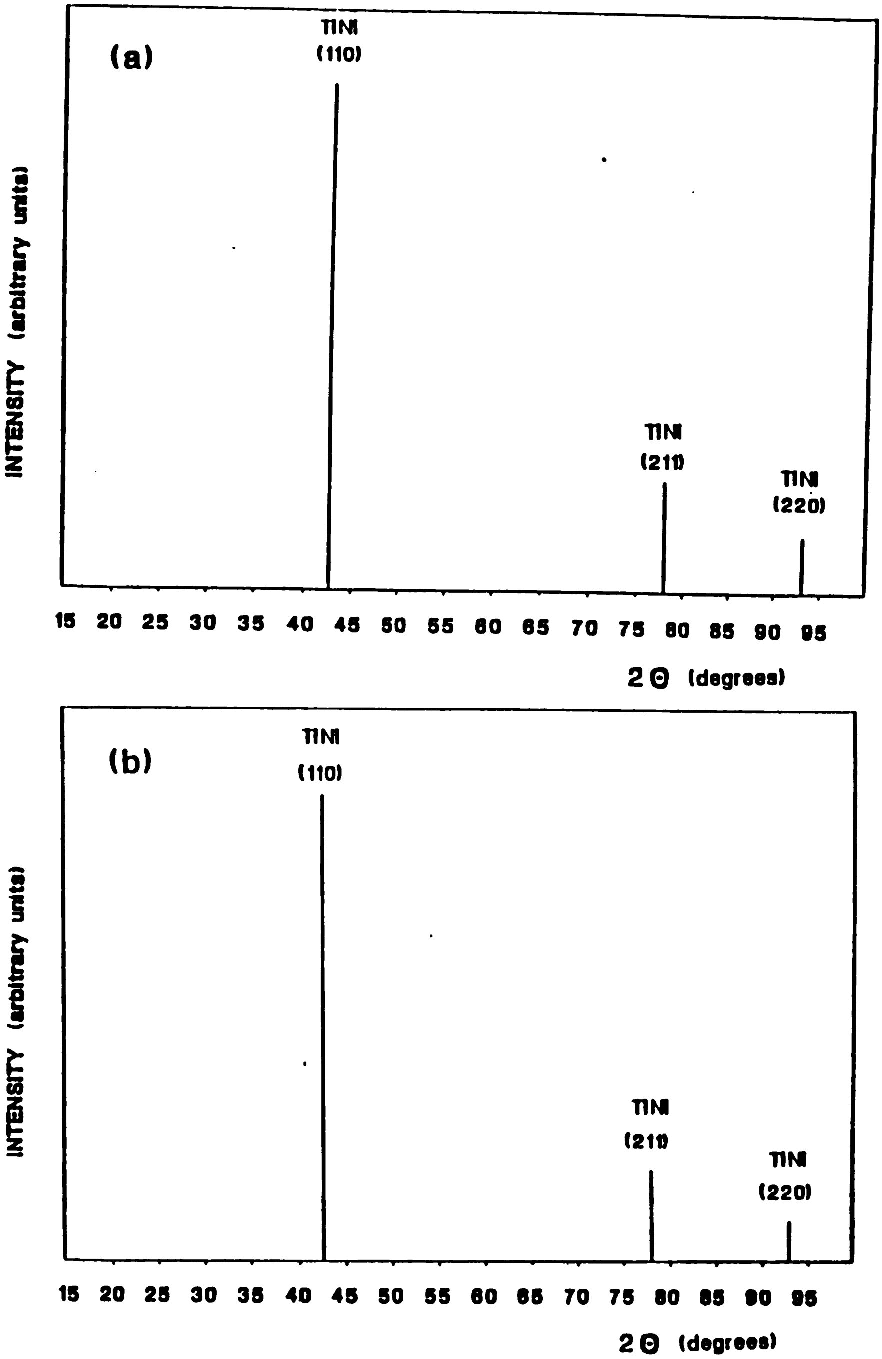

Figure 21. X-ray diffraction pattern of Nitinol (a) Uncoated (b) Coated with a 3000 A^o carbon film.

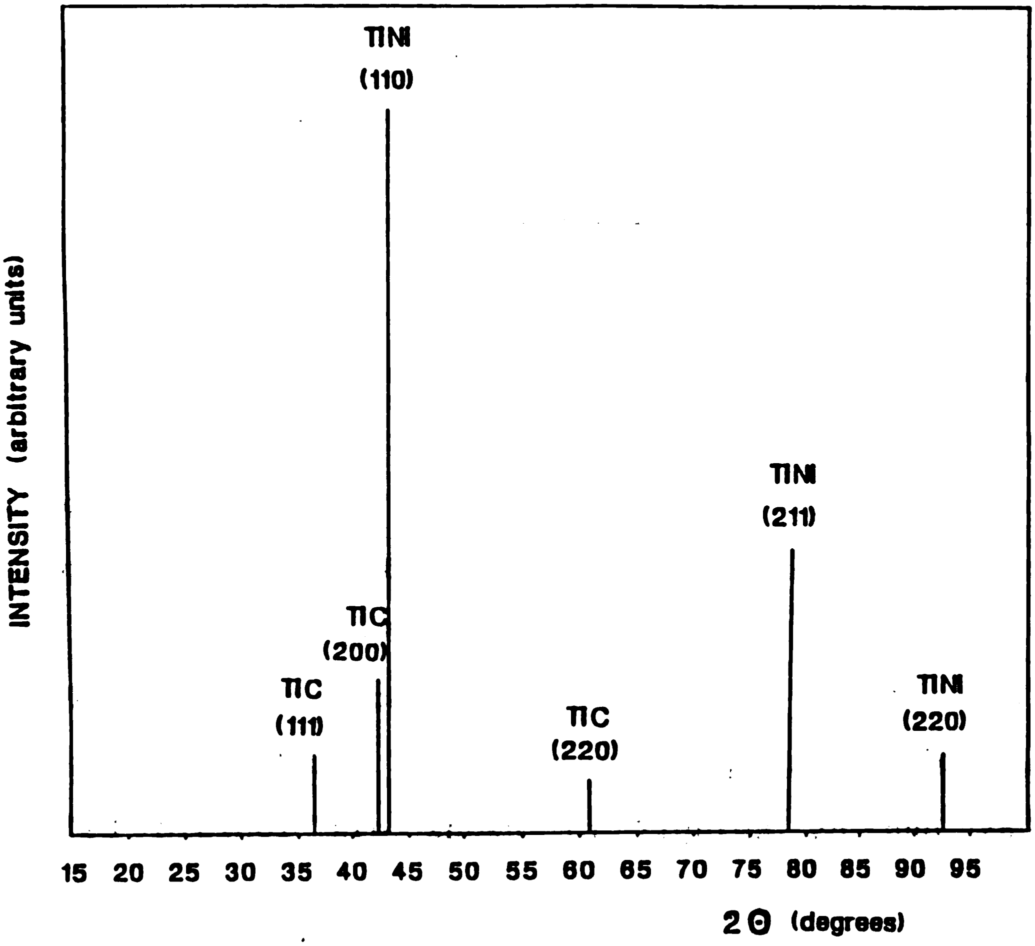

Figure 22. X-ray diffraction pattern of a 3000 A^o carbon coated Nitinol sample heat treated at 700^oC for 3 hours after coating.

Annealing of the carbon coated samples at the same temperature (700°C) for a longer period of time, six hours, caused the TiC peaks to intensify. This effect is illustrated in Figure 23.

3. Microhardness Measurements:

Microhardness measurements were run on 3000 A° carbon coated Nitinol samples that were heat treated at 700°C. As the annealing time increased, the thickness of the TiC at the carbon/TiNi interface increased. Consequently, the surface hardness increased. This effect is shown in Figure 24.

4. Scanning Electron Microscopy of the Carbon Coated TiNi Alloy

The electron microscope was used in the scanning mode to evaluate both the microstructure and topography of the uncoated and carbon coated Nitinol samples. The vapour deposited ULTI carbon film was found to form a continuous film on the Nitinol surface. Thicknesses of the carbon film up to 3000 A° did not change the topography of Nitinol, and had no microstructural features. SEM photomicrographs of unannealed Nitinol are shown in Figures 25 and 26 for uncoated and coated samples, respectively. Comparison of the microstructure in both micrographs prove that the coating is continuous and does not change the topography of the Nitinol samples. On annealing uncoated and coated Nitinol samples, the carbon film remained continuous and did

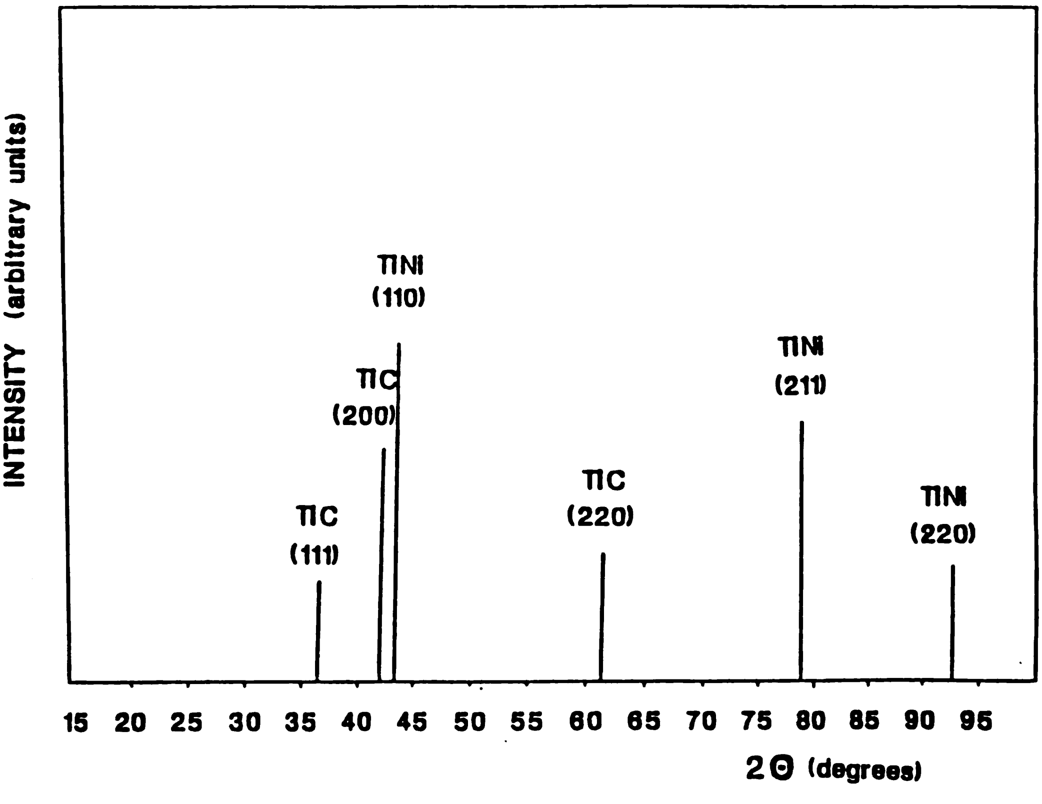

Figure 23. X-ray diffraction pattern of a 3000 A^{o} carbon coated nitinol sample heat treated at 700^{o}C for 6 hours after coating.

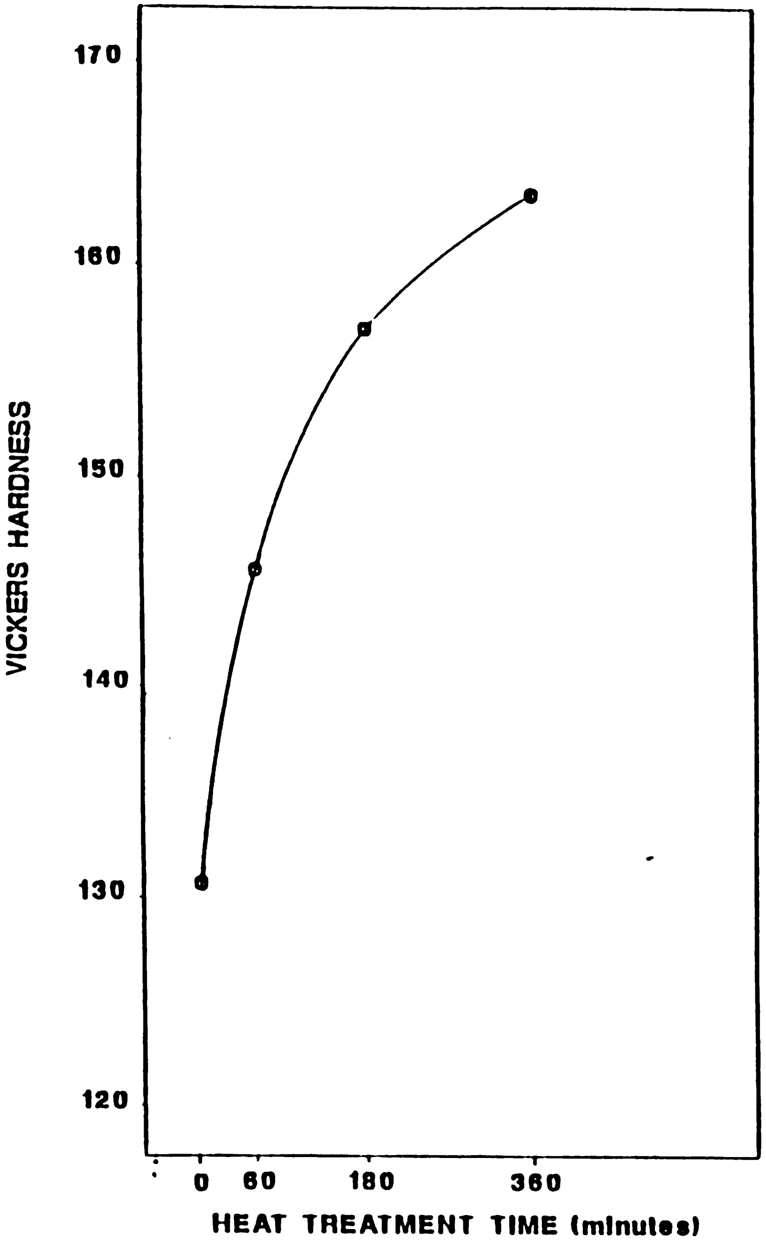

Figure 24. Vickers hardness as a function of annealing time of a 3000 A$^{\circ}$ carbon coated Nitinol sample heat treated at 700°C. Each hardness point is an average of 5 readings. The maximum deviation is 9.48%.

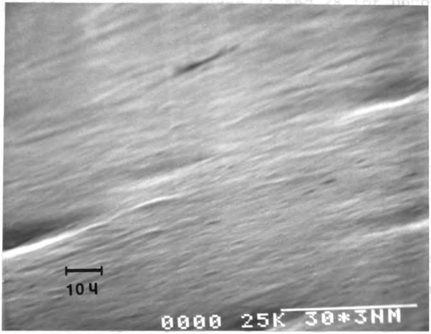

Figure 25. SEM photomicrograph of an uncoated, unannealed Nitinol sample.

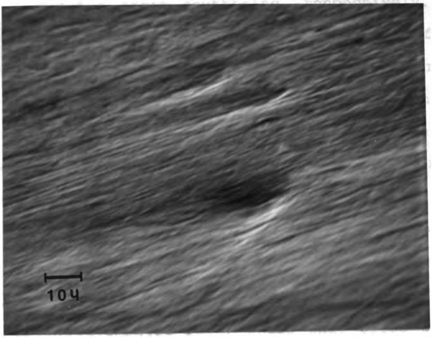

Figure 26. SEM photomicrograph of an unannealed 3000 A^{o} carbon coated Nitinol sample.

not change the topography of the Nitinol surface. The latter case is illustrated in Figures 27 and 28 for uncoated and coated Nitinol samples, respectively, that were heat treated at 700^{o}C for three hours.

5. Auger Electron Spectroscopy

Elemental analysis of the carbon coated Nitinol was done using Auger Electron Spectroscopy. The analysis was done for 3000 A^{o} carbon coated Nitinol samples that were unannealed, as well as for coated sample that were annealed for one hour, three hours, and six hours. Concentration profiles using the depth profiling technique were also obtained for these samples.

Figure 29 (a) and (b) show the Auger spectrum of an unannealed 3000 A^{o} carbon coated Nitinol sample after one minute and 26 minutes argon sputtering, respectively. In Figure 29 (a) it is illustrated that the surface of the Nitinol is completely covered with carbon, while Figure 29 (b) show that carbon, nickel, titanium and oxygen are present at the carbon/Nitinol interface. It is speculated that the oxygen was present as a very thin layer over the Nitinol surface prior to carbon deposition, or was introduced to the Nitinol surface early in the deposition process with carbon. Analysis of the carbon signal in the Auger spectrum show that the carbon at the surface (Figure 29 (a)) is in the elemental form, while that close to the interface (Figure 29 (b)) is in the compound form, titanium carbide. Figure 30 show a depth profile of the unannealed

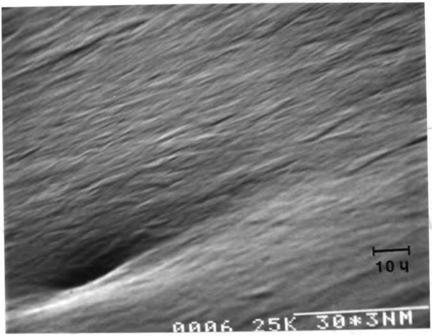

Figure 27. SEM photomicrograph of an uncoated Nitinol sample heat treated at 700°C for 3 hours.

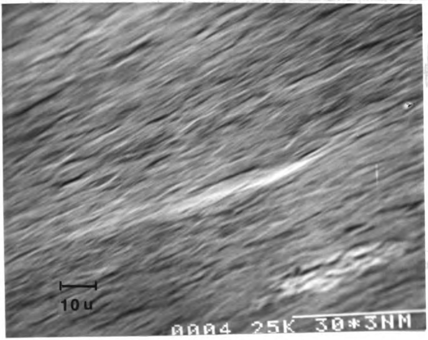

Figure 28. SEM photomicrograph of a 3000 A° carbon coated Nitinol sample that was heat treated at 700°C for 3 hours after coating.

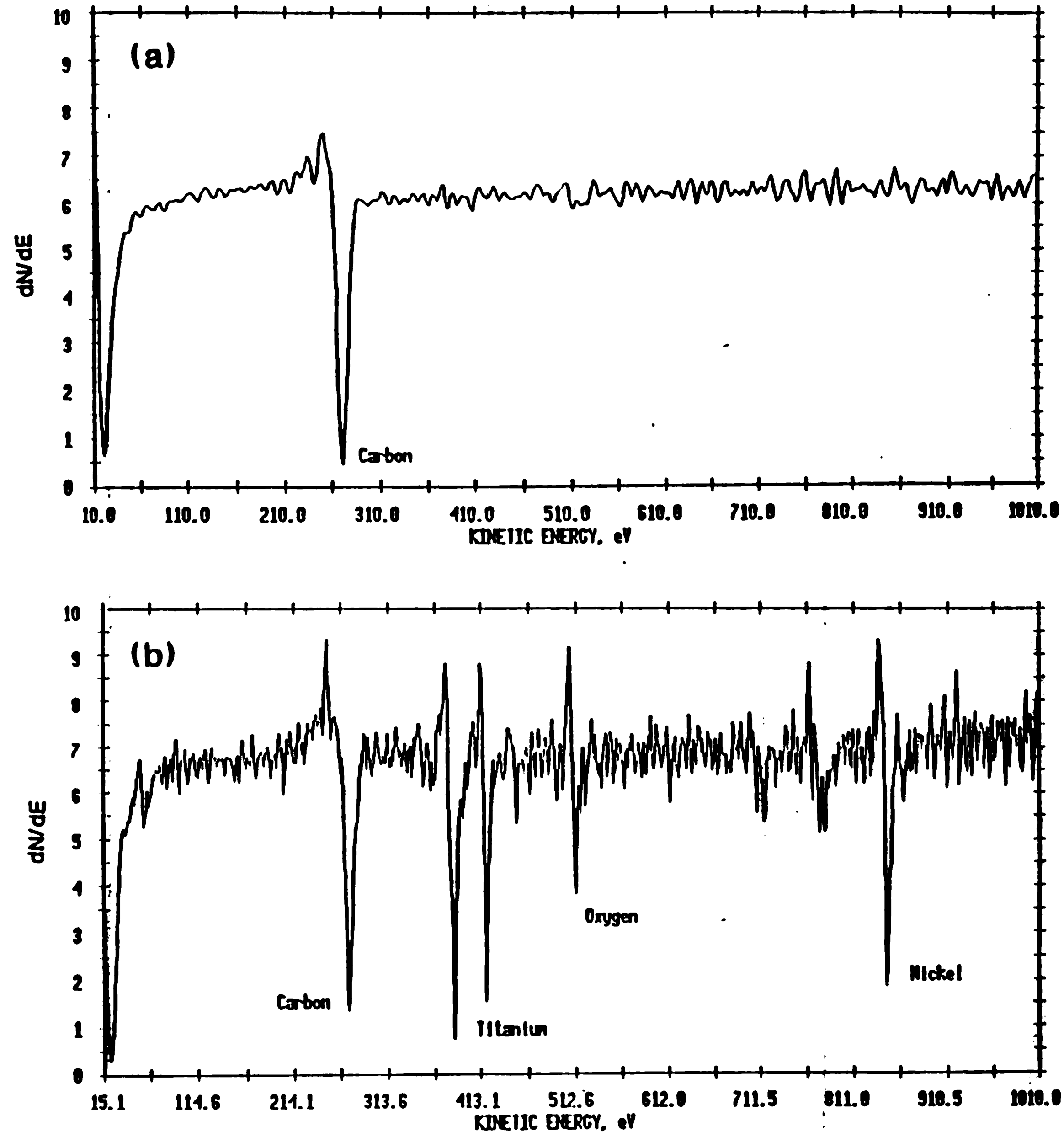

Figure 29. Auger signal of an unannealed 3000 A^{o} carbon coated Nitinol sample (a) one minute argon sputtering (b) 26 minutes argon sputtering.

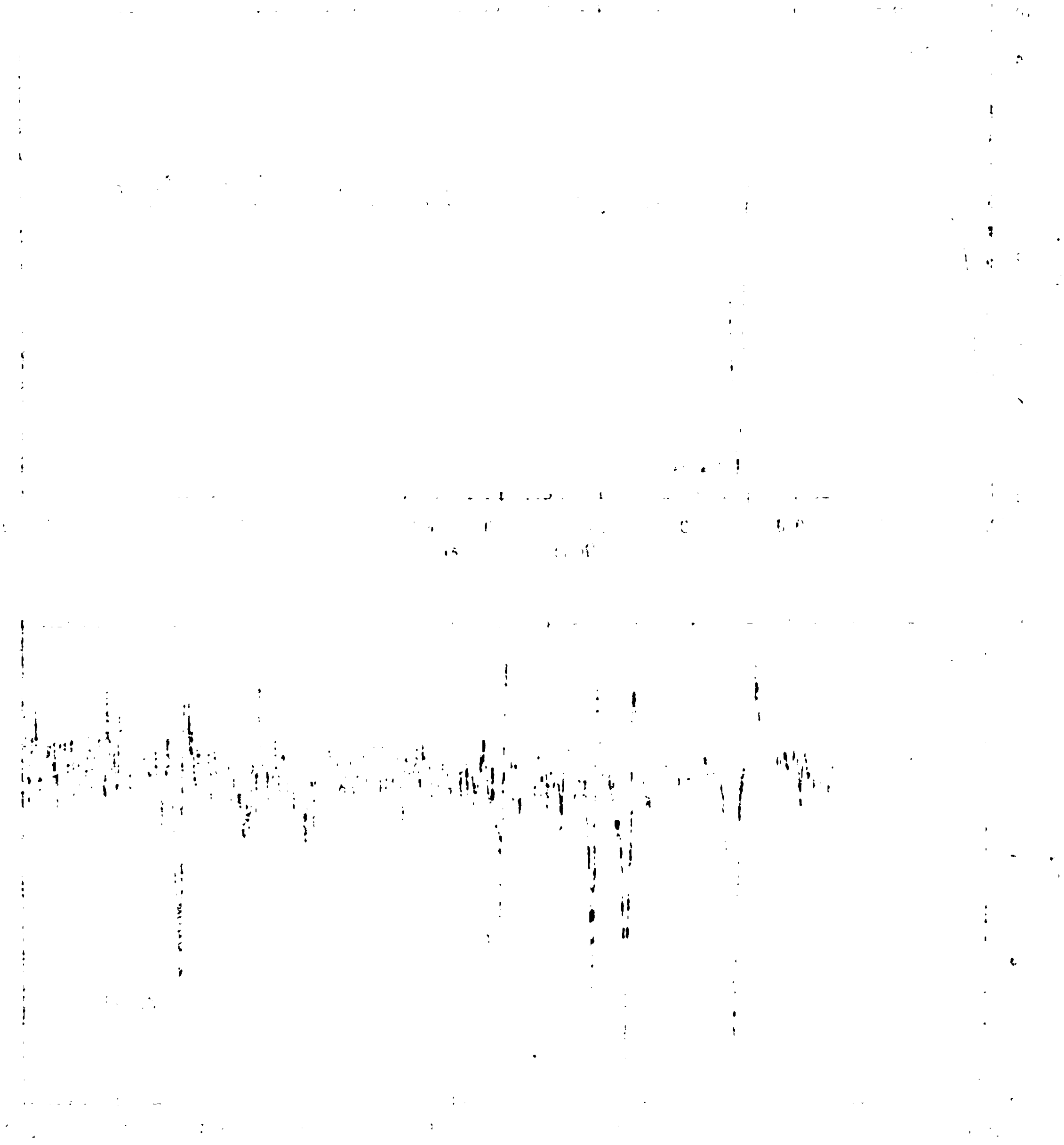

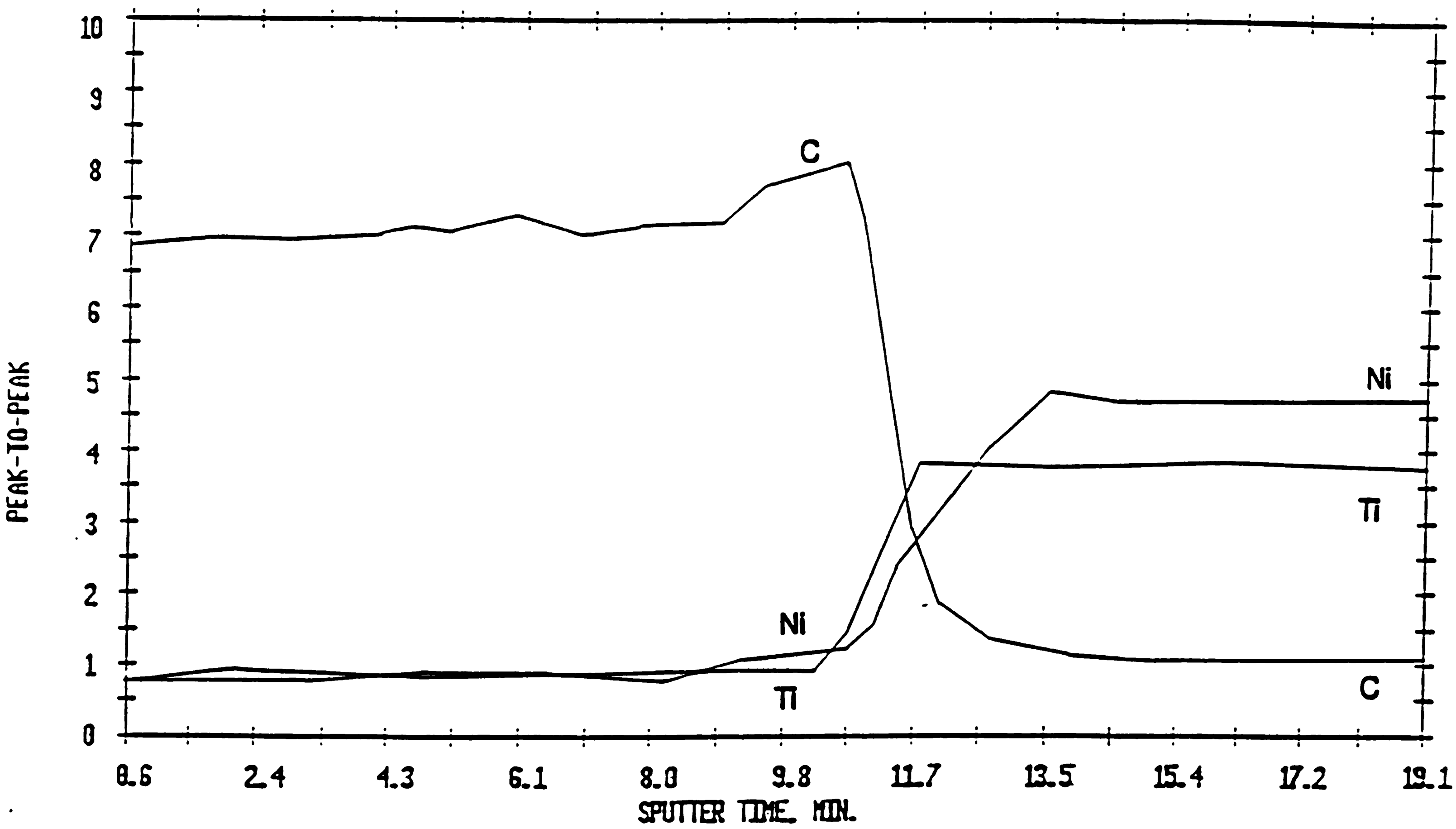

Figure 30. Depth profile of an unannealed 3000 A^o carbon coated Nitinol sample.

3000 A^o carbon coated samples. It is illustrated how carbon is concentrated at the surface, and then its concentration drops after the carbon/Nitinol interface. On the other hand, both nickel and titanium are concentrated in the bulk of the material, and are depleted at the surface of the sample. Considering the carbon film thickness, it is estimated that the sputtering rate of the carbon film was about 250 A^o/min. Figure 31 is an SEM photomicrograph of the argon sputtered surface of an unannealed carbon coated Nitinol sample. The contrast between the carbon coating and the TiNi phase shows a sharp interface area between the carbon film and the substrate.

Auger analysis was also done on 3000 A^o carbon coated samples annealed at 700^{o}C for one hour, three hours, and six hours. Figure 32 (a) and (b) shows the Auger spectrum for the sample annealed for one hour after one minute and 40 minutes argon sputtering, respectively. The depth profile shown in Figure 33 shows that the annealing for one hour at 700^{o}C broadened the TiC region at the carbon/Nitinol interface. Similarly, Figure 34 (a) and (b) shows the Auger spectrum for the sample annealed for three hours after one minute and 40 minutes argon sputtering, respectively. It is clear that the carbon still exists in the elemental form at the surface. Moreover, Figure 35 shows the depth profile of the three hour annealed carbon coated sample. It is clear that the longer heat treatment broadened the TiC region at the carbon/Nitinol interface as compared to one hour

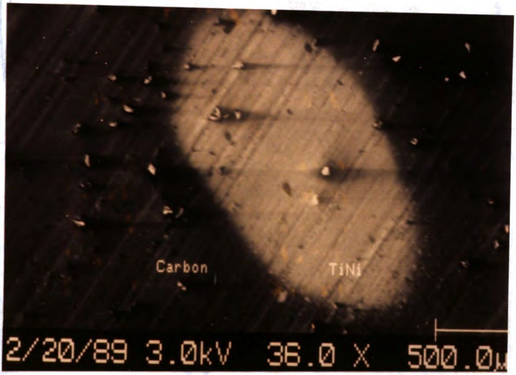

Figure 31. SEM photomicrograph of an unannealed 3000 A^{o} carbon coated Nitinol after 26 minutes argon sputtering.

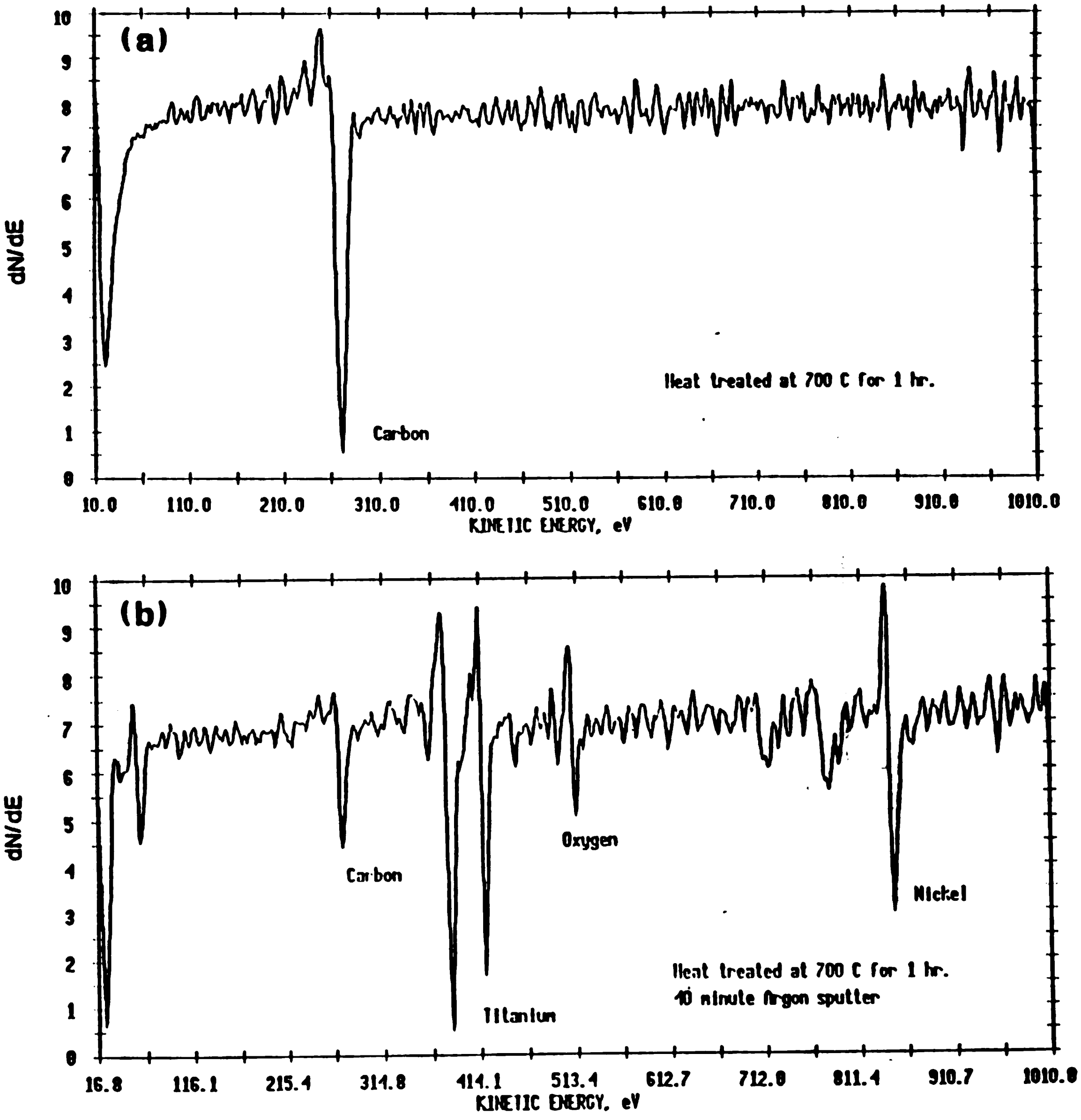

Figure 32. Auger signal of a 3000 A°carbon coated Nitinol sample annealed at 700°C for one hour after coating. (a) One minute argon sputtering (b) 40 minutes argon sputtering.

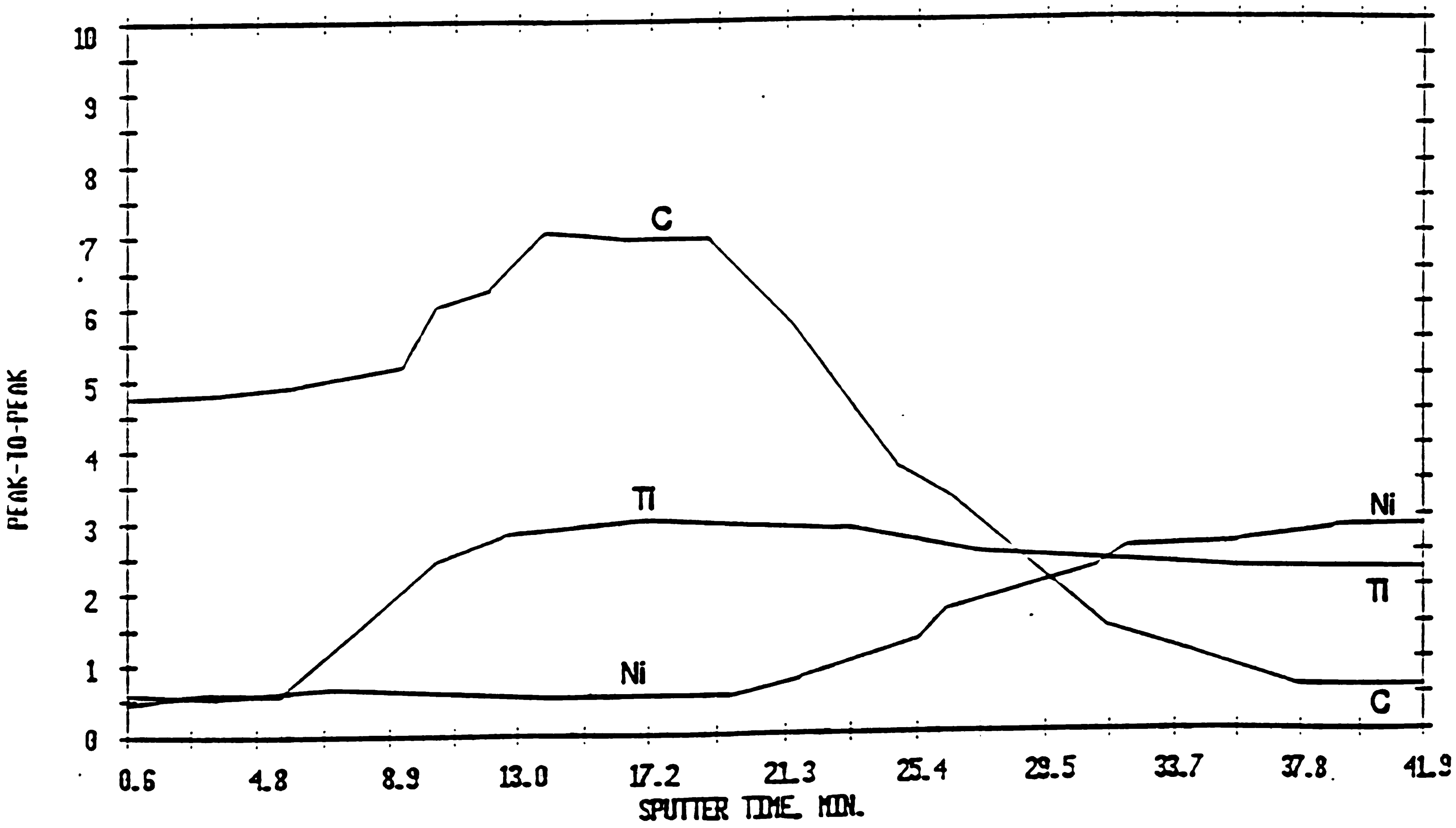

Figure 33. Depth profile of a 3000 A^{o}carbon coated Nitinol annealed at 700^{o}C for one hour.

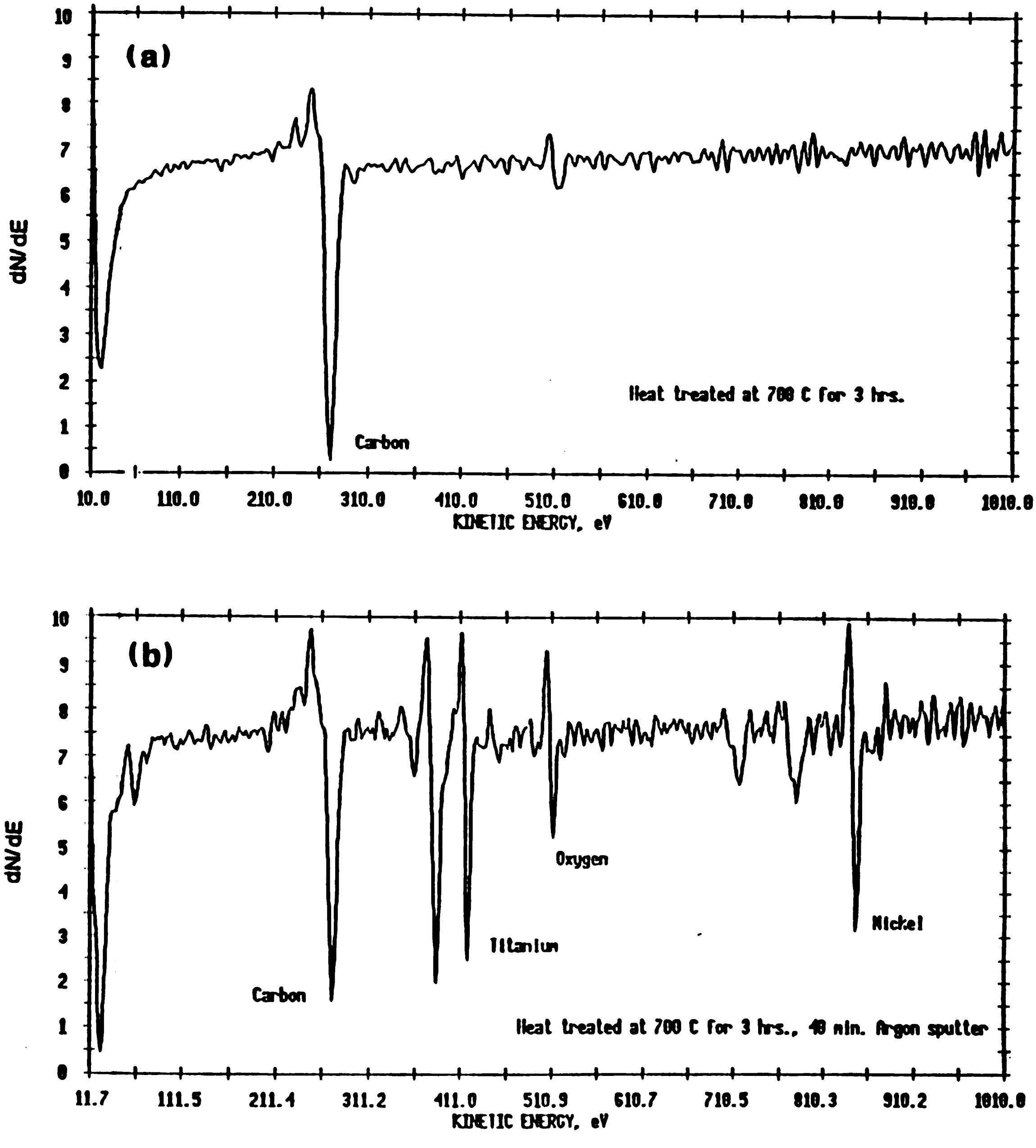

Figure 34. Auger signal of a 3000 A^{o} carbon coated Nitinol sample annealed at 700^{o}C for three hours after coating. (a) One minute argon sputtering (b) 40 minutes argon sputtering.

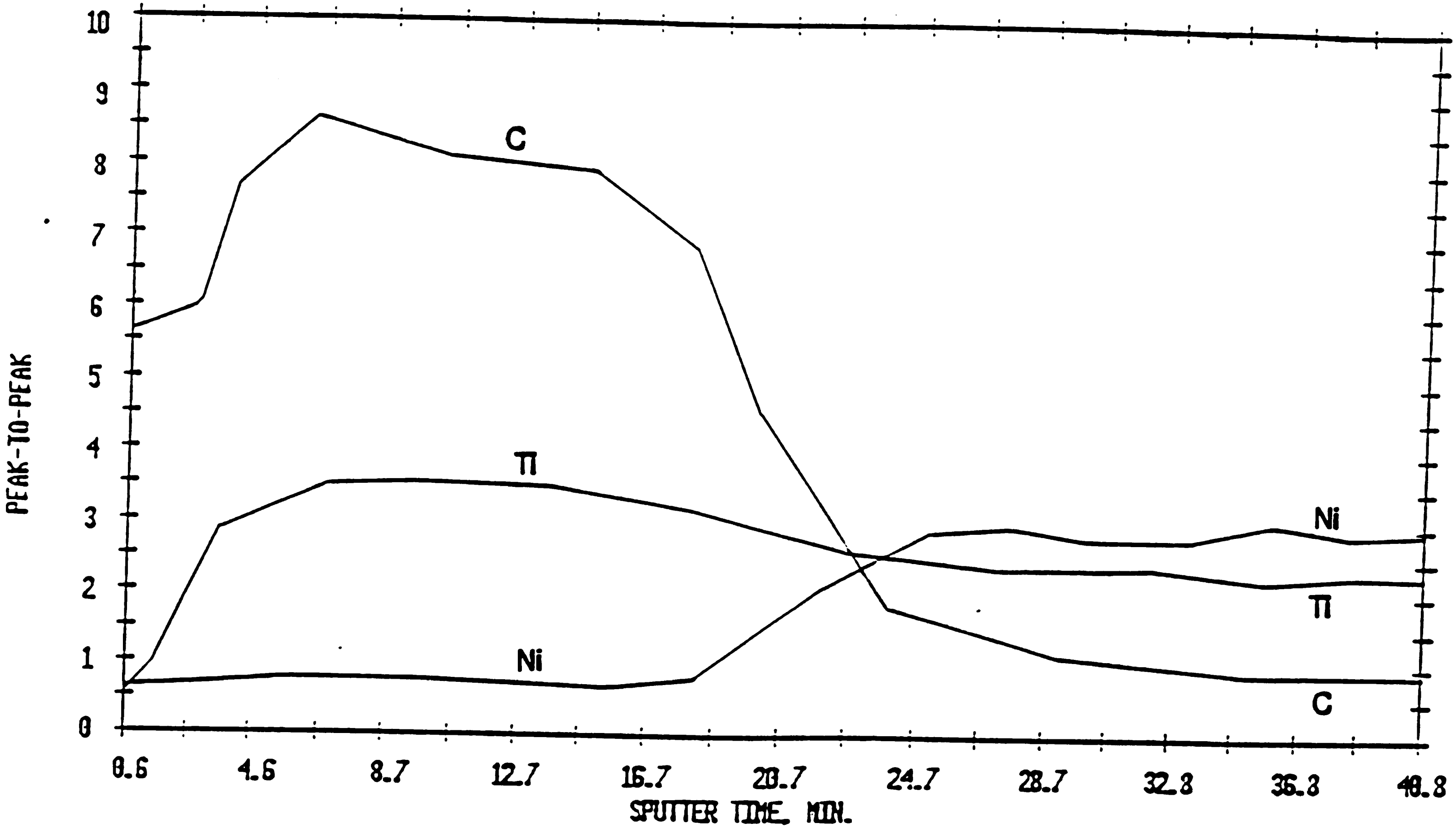

Figure 35. Depth profile of a 3000 A^{o} carbon coated Nitinol sample annealed at 700^{o}C for three hours.

annealing. Figure 36 is an SEM photomicrograph illustrating the presence of TiC at the carbon/Nitinol interface.

A six hour anneal was sufficient to make the 3000 A^{o} carbon film react with the substrate to form at the TiC surface of the Nitinol substrate. This is illustrated in Figure 37 (a) and (b) which shows the Auger spectrum after one minute and 35 minutes argon sputtering, respectively. Analysis of the carbon signals in both Figure (a) and (b) show that it exists in the compound form, TiC. Figure 38, which is a depth profile of the sample, also shows that titanium is present at the surface with carbon.

6. Transmission Electron Microscopy:

Cross sectional specimens of vapour deposited ultra-low temperature isotropic (ULTI) carbon on Nitinol substrates were examined using transmission electron microscopy. The phase transformation of the surface constrained Nitinol was studied in-situ using a cold stage. The major findings of the study were that during martensitic transformation, the last martensite to form was close to the constrained surface. Also, the last martensite formed disappeared first in the reverse transformation. The TEM foil, which is made up of 3000 A^{o} carbon coated Nitinol samples heat treated at 700^{o}C for three hours, was cooled to about 240 K using the TEM cold stage. The temperature of cooling was chosen to be below the M_f temperature to ensure complete martensitic transformation of Nitinol. The cooling was then stopped, and the TEM foil was left to warm up in

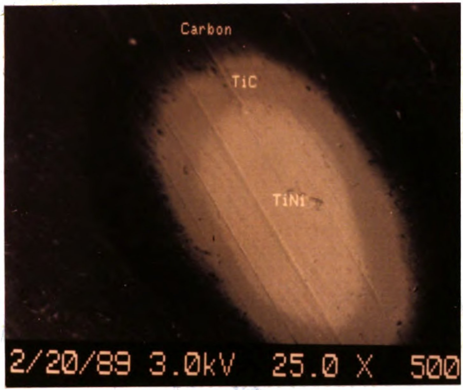

Figure 36. SEM photomicrograph of 3000 A° carbon coated Nitinol annealed at 700°C for three hours after 40 minutes argon sputtering.

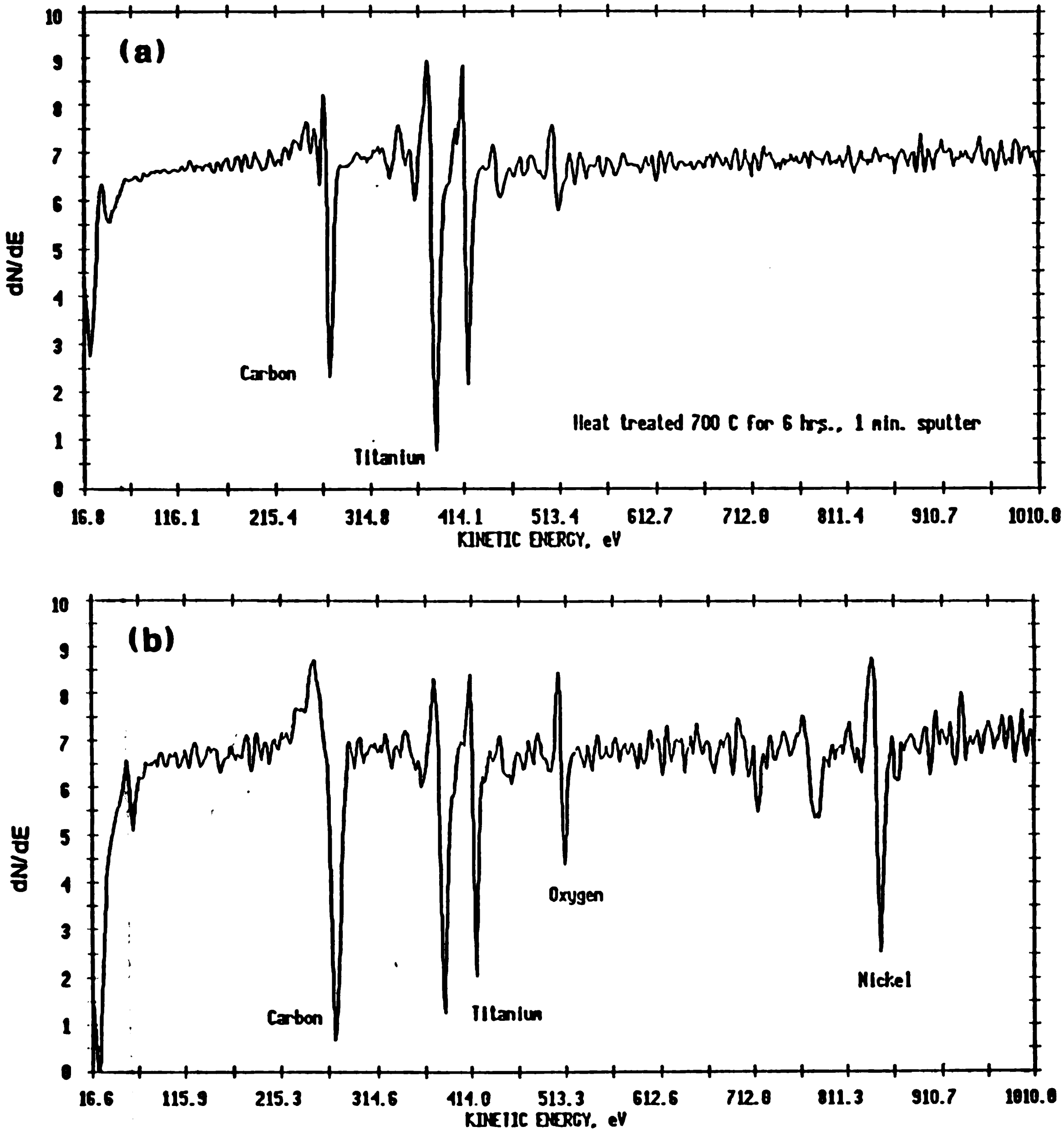

Figure 37. Auger signal of a 3000 A^o carbon coated Nitinol sample annealed at 700^oC for six hours after coating. (a) One minute argon sputtering (b) Thirty five minutes argon sputtering.

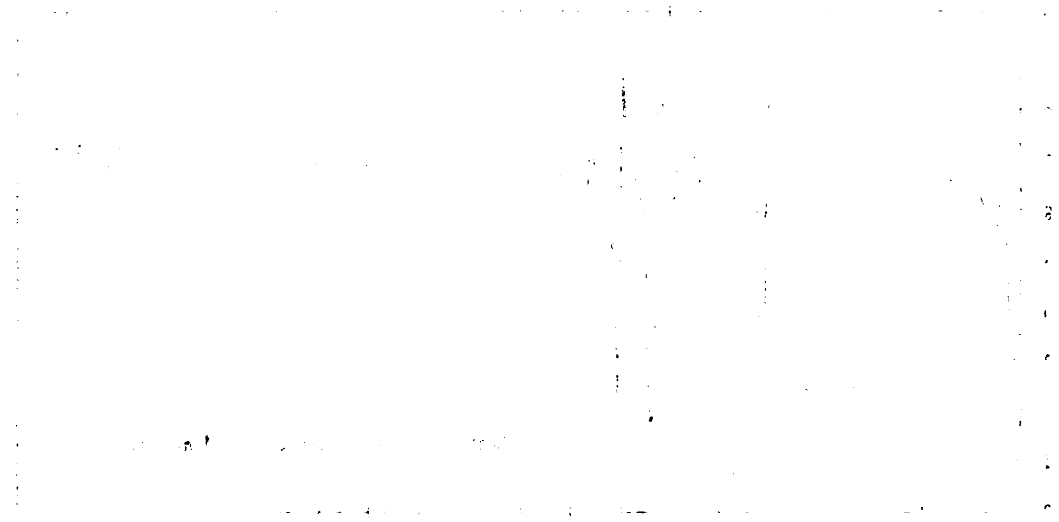

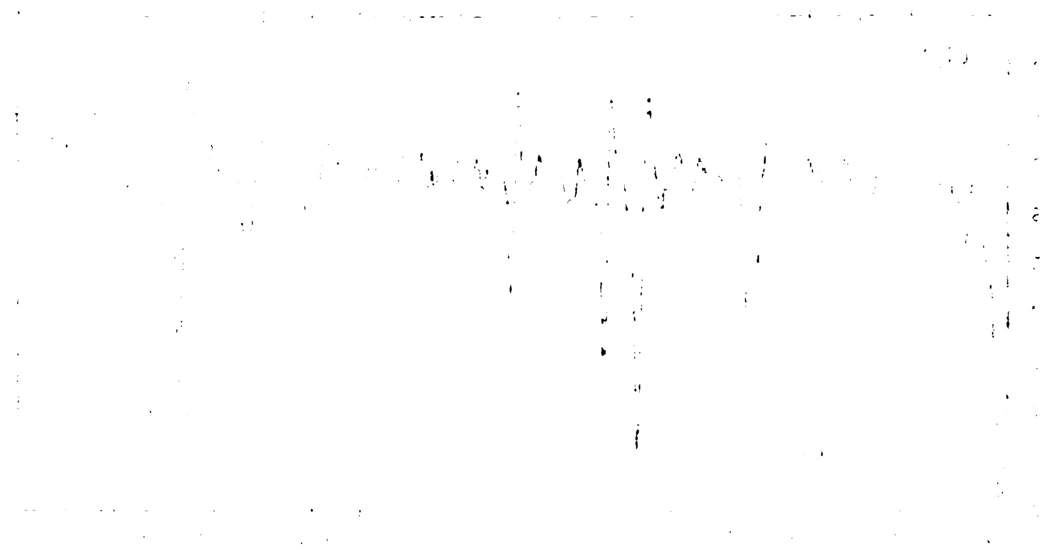

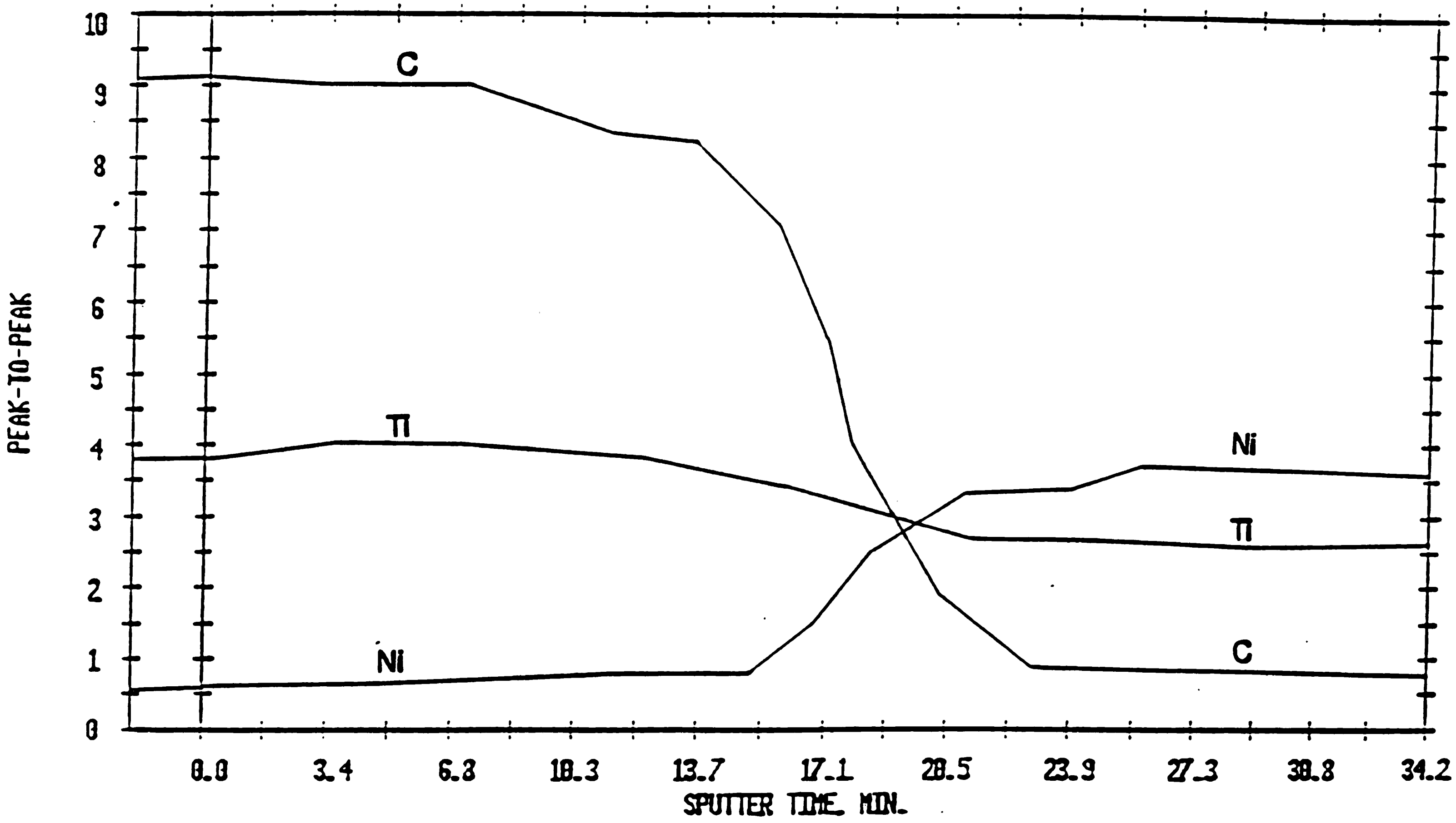

Figure 38. Depth profile of a 3000 A° carbon coated Nitinol sample annealed at 700°C for six hours.

the column to about 300 K. Thus, partial austenitic transformation of the Nitinol occurred. Figures 39 (a) and (b) are bright field images of the vertical cross-section TEM foil at about 300 K. The micrographs (Figure 39 (a) and (b)) show lathes of martensite present in the bulk of the Nitinol sample, away from the constrained surface at that temperature. Figure 40 is an electron diffraction pattern, $[1\bar{1}0]_m$, of the martensitic phase at about 240 K, and Figure 41 is the analysis of the $[1\bar{1}0]_m$ electron diffraction pattern.

Transmission electron microscopy was also used to examine the microstructures of both the carbon thin film vapour deposited on the Nitinol substrates, and the TiC formed at the carbon/Nitinol interface in the heat treated samples. Figure 42 shows the microstructure of a carbon flake in a vertical cross-section TEM foil for a 3000 A^o carbon coated unannealed Nitinol samples. Figure 43 shows the electronc diffraction pattern of the carbon flake. Since the structure of carbon is semicrystalline (turbostratic), a ring pattern appears rather than diffraction spots. The inner ring corresponds to the angular position of (100) in graphite crystals while the outer ring corresponds to the (002).

The TiC formed at the carbon/Nitinol interface was investigated with an examination of a horizontal cross-section TEM foil of a 3000 A^o carbon coated Nitinol sample heat treated at 700^{o}C for three hours. Figures 44 and 45 show the microstructure of TiC and the electron diffraction

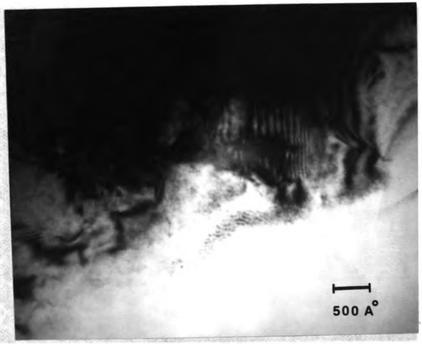

(a)

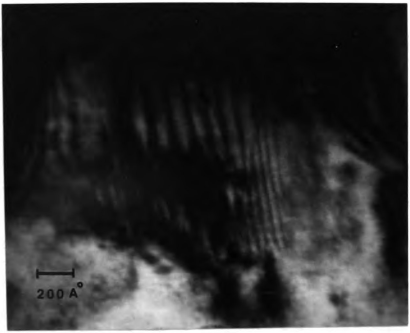

(b)

Figure 39. Bright field image of a vertical cross-section TEM foil of a 3000 A^{O} carbon coated Nitinol sample heat treated at 700^{O}C for 3 hours (a) 200,000 x, (b) 500,000 x.

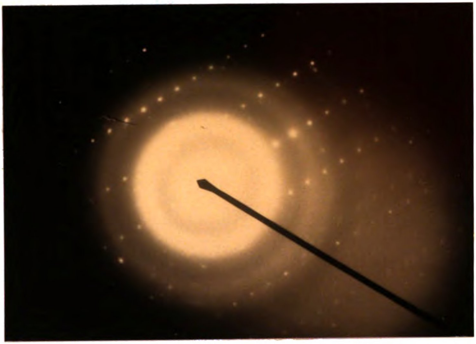

Figure 40. Electron diffraction pattern of Nitinol in the martensitic phase, $[1\bar{1}0]_m$.

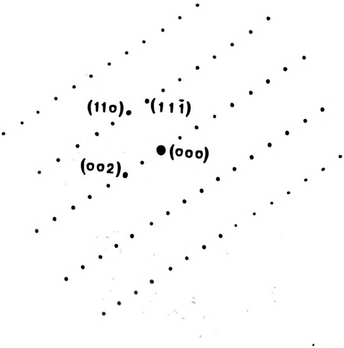

Figure 41. Analysis of the electron diffraction pattern of Nitinol in the martensitic phase, $[1\bar{1}0]_m$.

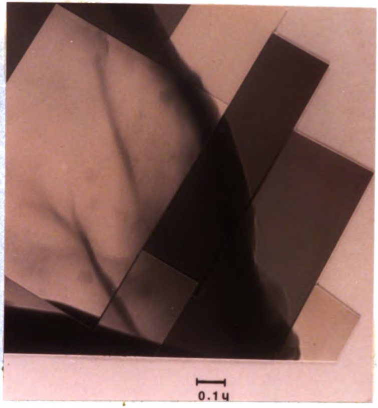

Figure 42. Bright field image of a carbon flake.

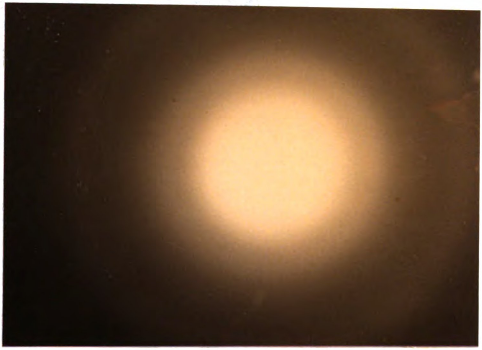

Figure 43. Electron diffraction pattern of a carbon flake.

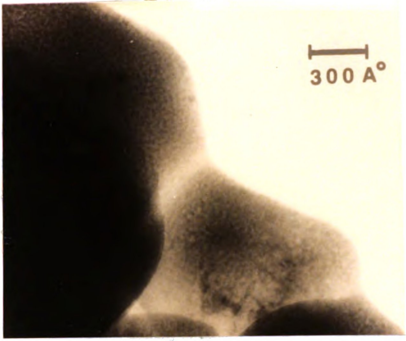

Figure 44. Bright field image of TiC.

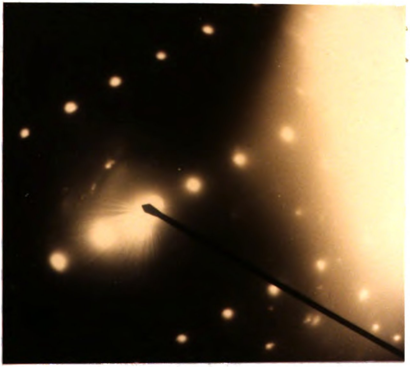

Figure 45. Electron diffraction pattern of TiC, $[123]_{TiC}$.

pattern, $[123]_{TiC}$, corresponding to it, respectively.

B. Biologic Evaluation of the Carbon Coated Nitinol

The objective of the biologic study was to evaluate the induced growth of collagenous tissue on non-annealed carbon coated Nitinol surfaces. Carbon coated Nitinol filaments, 0.076 mm in diameter, were incorporated into the fascia lata which replaced the anterior cruciate ligament in a canine's stifle joint. Figure 46 (a) and (b) show part of the surgical procedure followed. Figure 46 (a) shows the fascia lata before incorporating the carbon coated filament into it, and Figure 46 (b) shows the process of drilling a tunnel in the femur through which the fascia lata would be pulled. Radiographs were also taken for the carbon coated Nitinol filaments in the canine's stifle joint. Figure 47 (a) and (b) shows the anterior-posterior and lateral-medial views of the operated knee joint, respectively.

Thirty days post-operatively, the canine was euthanized, and the stifle joint was harvested. Scanning electron microscopy examination of a wire section taken from the fascia lata secured on the patellar tendon during surgery showed the presence of islands of reticular collagen on the surface of the carbon coated filaments. This is illustrated in Figures 48 (a) and (b) which are SEM photomicrographs of collagenous tissue over carbon coated filaments harvested from an area adjacent to the patellar tendon. However, histological evaluation at a magnification of 100X could not reveal whether fibrocytes were formed on

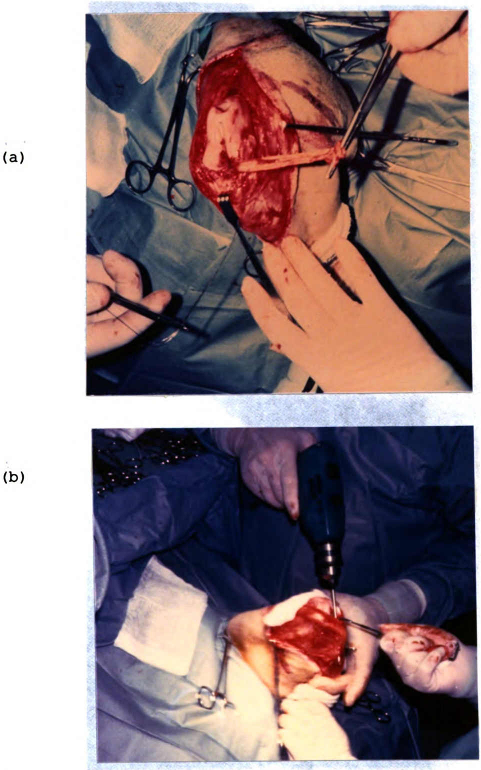

Figure 46. Photographs illustrating part of the surgical procedure followed in the study. (a) Fascia lata before pulling it through the tibia, (b) drilling a tunnel in the tibia.

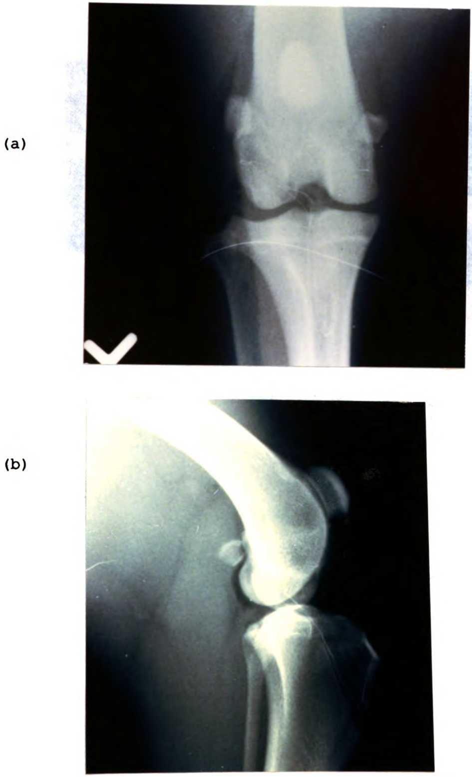

Figure 47. Radiographs showing the carbon coated Nitinol filaments in the canine’s stifle joint. (a) Anterior-posterior view, (b) lateral-medial view.

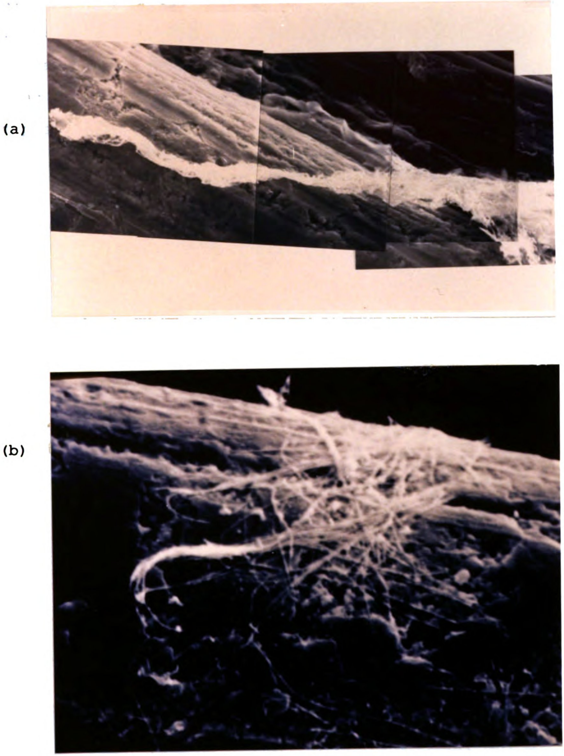

Figure 48. SEM photomicrographs of collagen islands on the surface of carbon coated Nitinol filaments. (a) 1000 X (b) 1000 X.

the carbon coated filaments in either the transverse section or the longitudinal section as shown in Figure 49 (a) and (b), respectively. Thus, it is not conclusive whether the reticular collagen viewed by SEM was induced by the carbon coating, or occurred as a result of tissue healing in the knee post-operatively.

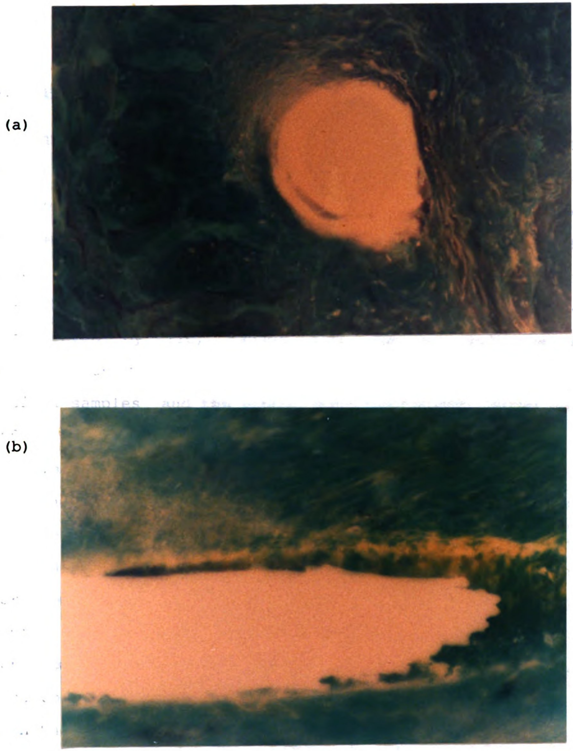

Figure 49. Optical photographs illustrating the carbon coated Nitinol filaments in tissue. (a) Transverse section, (b) longitudinal section.

V. DISCUSSION

A. Phase Transformation of Nitinol

The objective of this research work was to study the effect of surface constraint on the phase transformation of Nitinol, with application to the design of a prosthesis for the reconstruction of the anterior cruciate ligament. The phase transformation studies showed that the constraint in the 3000 A^o carbon coated and annealed Nitinol samples, represented by TiC, caused both the M_f and the A_s temperatures to drop markedly. The thicknesses of the Nitinol samples and the vapour deposited carbon films were 600 μm, and 0.3 μm (3000 A^o), respectively.

The transformation peaks of the thermally cycled coated and uncoated Nitinol samples were analyzed. The 9900 computer/thermal analyzer with which the differential scanning calorimeter is equipped, was used in the analysis. For every peak in the heating or cooling cycle of the Nitinol sample tested, the percentage of the area under the curve as a function of temperature was plotted. The plot also corresponded to the percentage of phase transformed in both the cooling and heating cycles. The analysis with this method was done for the transformation peaks of the coated and uncoated samples on the first cycle of heating and cooling. Since there was no distinct difference in the

transformation peaks of the unannealed samples, the analysis was only performed for the coated and uncoated samples that were annealed at 700°C for three and six hours. Figures 50 and 51 show the effect of surface constraint on the phase transformation of Nitinol for samples annealed at 700°C for three and six hours, respectively. Both figures represent mapping of the percentage of martensitic phase present in the heating and cooling cycles as a function of temperature. A distinctive characteristic of the figures is how the surface constraint causes the A_s and M_f temperatures to drop markedly. Consequently, the annealed coated samples undergo a certain degree of supercooling to complete the transformation, although both the M_s and A_f remain unchanged.

It is significant to point out that the phase transformation of Nitinol will be affected by the ratio of constraint thickness to sample's thickness. This can be illustrated by comparing the DSC results for unannealed and annealed carbon coated Nitinol samples. In the first case, the TiC layer present at the carbon/Nitinol interface is too thin compared to the substrate's thickness to affect its transformation. In the latter case, it was shown that the more the time of annealing, the thicker was the TiC layer formed at the interface, and thus the more was the effect of the constraint. on the phase transformation.

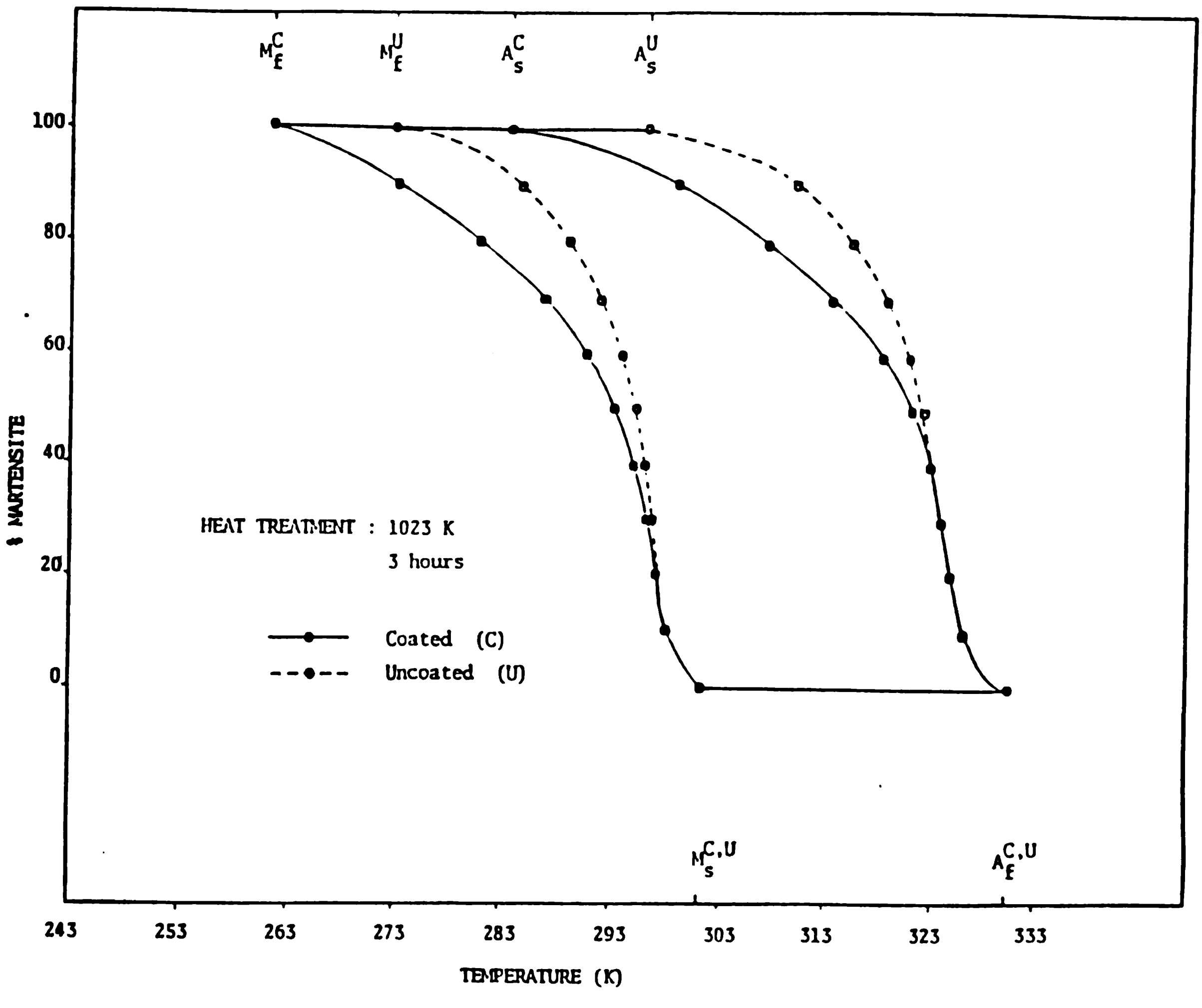

Figure 50. Percent of martensite as a function of temperature for 3000 A^o carbon coated Nitinol samples heat treated at 700^{o}C for three hours.

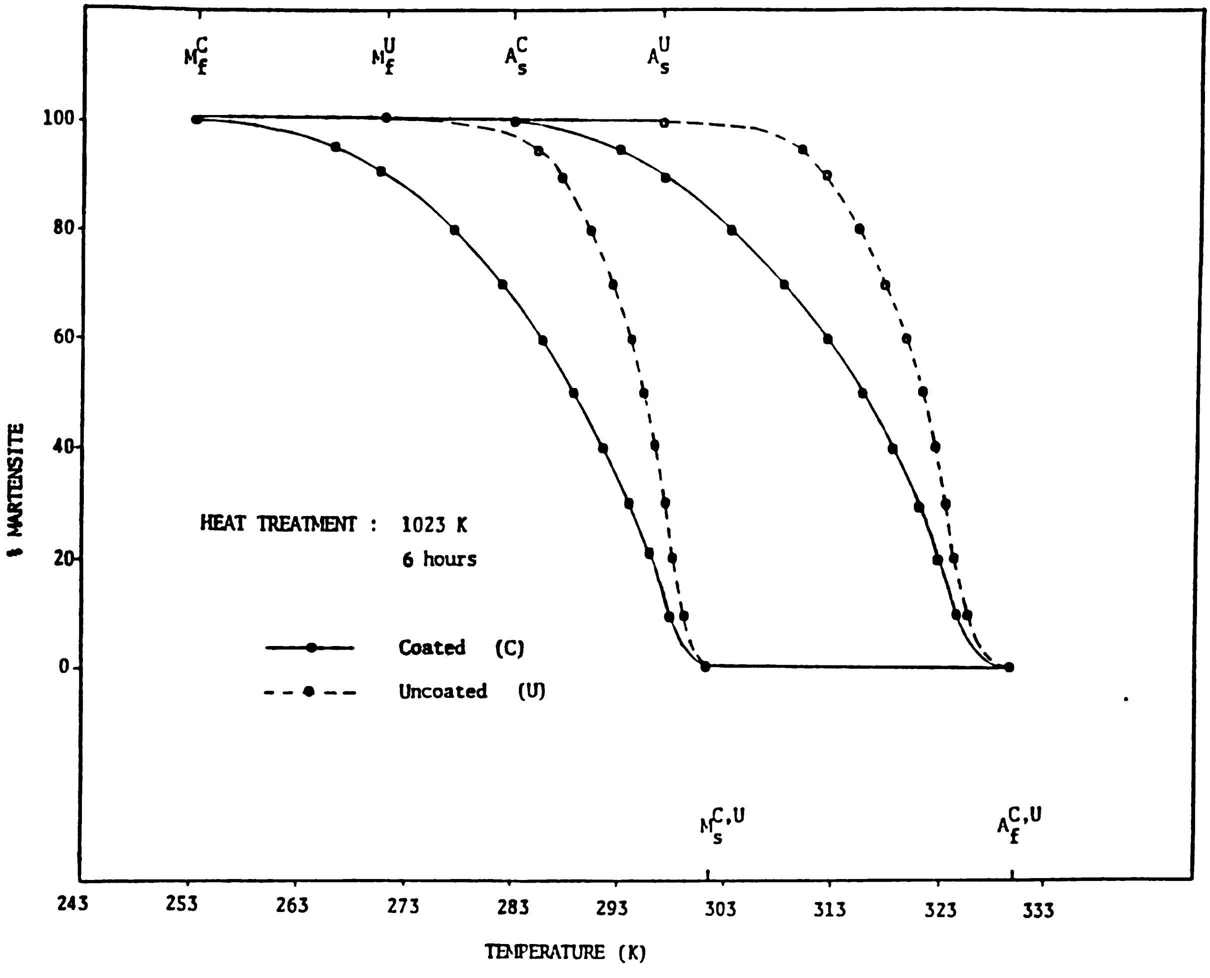

Figure 51. Percent of martensite as a function of temperature for 3000 A^o carbon coated Nitinol samples heat treated at 700^{o}C for six hours.

1. Mathematical Analysis of the Transformation Data

Mathematical analysis was performed on the percentage of phase transformed versus temperature data. A mathematical empirical formula was obtained to fit the experimental data. The formula was of the exponential form:

$$1 - f = A \exp(-B(M_s - T)) \qquad (5)$$

for the martensitic transformation, and

$$f = A \exp(-B(A_f - T)) \qquad (6)$$

for the reverse transformation, where

f is the fraction of martensitic phase present at the specific temperature (T),

$1 - f$ is the fraction of austenitic phase present at the specific temperature (T),

and

A, B are constants.

Figure 52 (a) and (b) represents a comparison of the percentage of the amount of austenitic phase present in uncoated and coated samples as a function of temperature during the first cooling cycle. The figures show the percentage transformed for the samples heat treated at 700°C for three hours and six hours, respectively. Similarly, Figure 53 (a) and (b) represent a comparison of the amount of austenitic phase present in uncoated and coated samples as a function of temperature during the first heating cycle. The figures show the percentage transformed for the samples heat treated at 700°C for three and six hours, respectively. In Figures 52 and 53, solid lines represent the empirical

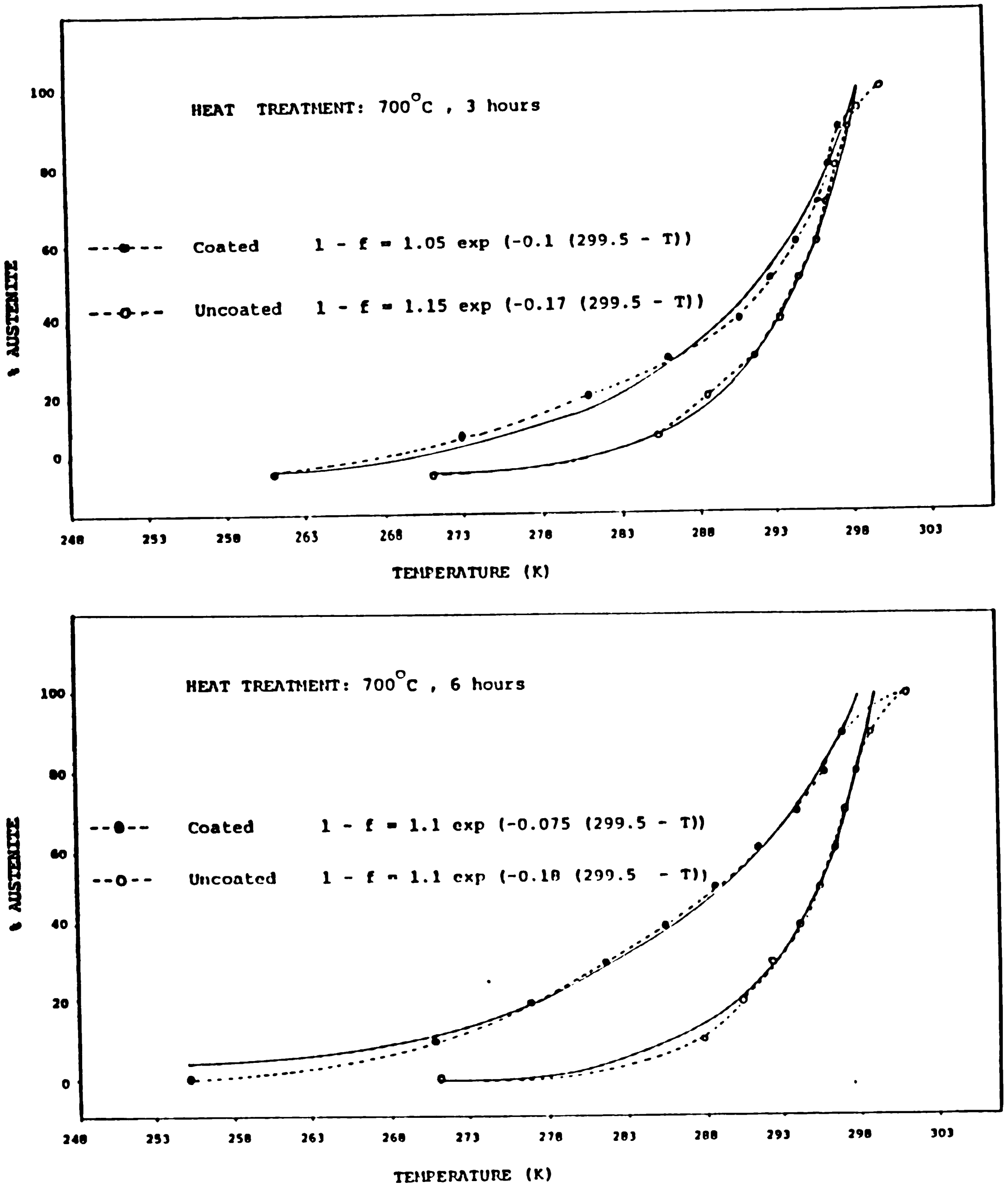

Figure 52. Percent of austenite present as a function of temperature in the first cooling cycle for coated and uncoated Nitinol samples heat treated at 700°C for (a) three hours (b) six hours.

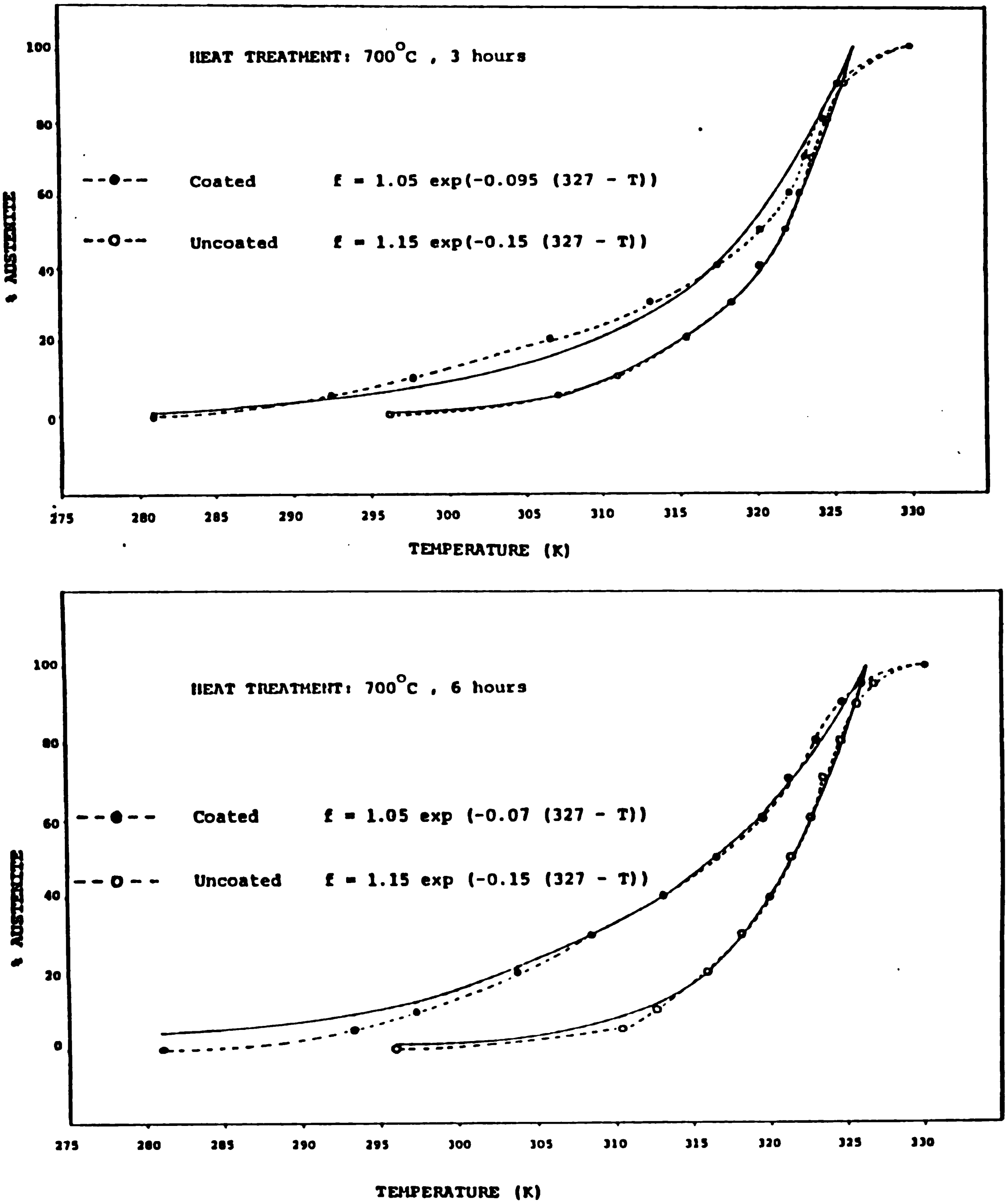

Figure 53. Percent of austenite present as a function of temperature in the first heating cycle for coated and uncoated Nitinol samples heat treated at 700°C for (a) three hours (b) six hours.

values obtained mathematically to fit the experimental data. The experimental results could be represented by two exponential functions, one of which is only effective about two to three degrees below the M_s or the A_f temperatures. For simplification, one exponential term was used. Thus, the M_s and A_f temperatures used in equations (5) and (6) are one and three degrees, respectively, lower than the actual M_s and A_f values obtained from the experimental results. The experimental and calculated data of the percentage of austenite present as a function of temperature are tabulated in Appendices 1 and 2 for uncoated and coated samples heat treated at 700°C for three and six hours, respectively.

Equations 5 and 6 describe empirically the fraction of austenite present in the martensitic and reverse transformation, respectively, as a function of temperature. However, as shown in Appendix 1 and 2, the values of the constants A and B varied with the experimental conditions such as the direction of transformation, the annealing time of the uncoated or coated samples, and the presence of surface constraint. Accordingly, it was deduced that the constants A and B can be expressed in terms of physical or thermodynamic parameters. These parameters differ from one sample to the other depending on the sample's thermomechanical history and the experimental conditions under which it was tested. To find these parameters in the martensitic transformation, equation (4) was employed.

$$f = \frac{1}{\Delta H_T} \int_T^{M_s} \frac{\partial \Delta H}{\partial T} \, dT \qquad (4)$$

where,

f is the fraction of martensite transformed,

and

ΔH_T is the total heat of transformation of the reaction. It is important to note that in these derivatives that the subscript, T, does not signify a dependency on temperature.

Based on experimental curve fitting, a functional form of the following type is proposed:

$$\frac{\partial \Delta H}{\partial T} = k_1 \, e^{-a_1(M_s - T)} - k_2 \, e^{-a_2(M_s - T)} \qquad (7)$$

where,

$a_1 << a_2$

and

$$1 - \frac{k_1}{\Delta H_T a_1} + \frac{k_2}{\Delta H_T a_2} = 0 \qquad (8)$$

Substitution of (7) into (4) yields

$$f = \frac{1}{\Delta H_T} \int_T^{M_s} \left[k_1 e^{-a_1(M_s - T)} - k_2 e^{-a_2(M_s - T)} \right] dT \qquad (9)$$

$$= \frac{1}{\Delta H_T} \left[\frac{k_1}{a_1} (1 - e^{-a_1(M_s - T)}) - \frac{k_2}{a_2} (1 - e^{-a_2(M_s - T)}) \right] \qquad (10)$$

$$1 - f = 1 - \frac{k_1}{\Delta H_T a_1} (1 - e^{-a_1(M_s - T)}) + \frac{k_2}{\Delta H_T a_2} (1 - e^{-a_2(M_s - T)}) \qquad (11)$$

Since $a_1 << a_2$, experimental results suggest that for

$T << M_s$, we have $e^{-a_2(M_s - T)} \approx 0$

$$1 - f \approx 1 - \frac{k_1}{\Delta H_T a_1} (1 - e^{-a_1(M_s - T)}) + \frac{k_2}{\Delta H_T a_2} \qquad (12)$$

Substitution of (8) in (12) yields

$$1 - f = \frac{k_1}{\Delta H_T a_1} (e^{-a_1(M_s - T)}) \qquad (13)$$

The assumption in equation (8) is justified by the fact that equation (13) agrees with the experimental results, as it will be shown later.

From experimental results, it was found out that

$$a_1 = \frac{\Delta H_T}{R(M_s - M_f)^2} \qquad (14)$$

and

$$\frac{k_1}{\Delta H_T a_1} = \alpha \approx 1 \qquad (15)$$

where,

α is a unitless term close to unity depending on the accuracy of the experimental data

$$\therefore k_1 = \frac{\alpha}{R}\left[\frac{\Delta H_T}{M_s - M_f}\right]^2 \qquad (16)$$

From our understanding of activated processes, we know that an expression of the following form can be written for the kinetics of a transformation reaction:

$$1 - f = \alpha\, e^{-Q/RT}$$

where,

$$Q = \Delta H_T$$

and

R = gas constant

We propose to define a normalized temperature, T_n

where

$$T_n = \frac{M_s - T}{M_s - M_f}$$

and the kinetic equation takes the form

$$1 - f = \alpha\, e^{\frac{-\Delta H_T}{R(M_s - M_f)} T_n}$$

which can also be written as:

$$1 - f = \alpha\, e^{\frac{-\Delta H_T(M_s - T)}{R(M_s - M_f)^2}} \qquad (17)$$

for the martensitic transformation.

Similarly, for the reverse transformation,

$$f = \frac{k_1}{\Delta H_T a_1} \left(e^{-a_1(A_f - T)}\right) \qquad (18)$$

where, from our experimental findings

$$a_1 = \frac{\Delta H_T}{R(A_f - A_s)^2} \tag{19}$$

and,

$$k_1 = \frac{\alpha}{R} \left[\frac{\Delta H_T}{A_f - A_s}\right]^2 \tag{20}$$

If we assume a normalized temperature T_m where,

$$T_m = \frac{A_f - T}{A_f - A_s} .$$

∴ the kinetic equation takes the form

$$f = \alpha e \ \frac{- \Delta H_T}{R(A_f - A_s)} \ T_m$$

which can also be written as

$$f = \alpha e^{\frac{- \Delta H_T}{R(A_f - A_s)^2} (A_f - T)} \tag{21}$$

for the martensite to parent phase transformation.

2. Driving Force of Phase Transformation in Nitinol

Both the martensitic and reverse transformation of Nitinol are characterized by no chemical compositional change associated with them. Thus, both the parent and the martensitic phase are considered to be a single component system [100]. Figure 54 is a schematic representation of the molar Gibbs chemical free energy for both the parent phase (P) and the martensitic phase (M) as a function of temperature. The figure illustrates that there exists a single equilibrium temperature, T_o, at which the difference in chemical free energy between the two phases is equal to zero ($\Delta G^{P-M} = 0$) [100].

For the martensitic transformation to proceed, ΔG^{P-M} has to be negative, i.e. $G^M_m < G^P_m$. It would be expected that the transformation would start at a temperature less than, but very close to, T_o. However, due to the presence of opposing elastic energies that are positive in magnitude, the Nitinol undergoes supercooling below T_o. The supercooling continues until the chemical driving force, which is negative in magnitude, overcomes the opposing non-chemical energies. Once a net negative energy is reached, the martensitic transformation starts, and the temperature at which this occurs is designated as M_s. The chemical driving force continues to increase from M_s to M_f at which the transformation is complete [100]. Similarly, in the reverse transformation, superheating above T_o is required. The superheating allows the chemical driving force to

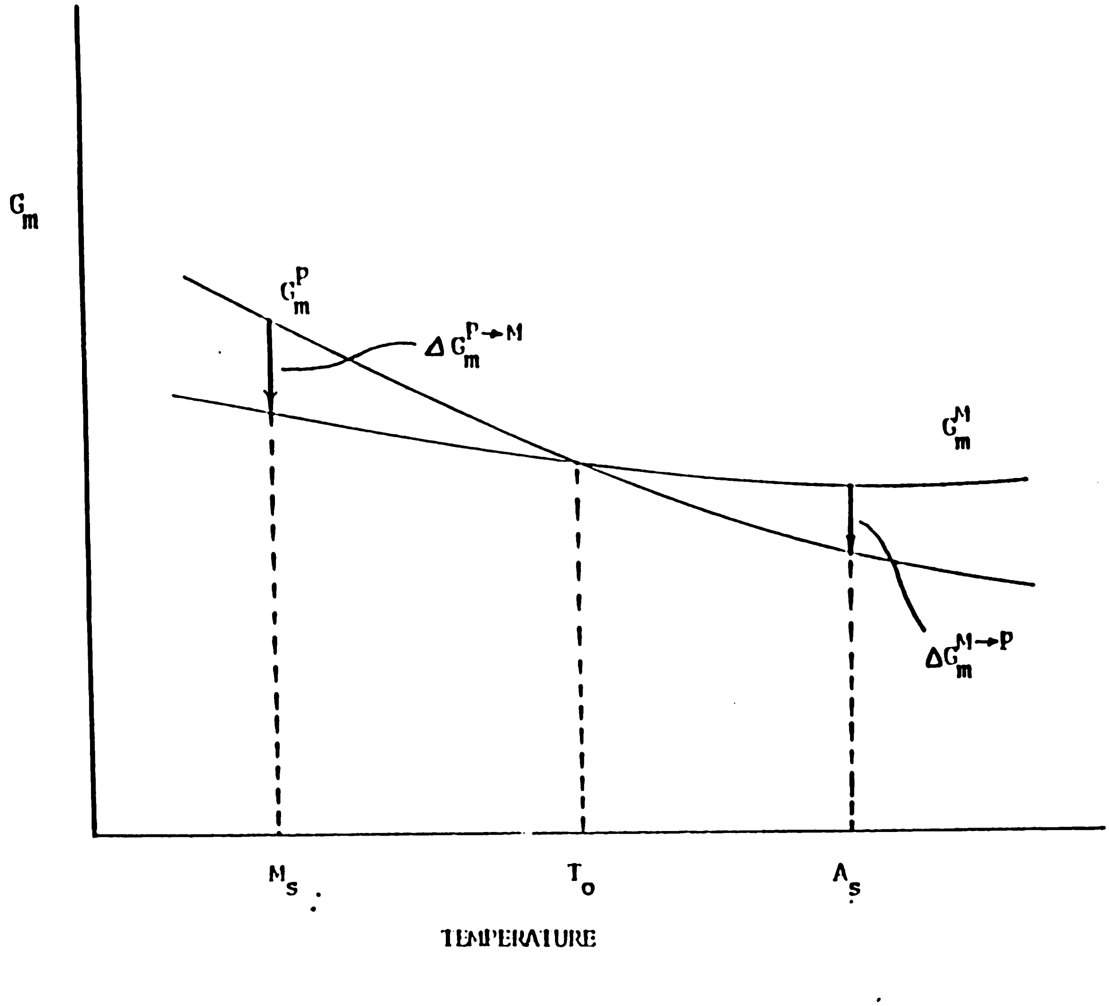

Figure 54. Schematic representation of G_m as a function of temperature [100].

overcome the non-chemical energies. Thus, the transformation starts at the A_s temperature and is complete at the A_f temperature. Moreover, the chemical driving force increases from A_s to A_f.

Equations (13) and (18) were derived to express the fraction of the parent phase present as a function of temperature during the martensitic and the reverse transformation, respectively. The heat of transformation at a specific temperature during the heating or cooling cycle is directly associated to a fraction of phase transformed. Thus, the driving force for the martensitic transformation or the reverse transformation can be calculated.

a. <u>Driving Force Calculations of the Martensitic Transformation</u>

$$1 - f = \frac{k_1}{\Delta H_T a_1} e^{-a_1(M_s - T)} \qquad (13)$$

$$f = 1 - \frac{k_1 \; e^{-a_1(M_s - T)}}{\Delta H_T \; a_1}$$

Also,

$$\Delta H_T(f) = \Delta H \qquad (22)$$

where ΔH_T is the total heat of transformation,

and ΔH is the integrated enthalpy from the temperature T to M_s.

$$f\ \Delta H_T = \Delta H_T - \frac{k_1}{a_1}\ e^{-\ a_1\ (M_s - T)}$$

$$\Delta H = \Delta H_T - \frac{k_1}{a_1}\ e^{-a_1 M_s}\ e^{a_1 T} \tag{23}$$

Using the Gibbs-Helmholtz equation

$$\frac{\partial(\Delta G/T)}{\partial T} = -\ \frac{\Delta H}{T^2} \tag{24}$$

$$\frac{\partial(\Delta G/T)}{\partial T} = \frac{-\Delta H_T}{T^2} + \frac{k_1}{a_1}\ e^{-a_1 M_s}\ \frac{e^{a_1 T}}{T^2} \tag{25}$$

$$\left.\frac{\Delta G}{T}\right|_T^{M_s} = + \left.\frac{\Delta H_T}{T}\ \right|_T^{M_s} + \frac{k_1 e^{-a_1 M_s}}{a_1} \int_T^{M_s} \frac{e^{a_1\ T}}{T^2}\ dT \tag{26}$$

$$\left.\frac{\Delta G}{T}\right|_{M_s} - \left.\frac{\Delta G}{T}\right|_T = + \frac{\Delta H_T}{M_s} - \frac{\Delta H_T}{T} + \frac{k_1 e^{-a_1 M_s}}{a_1} \int_T^{M_s} \frac{e^{a_1\ T}}{T^2}\ dT \tag{27}$$

At M_s , $\Delta G = 0$

$$\int_T^{M_s} \frac{e^{a_1 T}}{T^2}\ dT = -\ \left.\frac{e^{a_1\ T}}{T}\ \right|_T^{M_s} + a_1 \int_T^{M_s} \frac{e^{a_1\ T}}{T}\ dT \tag{28}$$

$$\therefore \int_T^{M_s} \frac{e^{a_1 T}}{T^2}\, dT = -\frac{e^{a_1 M_s}}{M_s} + \frac{e^{a_1 T}}{T} + a_1 \int_T^{M_s} \frac{e^{a_1 T}}{T}\, dT \qquad (29)$$

But

$$\int_T^{M_s} \frac{e^{a_1 T}}{T}\, dT = \ln\left(\frac{M_s}{T}\right) + \sum_{i=1}^{\infty} \frac{(a_1)^i (M_s^i - T^i)}{i \cdot i!} \qquad (30)$$

which is not a closed form integral. Thus, the integral

$\int_T^{M_s} \frac{e^{a_1 T}}{T}\, dT$ was calculated using the trapezoid rule of integration, and is tabulated in Appendices 3 and 4.

$$-\frac{\Delta G}{T} = +\frac{\Delta H_T}{T} - \frac{\Delta T_T}{T} + \frac{k_1 e^{-a_1 M_s}}{a_1} \left[-\frac{e^{a_1 M_s}}{M_s} + \frac{e^{a_1 T}}{T} + a_1 \int_T^{M_s} \frac{e^{a_1 T}}{T}\, dT \right] \qquad (31)$$

But, the martensitic transformation is an exothermic reation. Thus, both ΔH_T and k_1 are assigned negative signs.

$$\therefore \Delta G = \frac{\Delta H_T \, T}{M_s} - \Delta H_T - \frac{k_1 T}{a_1 M_s} + \frac{k_1}{a_1} e^{-a_1(M_s - T)}$$

$$+ k_1 T \, e^{-a_1 M_s} \int_T^{M_s} \frac{e^{a_1 T}}{T} \, dT \qquad (32)$$

The values for the driving force of the martensitic transformation of (ΔG) of constrained and unconstrained samples in given in Appendices 3 and 4.

b. <u>Driving Force Calculations for the Martensite to Parent Phase Transformation</u>

From equation (18):

$$1 - f = 1 - \frac{k_1}{\Delta H_T a_1} \left(e^{-a_1(A_f - T)}\right) \qquad (33)$$

$$\text{since,} \quad \Delta H_T (1 - f) = \Delta H \qquad (22)$$

$$\therefore \Delta H = \Delta H_T - \frac{k_1}{a_1} e^{-a_1(A_f - T)} \qquad (34)$$

Applying the Gibbs-Helmholtz equation

$$\frac{\partial(\Delta G/T)}{\partial T} = -\frac{\Delta H}{T^2} \qquad (24)$$

$$\frac{\partial(\Delta G/T)}{\partial T} = -\frac{\Delta H_T}{T^2} + \frac{k_1}{a_1T^2}\, e^{-a_1(A_f-T)} \qquad (35)$$

$$\left.\frac{\Delta G}{T}\right|_{A_f} - \left.\frac{\Delta G}{T}\right|_{T} = -\int_T^{A_f} \Delta H_T \frac{dT}{T^2} + \int_T^{A_f} \frac{k_1}{a_1}\, e^{-a_1A_f} \frac{e^{a_1T}}{T^2}\, dT \qquad (36)$$

$$= \left.\frac{\Delta H_T}{T}\right|_T^{A_f} + \frac{k_1}{a_1}\, e^{-a_1A_f} \int_T^{A_f} \frac{e^{a_1T}}{T^2}\, dT \qquad (37)$$

$$\frac{T}{A_f}\, \Delta G_{A_f} - \Delta G_T = \frac{\Delta H_T T}{A_f} - \Delta H_T$$

$$+ \frac{k_1T}{a_1}\, e^{a_1A_f} \left[-\frac{e^{a_1A_f}}{A_f} + \frac{e^{a_1T}}{T} + a_1 \int_T^{A_f} \frac{e^{a_1T}}{T}\, dT \right] \qquad (38)$$

$$\therefore \frac{T}{A_f}\, \Delta G_{A_f} - \Delta G_T = \frac{\Delta H_T T}{A_f} - \Delta H_T - \frac{k_1T}{a_1A_f} + \frac{k_1}{a_1}\, e^{-a_1(A_f-T)}$$

$$+ k_1Te^{-a_1A_f}\int_T^{A_f} \frac{e^{a_1T}}{T}\, dT \qquad (39)$$

ΔG_{A_f} can be calculated using the condition,

$$\Delta G_T = 0 \quad \text{at } A_s$$

With ΔG_{A_f} known, ΔG_T can be calculated from:

$$\Delta G_T = \frac{T}{A_f}\Delta G_{A_f} - \frac{\Delta H_T T}{A_f} + \Delta H_T + \frac{k_1 T}{a_1 A_f} - \frac{k_1}{a_1} e^{-a_1(A_f - T)}$$

$$- k_1 T e^{-a_1 A_f} \int_T^{A_f} \frac{e^{a_1 T}}{T}\, dT \qquad (40)$$

where the integral $\int_T^{A_f} \frac{e^{a_1 T}}{T}\, dT$

was calculated using the trapezoid rule of integration, and is tabulated in Appendices 3 and 4.

The values for the driving force of the constrained and unconstrained samples in the martensite to parent phase transformation is given in Appendices 3 and 4.

The surface constraint was found to affect the driving force. The calculated values of the driving force, G, for the transformation of coated and uncoated samples that were heat treated at 700^{o}C for three and six hours are tabulated in Appendices 3 and 4, respectively. Figures 55 and 56 illustrate the driving force as a function of temperature for the unconstrained and constrained Nitinol samples. Both figures show that for the martensitic transformation, M_s is the same for both the constrained and unconstrained sample. However, as the transformation proceeds, the constraint opposes the driving force in the surface constrained sample, causing it to be lower than that for the unconstrained sample. In order to overcome the constraint and the strain energy associated with it, the constrained sample has to be supercooled to achieve the same driving force required to complete the transformation as in the unconstrained sample. Thus, at any temperature during the martensitic transformation other than M_s, the net driving force for the constrained sample is lower than that for the unconstrained one. Moreover, it is noticed from Figures 55 and 56 that even though the constrained sample is supercooled to lower temperatures, the net driving force at saturation is less than that for the unconstrained sample. This is an indication that complete transformation to martensite in the cooling cycle is never achieved for the constrained sample. It also indicates that for surface constrained samples, martensitic transformation starts at the bulk and proceeds to the surface with the decrease in temperature.

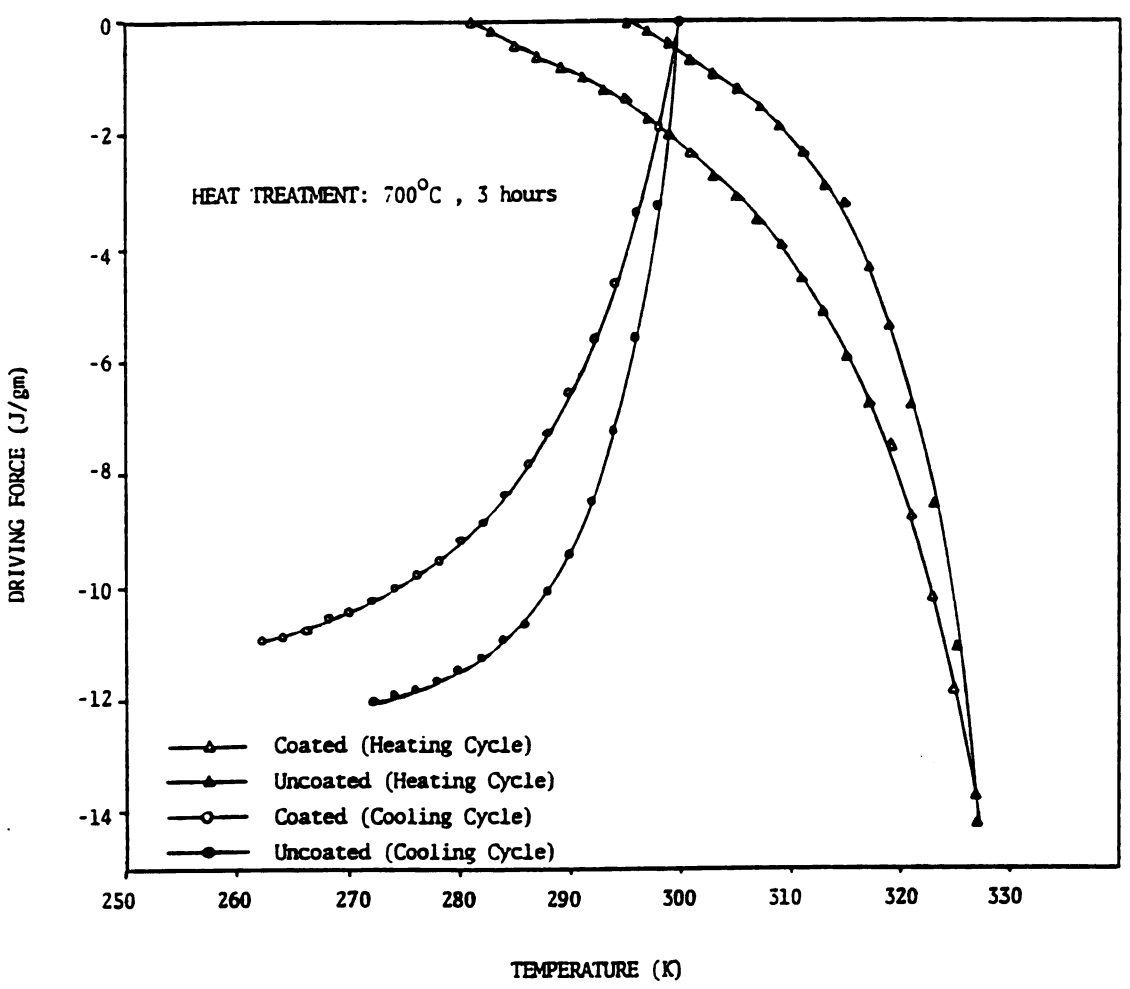

Figure 55. Driving force as a function of temperature for unconstrained and constrained samples heat treated at 700°C for three hours.

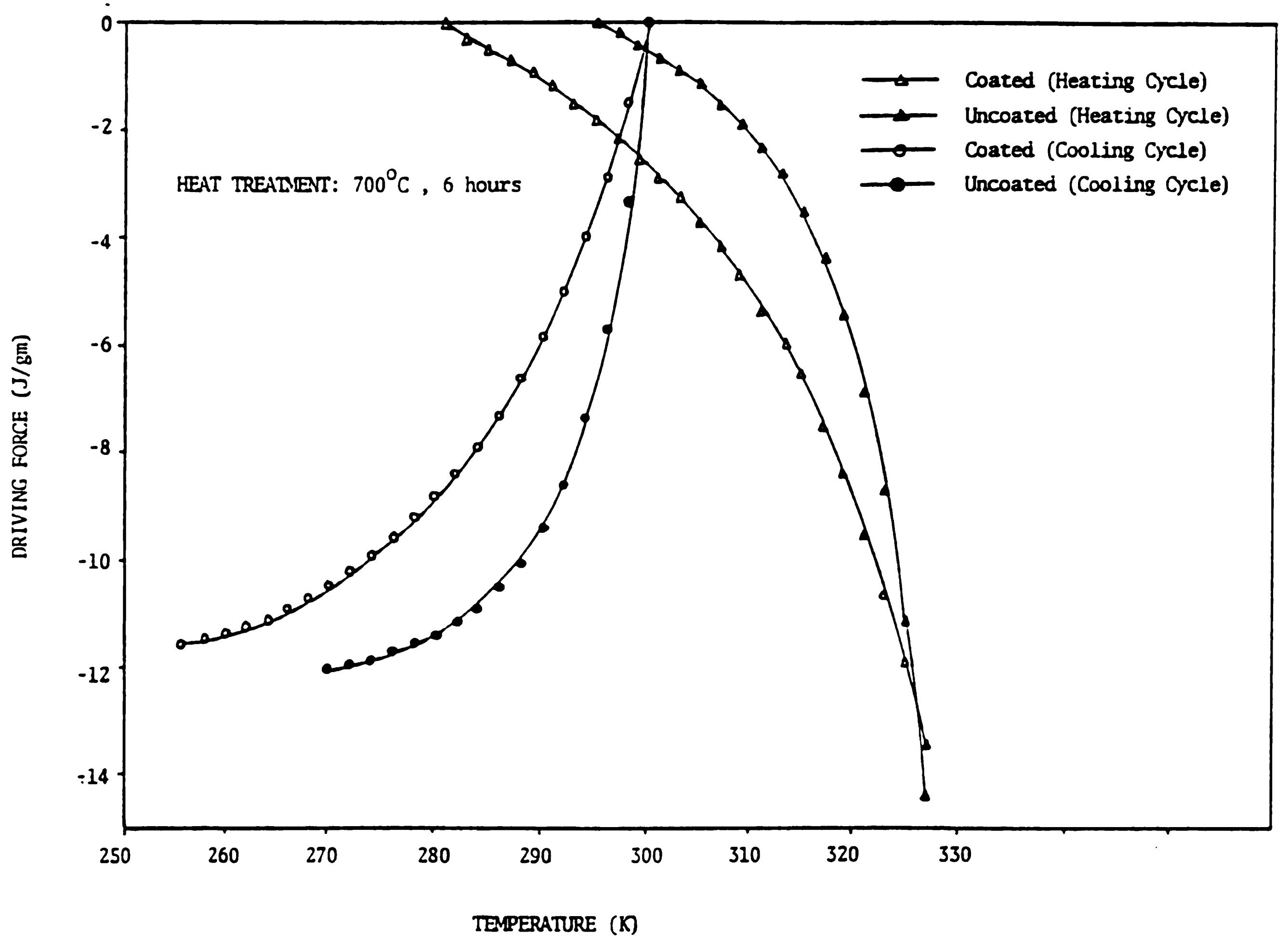

Figure 56. Driving force as a function of temperature for unconstrained and constrained samples that were heat treated at 700°C for six hours.

In the martensite to parent phase transformation, the A_s temperature for the surface constrained sample is lower than that of the unconstrained one. This is attributed to the fact that there is an increased amount of strain energy associated with the surface constrained sample during the martensitic transformation. Release of this stored energy assists in the reverse transformation causing it to start earlier, i.e. at a lower temperature. Thus, the driving force is greater in the constrained sample in the reverse transformation as compared to the unconstrained one at any temperature during the reverse transformation. Since the accommodation strain is largest for the martensite plates formed near the constrained surface, the reverse transformation of the surface constrained sample starts at or near the surface and proceeds to the bulk with the increase in temperature.

Finally, the strain energy associated with the surface constraint of the Nitinol samples could be estimated. Figures 55 and 56 show the differences in the driving force between the unconstrained and constrained samples at a given temperature during martensitic and reverse transformations. This difference corresponds to the strain energy contributed by the surface constraint. Although the strain energy is a function of temperature, it can be estimated that the maximum stored elastic energy difference between an unconstrained and a constrained (thin Nitinol sample) is estimated to be 3.5 J/gm.

B. Design of a Prosthesis for the Reconstruction of the Anterior Cruciate Ligament

Scanning electron microscopy figures of the harvested carbon coated filaments showed that islands of reticular collagen formed on their surface thirty days post-operative. However, the biological findings are inconclusive at that early stage, and additional research is required. The research should include a simple design of a prosthesis for the reconstruction of the anterior cruciate ligament in which the carbon coated Nitinol filaments are easily anchored to the tibia and femur.

The design envisioned, which should be modified as research progresses, uses the unique characteristic of Nitinol to change its shape with temperature. The Nitinol alloy chosen should have an austenitic finish temperature of about 35^{o}C, which is below the body temperature. Figure 57 shows the proposed design of the prosthesis. It is illustrated how one prosthesis has the ends deflected to illustrate the anchoring position with the tibia and femur when the Nitinol transforms with body temperature.

The components of the prosthesis are illustrated in Figure 58. It consists of two hollow cylindrical ends connected with the carbon coated filaments. There are two upset horizontal pins in each hollow end. The lower one is for the filament attachment, while the upper one is for surgical handling while pulling the ends of the prosthesis through the bones.

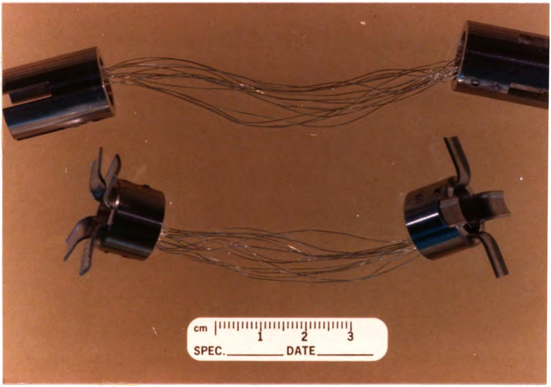

Figure 57. Proposed design of a carbon coated Nitinol prosthesis for the reconstruction of the anterior cruciate ligament.

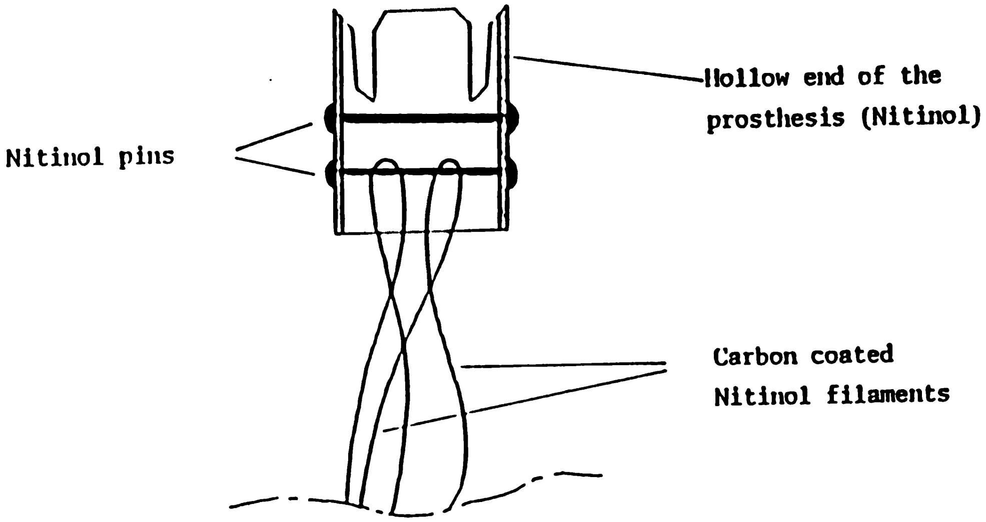

Figure 58. Design details of the prosthesis devised for the reconstruction of the anterior cruciate ligament.

Figures 59 and 60 (a) and (b) illustrate the method by which the prosthesis will be presented into the knee joint. Following drilling tunnels in the condyles of the tibia and femur, a flexible scale will be introduced to measure the distance between the surfaces of the tibia and the femur at the tunnel outlets (Figure 59). The prosthesis of the desired length, which will be kept at low temperatures prior to its use, will then be introduced in the knee joint. To avoid transformation of the Nitinol prosthesis, the knee will be cooled well below body temperature by ice packs. Figure 60 (a) shows the prosthesis in the untransformed configuration. The ice packs will be removed from around the knee allowing it to warm to body temperature, which will in turn heat the Nitinol prosthesis. Both ends of the prosthesis will deflect, and the anchoring of it to the tibia and femur is complete (Figure 60 (b)).

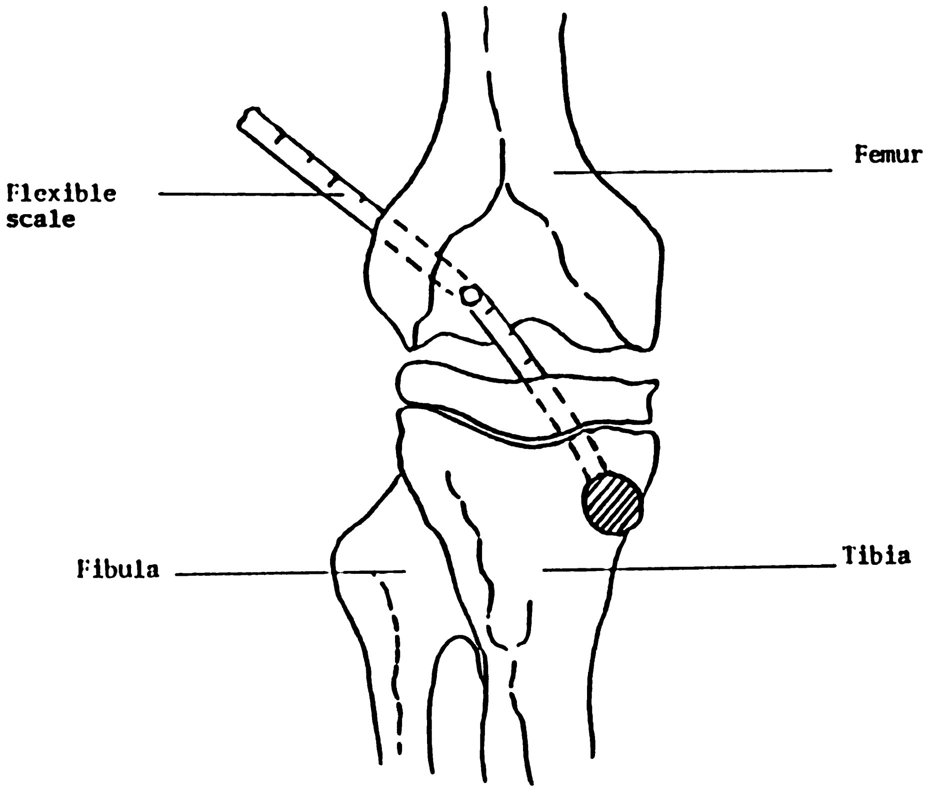

Figure 59. Illustration of a measuring device to measure the lengths between the surfaces of the tibia and femur.

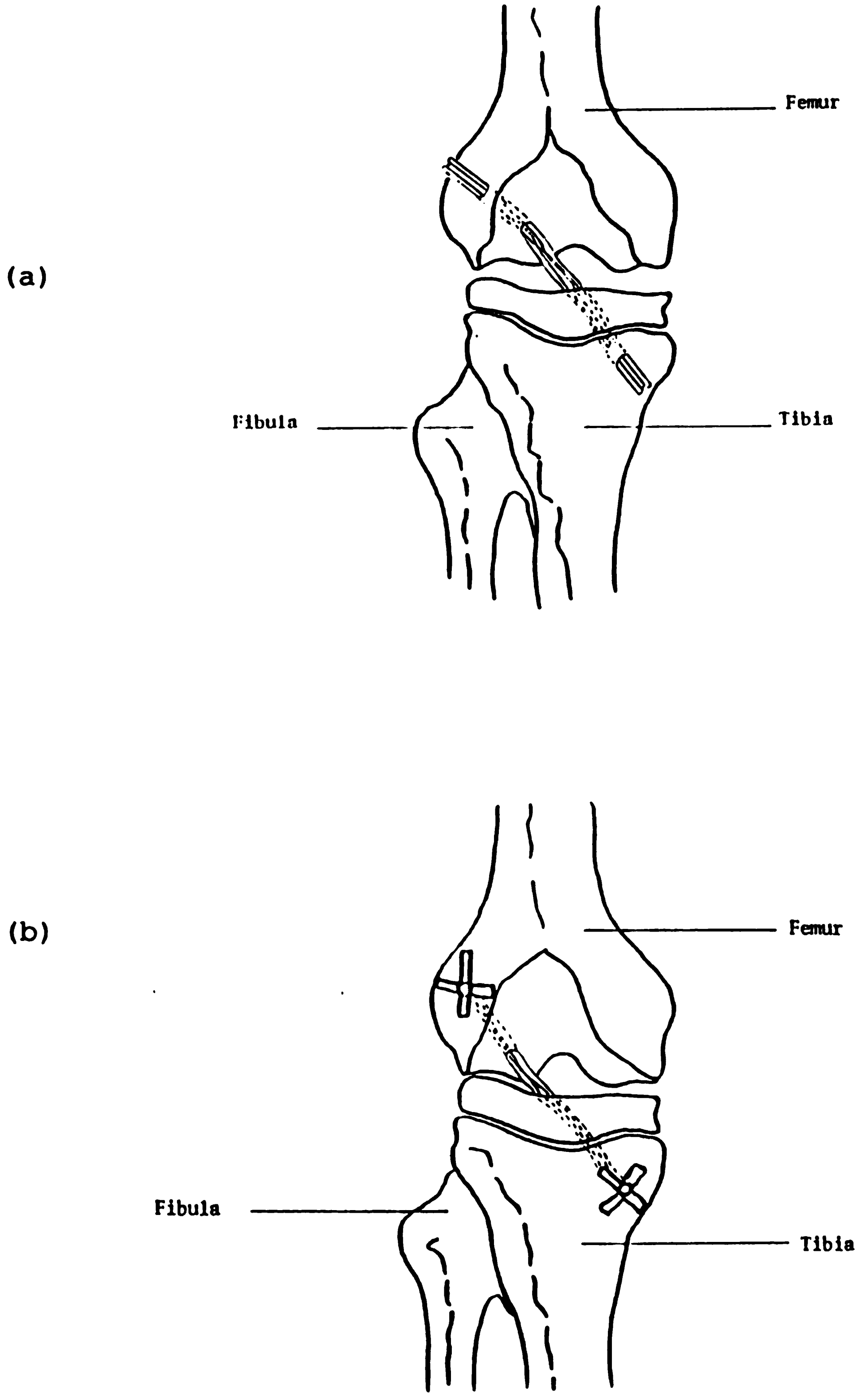

Figure 60. Prosthesis in the knee joint (a) before transformation (b) after transformation.

VI. CONCLUSIONS

1. Surface constraint of Nitinol results in marked drop in the A_s and M_f temperatures for thin samples.

2. Unannealed coatings did not inhibit the NiTi phase transformation regardless of the thickness of the coatings.

3. The carbon coating did not change the topography of the Nitinol surface.

4. TiC forms at the carbon/TiNI interface with annealing, and the thickness increases with the time of heat treatment.

5. The inhibition of the martensitic transformation increases as the thickness of the TiC interface increases.

6. The thicker the TiC interface was, the more the R-phase was inhibited during the martensitic transformation.

7. It is proposed that for surface constrained samples, the martensite plates last to form were close to the surface, and these are first to disappear during reverse transformation.

8. The forward transformation can be described by an equation of the form

$$1 - f = A \exp(-B(M_S - T))$$

where A and B can be defined by thermodynamic parameters.

9. The net driving force for the constrained sample was lower in the martensitic transformation compared to that of the unconstrained sample. The opposite is true for the reverse transformation.

10. The maximum stored elastic energy difference between an unconstrained and a constrained (thin Nitinol sample) is estimated to be 3.5 J/gm.

APPENDICES

APPENDIX 1

Experimental and Calculated Data for the Percentage of Austenite Present as a Function of Temperature for Uncoated Nitinol Samples Heat Treated at 700°C for Three Hours, and Carbon Coated Nitinol Samples Heat Treated at 700°C for Three Hours After Coating.

TABLE 1

Unconstrained Nitinol Sample - First Cooling Cycle

T(K)	% Austenite (Experimental)	% Austenite (Calculated*)
299.5	100	115
298.5	95	97
298.05	90	90
297.2	80	78
296.5	70	69
295.9	60	62
294.7	50	51
293.5	40	41
291.7	30	30
288.7	20	18
285.3	10	10
281.8	5	5
271.0	0	1

* % Austenite = $100\ (1-f) = 100 \times 1.15 \exp[-0.17(299.5-T)]$.

TABLE 2

Constrained Nitinol Sample - First Cooling Cycle

T(K)	% Austenite (Experimental)	% Austenite (Calculated*)
299.5	100	105
297.6	90	87
296.8	80	80
296.0	70	74
294.6	60	64
293.0	50	52
290.8	40	42
286.2	30	28
281.0	20	17
273.0	10	8
268.0	5	5
261.0	0	2

* % Austenite = $100\ (1-f) = 100 \times 1.05 \exp[-0.1(299.5-T)]$.

Table 3

Unconstrained Nitinol Sample - First Heating Cycle

T(K)	% Austenite (Experimental)	% Austenite (Calculated*)
327	100	115
326.3	95	103
325.7	90	94
324.7	80	81
323.7	70	70
322.8	60	61
321.7	50	52
320.2	40	41
318.3	30	31
315.5	20	20
311.05	10	10
307.1	5	6
296	0	1

* % Austenite = $100 \times f = 100 \times 1.15 \exp[-0.15(327-T)]$.

Table 4

Constrained Nitinol Sample - First Heating Cycle

T(K)	% Austenite (Experimental)	% Austenite (Calculated*)
327	100	105
325.4	90	90
324.3	80	81
323.2	70	73
322.1	60	66
320.2	50	55
317.4	40	42
313.1	30	28
306.6	20	15
297.7	10	7
292.3	5	4
281.0	0	1

* % Austenite = $100 \times f = 100 \times 1.05 \exp[-0.095(327-T)]$.

APPENDIX 2

Experimental and Calculated Data for the Percentage of Austenite Present as a Function of Temperature for Uncoated Nitinol Samples Heat Treated at 700°C for Six Hours, and Carbon Coated Nitinol Samples Heat Treated at 700°C for Six Hours After Coating.

Table 1

Unconstrained Nitinol Sample - First Cooling Cycle

T(K)	% Austenite (Experimental)	% Austenite (Calculated*)
299.5	100	110
298.7	90	95
297.8	80	81
297.0	70	70
296.3	60	62
295.3	50	51
294.0	40	41
292.2	30	30
290.2	20	20
287.7	10	13
285.8	5	9
271.0	0	1

* % Austenite = $100 \times (1-f) = 100 \times 1.1 \exp[-0.18(299.5-T)]$.

Table 2

Constrained Nitinol Sample - First Cooling Cycle

T(K)	% Austenite (Experimental)	% Austenite (Calculated*)
299.5	100	110
296.9	90	90
295.7	80	83
293.9	70	72
291.3	60	59
288.5	50	48
285.2	40	38
281.4	30	28
276.7	20	20
270.7	10	12
266.3	5	9
255.0	0	4

* % Austenite = $100(1-f) = 100 \times 1.1 \exp[-0.075(299.5-T)]$.

Table 3

Unconstrained Nitinol Sample - First Heating Cycle

T(K)	% Austenite (Experimental)	% Austenite (Calculated*)
327.0	100	115
326.7	95	110
325.5	90	92
324.5	80	79
323.5	70	68
322.6	60	59
321.4	50	50
319.9	40	40
318.1	30	30
315.9	20	22
312.7	10	13
310.3	5	9
296.0	0	1

* % Austenite = $100 \times f = 100 \times 1.15 \exp[-0.15(327-T)]$.

Table 4

Constrained Nitinol Sample - First Heating Cycle

T(K)	% Austenite (Experimental)	% Austenite (Calculated*)
327.0	100	105
326.0	95	98
324.8	90	90
323.0	80	79
321.3	70	70
319.6	60	62
316.4	50	50
313.0	40	39
308.3	30	28
303.8	20	21
297.4	10	13
293.1	5	10
281.0	0	4

* % Austenite = 100 x f = 100 x 1.05 exp [-0.07(327-T)].

APPENDIX 3

Driving Force of Phase Transformation as a Function of Temperature for Uncoated Nitinol Samples Heat Treated at 700°C for Three Hours, and Carbon Coated Nitinol Samples Heat Treated at 700°C for Three Hours After Coating.

Table 1

Unconstrained Nitinol Sample - First Cooling Cycle

T (K)	$\frac{e^{a_1 T}}{T}$	$\int_T^{M_s} \frac{e^{a_1 T}}{T}\,dT$	ΔG (J/gm)
299.5	4.32×10^{19}	0	0
297.5	3.09×10^{19}	4.32×10^{19}	- 3.25
295.5	2.22×10^{19}	7.41×10^{19}	- 5.59
293.5	1.59×10^{19}	9.63×10^{19}	- 7.27
291.5	1.13×10^{19}	11.2×10^{19}	- 8.52
289.5	8.16×10^{18}	12.35×10^{19}	- 9.4
287.5	5.85×10^{18}	13.16×10^{19}	-10.07
285.5	4.19×10^{18}	13.75×10^{19}	-10.66
283.5	3.00×10^{18}	14.17×10^{19}	-10.94
281.5	2.15×10^{18}	14.47×10^{19}	-11.22
279.5	1.54×10^{18}	14.68×10^{19}	-11.47
277.5	1.10×10^{18}	14.83×10^{19}	-11.66
275.5	7.94×10^{18}	14.94×10^{19}	-11.83
273.5	5.69×10^{18}	15.02×10^{19}	-11.95
271.5	4.08×10^{18}	15.08×10^{19}	-12.08

$\Delta H_T = 23.8$ J/gm

$a_1 = 0.17\ K^{-1}$

$K_1 = 4.65$ J/gm.K

Table 2

Constrained Nitinol Sample - First Cooling Cycle

T (K)	$\frac{e^{a_1 T}}{T}$	$\int_T^{M_s} \frac{e^{a_1 T}}{T} dT$	ΔG (J/gm)
299.5	3.39×10^{10}	0	0
297.5	2.79×10^{10}	3.39×10^{10}	- 1.86
295.5	2.3×10^{10}	6.18×10^{10}	- 3.36
293.5	1.9×10^{10}	8.48×10^{10}	- 4.61
291.5	1.56×10^{10}	10.38×10^{10}	- 5.63
289.5	1.29×10^{10}	11.94×10^{10}	- 6.52
287.5	1.06×10^{10}	13.23×10^{10}	- 7.24
285.5	0.87×10^{10}	14.29×10^{10}	- 7.84
283.5	0.72×10^{10}	15.16×10^{10}	- 8.36
281.5	0.59×10^{10}	15.88×10^{10}	- 8.79
279.5	0.49×10^{10}	16.47×10^{10}	- 9.16
277.5	0.40×10^{10}	16.96×10^{10}	- 9.48
275.5	0.33×10^{10}	17.36×10^{10}	- 9.76
273.5	0.27×10^{10}	17.69×10^{10}	- 9.99
271.5	0.22×10^{10}	17.96×10^{10}	-10.20
269.5	0.18×10^{10}	18.18×10^{10}	-10.40
267.5	0.15×10^{10}	18.36×10^{10}	-10.56
265.5	0.12×10^{10}	18.51×10^{10}	-10.72
263.5	0.10×10^{10}	18.63×10^{10}	-10.85
261.5	0.087×10^{10}	18.73×10^{10}	-10.98

$\Delta H_T = 21.38$ J/gm

$a_1 = 0.1$ K^{-1}

$K_1 = 2.24$ J/gm.K

Table 3

Unconstrained Nitinol Sample - First Heating Cycle

T (K)	$\frac{e^{a_1 T}}{T}$	$\int_{T}^{A_f} \frac{e^{a_1 T}}{T} dT$	ΔG (J/gm)
327	6.13 x 10^{18}	0	-14.18
325	4.57 x 10^{18}	6.13 x 10^{18}	-11.01
323	3.40 x 10^{18}	10.7 x 10^{18}	- 8.61
321	2.53 x 10^{18}	14.1 x 10^{18}	- 6.78
319	1.89 x 10^{18}	16.63 x 10^{18}	- 5.4
317	1.41 x 10^{18}	18.52 x 10^{18}	- 4.33
315	1.05 x 10^{18}	19.93 x 10^{18}	- 3.05
313	0.78 x 10^{18}	20.98 x 10^{18}	- 2.82
311	0.58 x 10^{18}	21.76 x 10^{18}	- 2.28
309	0.436 x 10^{18}	22.34 x 10^{18}	- 1.86
307	0.325 x 10^{18}	22.776 x 10^{18}	- 1.49
305	0.242 x 10^{18}	23.101 x 10^{18}	- 1.17
303	0.181 x 10^{18}	23.343 x 10^{18}	- 0.90
301	0.134 x 10^{18}	23.524 x 10^{18}	- 0.65
279	0.0865 x 10^{18}	23.658 x 10^{18}	- 0.42
297	0.075 x 10^{18}	23.73 x 10^{18}	- 0.19
295	0.056 x 10^{18}	23.808 x 10^{18}	0

ΔH_T = 24.53 J/gm

a_1 = 0.15 K^{-1}

K_1 = 4.23 J/gm.K

Table 4

Constrained Nitinol Sample - First Heating Cycle

T (K)	$\frac{e^{a_1 T}}{T}$	$\int_T^{A_f} \frac{e^{a_1 T}}{T} dT$	ΔG (J/gm)
327	9.48×10^{10}	0	-13.72
325	7.88×10^{10}	9.48×10^{10}	-11.78
323	6.56×10^{10}	17.36×10^{10}	-10.17
321	5.46×10^{10}	23.92×10^{10}	- 8.8
319	4.54×10^{10}	29.38×10^{10}	- 7.64
317	3.78×10^{10}	33.92×10^{10}	- 6.66
315	3.14×10^{10}	37.7×10^{10}	- 5.82
313	2.62×10^{10}	40.84×10^{10}	- 5.1
311	2.18×10^{10}	43.46×10^{10}	- 4.47
309	1.81×10^{10}	45.64×10^{10}	- 3.92
307	1.51×10^{10}	47.45×10^{10}	- 3.47
305	1.25×10^{10}	48.96×10^{10}	- 3.03
303	1.04×10^{10}	50.21×10^{10}	- 2.65
301	0.871×10^{10}	51.25×10^{10}	- 2.31
299	0.725×10^{10}	52.121×10^{10}	- 2.01
297	0.603×10^{10}	52.846×10^{10}	- 1.72
295	0.502×10^{10}	53.449×10^{10}	- 1.47
293	0.418×10^{10}	53.951×10^{10}	- 1.23
291	0.348×10^{10}	54.369×10^{10}	- 0.98
289	0.290×10^{10}	54.71×10^{10}	- 0.78
287	0.241×10^{10}	55.00×10^{10}	- 0.57
285	0.201×10^{10}	55.248×10^{10}	- 0.37

TABLE 4 - (continued)

T (K)	$\frac{e^{a_1 T}}{T}$	$\int_T^{A_f} \frac{e^{a_1 T}}{T} dT$	ΔG (J/gm)
283	0.167×10^{10}	55.449×10^{10}	- 0.19
281	0.139×10^{10}	55.616×10^{10}	0

ΔH_T = 22.37 J/gm

a_1 = 0.095 K^{-1}

K_1 = 2.23 J/gm.K

APPENDIX 4

Driving Force of Phase Transformation as a Function of Temperature for Uncoated Nitinol Samples Heat Treated at 700°C for Six Hours, and Carbon Coated Nitinol Samples Heat Treated at 700°C for Six Hours After Coating.

Table 1

Unconstrained Nitinol Sample - First Cooling Cycle

T (K)	$\frac{e^{a_1 T}}{T}$	$\int_T^{M_s} \frac{e^{a_1 T}}{T} dT$	ΔG (J/gm)
299.5	8.63×10^{20}	0	0
297.5	6.06×10^{20}	8.63×10^{20}	- 3.35
295.5	4.26×10^{20}	14.69×10^{20}	- 5.71
293.5	2.99×10^{20}	18.95×10^{20}	- 7.39
291.5	2.10×10^{20}	21.94×10^{20}	- 8.59
289.5	1.47×10^{20}	24.04×10^{20}	- 9.44
287.5	1.037×10^{20}	25.51×10^{20}	-10.07
285.5	0.729×10^{20}	26.547×10^{20}	-10.55
283.5	0.512×10^{20}	27.276×10^{20}	-10.9
281.5	0.360×10^{20}	27.788×10^{20}	-11.18
279.5	0.252×10^{20}	28.148×10^{20}	-11.39
277.5	0.177×10^{20}	28.4×10^{20}	-11.59
275.5	0.124×10^{20}	28.577×10^{20}	-11.72
273.5	0.0877×10^{20}	28.701×10^{20}	-11.87
271.5	0.0616×10^{20}	28.7887×10^{20}	-11.99
269.5	0.0433×10^{20}	28.8503×10^{20}	-12.11

$\Delta H_T = 24.71$ J/gm

$a_1 = 0.18\ K^{-1}$

$K_1 = 4.89$ J/gm.K

Table 2

Constrained Nitinol Sample - First Cooling Cycle

T (K)	$\frac{e^{a_1 T}}{T}$	$\int_T^{M_s} \frac{e^{a_1 T}}{T} dT$	ΔG (J/gm)
299.5	19.00×10^6	0	0
297.5	16.47×10^6	19.00×10^6	- 1.54
295.5	14.27×10^6	35.47×10^6	- 2.85
293.5	12.36×10^6	49.74×10^6	- 4.0
291.5	10.71×10^6	62.1×10^6	- 5.0
289.5	9.28×10^6	72.81×10^6	- 5.87
287.5	8.05×10^6	82.09×10^6	- 6.64
285.5	6.97×10^6	90.14×10^6	- 7.3
283.5	6.04×10^6	97.11×10^6	- 7.88
281.5	5.24×10^6	103.15×10^6	- 8.38
279.5	4.54×10^6	108.39×10^6	- 8.83
277.5	3.93×10^6	112.93×10^6	- 9.23
275.5	3.41×10^6	116.86×10^6	- 9.59
273.5	2.96×10^6	120.27×10^6	- 9.9
271.5	2.56×10^6	123.23×10^6	-10.18
269.5	2.22×10^6	125.79×10^6	-10.43
267.5	1.93×10^6	128.01×10^6	-10.66
265.5	1.67×10^6	129.94×10^6	-10.86
263.5	1.45×10^6	131.61×10^6	-11.05
261.5	1.25×10^6	133.06×10^6	-11.23
259.5	1.09×10^6	134.31×10^6	-11.38

Table 2 (continued)

T (K)	$\frac{e^{a_1 T}}{T}$	$\int_{T}^{M_s} \frac{e^{a_1 T}}{T} dT$	ΔG (J/gm)
257.5	0.94×10^6	135.4×10^6	-11.53
255.5	0.82×10^6	136.34×10^6	-11.66

$\Delta H_T = 22.27$ J/gm

$a_1 = 0.075\ K^{-1}$

$K_1 = 1.63$ J/gm.K

Table 3

Unconstrained Nitinol Sample - First Heating Cycle

T (K)	$\frac{e^{a_1 T}}{T}$	$\int_T^{A_f} \frac{e^{a_1 T}}{T} dT$	ΔG (J/gm)
327	6.13×10^{18}	0	-14.39
325	4.57×10^{18}	6.13×10^{18}	-11.16
323	3.4×10^{18}	10.7×10^{18}	- 8.73
321	2.53×10^{18}	14.1×10^{18}	- 6.89
319	1.89×10^{18}	16.63×10^{18}	- 5.48
317	1.41×10^{18}	18.52×10^{18}	- 4.30
315	1.05×10^{18}	19.93×10^{18}	- 3.54
313	0.78×10^{18}	20.98×10^{18}	- 2.88
311	0.58×10^{18}	21.76×10^{18}	- 2.32
309	0.436×10^{18}	22.34×10^{18}	- 1.88
307	0.325×10^{18}	22.776×10^{18}	- 1.5
305	0.242×10^{18}	23.101×10^{18}	- 1.19
303	0.181×10^{18}	23.343×10^{18}	- 0.91
301	0.134×10^{18}	23.524×10^{18}	- 0.65
299	0.0865×10^{18}	23.658×10^{18}	- 0.41
297	0.075×10^{18}	23.73×10^{18}	- 0.18
295	0.056×10^{18}	23.808×10^{18}	0

ΔH_T = 24.92 J/gm

a_1 = 0.15 K^{-1}

K_1 = 4.29 J/gm.K

Table 4

Constrained Nitinol Sample - First Heating Cycle

T (K)	$\frac{e^{a_1 T}}{T}$	$\int_T^{A_f} \frac{e^{a_1 T}}{T} dT$	ΔG (J/gm)
327	26.69×10^6	0	-13.44
325	23.35×10^6	26.69×10^6	-11.92
323	20.42×10^6	50.04×10^6	-10.59
321	17.86×10^6	70.46×10^6	- 9.45
319	15.63×10^6	88.32×10^6	- 8.41
317	13.67×10^6	103.95×10^6	- 7.47
315	11.96×10^6	117.62×10^6	- 6.51
313	10.46×10^6	129.58×10^6	- 5.92
311	9.15×10^6	140.04×10^6	- 5.27
309	8.01×10^6	149.19×10^6	- 4.67
307	7.01×10^6	157.2×10^6	- 4.13
305	6.13×10^6	164.21×10^6	- 3.65
303	5.36×10^6	170.34×10^6	- 3.2
301	4.69×10^6	175.7×10^6	- 2.8
299	4.11×10^6	180.39×10^6	- 2.51
297	3.59×10^6	184.5×10^6	- 2.09
295	3.15×10^6	188.09×10^6	- 1.77
293	2.75×10^6	191.24×10^6	- 1.47
291	2.41×10^6	193.99×10^6	- 1.19
289	2.11×10^6	196.4×10^6	- 0.92
287	1.84×10^6	198.57×10^6	- 0.67
285	1.61×10^6	200.35×10^6	- 0.44

Table 4 (continued)

T (K)	$\frac{e^{a_1 T}}{T}$	$\int_T^{A_f} \frac{e^{a_1 T}}{T} dT$	ΔG (J/gm)
283	1.41×10^6	201.96×10^6	- 0.22
281	1.24×10^6	203.37×10^6	0

ΔH_T = 22.27 J/gm

a_1 = 0.07 K^{-1}

K_1 = 1.63 J/gm.K

BIBLIOGRAPHY

1. Mukherjee, K., "Shape-Memory-Effect Alloys: Biomedical Applications." In, Encyclopedia of Materials Science and Engineering, ed. Michael Bever, New York: Pergamon Press, 1986.

2. Castleman, L.S., and S.M. Motzkin, "The Biocompatibility of Nitinol." In, Biocompatibility of Clinical Implant Materials, ed. David Williams, Florida: CRC Press, 1981.

3. Jenkins, D.H.R., "The Repair of Cruciate Ligaments with Flexible Carbon Fiber." J. Bone J. Surg., V.60B, (1978): 520.

4. Jenkins, D.H.R., Forester, I.W., McKibbins, B., and Z.A. Ralis, "Induction of Tendon and Ligament Formation by Carbon Implants." J. Bone J. Surg., V.59B, (1977): 53.

5. Walker, D., Fitzer, E., Helbing, G., and J. Goldaway, "Ligament Replacement in the Knee Joint with Carbon Fibers Coated with Pyrolytic Carbon." Trans. 3rd Ann. Mtg. Soc. for Biomat., (1977): 126.

6. Neugebauer, R., Claes, L., Helbing, G., and D. Wolter, "The Replacement of the Abdiominal Wall by a Carbon Cloth in Rabbits." Trans. 5th Ann. Mtg. Soc. for Biomat., (1979): 135.

7. Neugebauer, R., Burri, C., Claes, L., Helbing, G., and D. Wolter, "The Anchorage of Carbon Fiber Strands into Bone; A Biomechanical and Biological Evaluation of Knee Joints." Trans. 2nd Mtg. European Soc. of Biomat., (1979).

8. Kennedy, J.C., "Application of Prosthetics to Anterior Cruciate Ligament Reconstruction and Repairs." Clin. Orthop. Rel. Res., V.175, (1983): 125-8.

9. Jenkins, D.H.R., "Carbon Fiber as a Prosthetic Implant Material in Orthopaedics." J. Bone J. Surg., V.58B, (1976): 253.

10. Jenkins, D.H.R., "Experimental and Clinical Application of Carbon Fiber as an Implant in Orthopaedics." J. Bone J. Surg., V.59B, (1977): 501.

11. Jenkins, D.H.R., "Ligamentous Induction of Filamentous Carbon Fiber." Surg. News, (1978): 6.

12. Rushton, N., et al., "The Clinical, Arthroscopic and Histological Findings After Replacement of the Anterior Cruciate Ligament with Carbon Fiber." J. Bone J. Surg., V.65B, (1983): 308.

13. Jenkins, G.H. and C.J Grigson, "The Fabrication of Artifacts out of Glassy Carbon and Carbon Fiber Reinforced Carbon for Biomedical Applications." J. Biomed. Mat. Res., V.13, (1979): 371.

14. Mukherjee, K., Sircar, S., and N. Dahotre, "Thermal Effects Associated with Stress-Induced Martensitic Transformation in a Ti-Ni Alloy." Mater. Sci. Engng., V.74, (1985): 75.

15. Halpern, A., The Runner's World Knee Book. New York: MacMillan Publishing Company, 1984.

16. Fetto, J., "Knee Lesions I." In, Ligament Injuries and Their Treatment, ed. D.H.R. Jenkins, England: Chapman and Hall Ltd., 1985

17. Reiman, P., and D. Jackson, "Anatomy of the Anterior Cruciate Ligament." In, The Anterior Cruciate Deficient Knee, ed. D. Jackson, and D. Drez, St. Louis: The C.V. Mosby Company, 1987.

18. Claes, L., "Biomechanical Properties of Human Ligaments." In, ed. C. Burri, and L. Claes, Bern: Hans Huber Publishers, 1983.

19. Forster, I., "Structural Aspects of Tendons and Ligaments." In, Natural and Living Biomaterials, ed. G. Hastings, and P. Ducheyne, Florida: CRC Press, Inc., 1984.

20. Ellison, A.E., "Distal Iliotibial Band Transfer for Anterior Lateral Rotary Instability of the Knee." J. Bone J. Surg., V.61A, (1979): 330.

21. Ireland, J. and E.L. Trickery, "Macintosh Tendesis for Anterior Instability of the Leg." J. Bone J. Surg.. V.62B, (1980): 340.

22. Jones, K.G., "Results of Use of the Central One Third of the patellar Ligament to Compensate for Anterior Cruciate Instability." Clin. Orthop. Relat. Res., V.147, (1980): 29.

23. Thomson, S.K., Calver, R., and C.J.E. Monk, "Anterior Cruciate Ligament Repair to Rotary Instability; the Lindemann Dynamic Muscle Transfer Procedure." J. Bone J. Surg., V.60A, (1978): 917.

24. Schulitz, H., Krahl, H., and W. Stein, "Late Reconstruction of Injured Ligaments of the Knee." New York: Springer-Verlag, 1978.

25. Leighton, R.L., "Repair of Ruptured Anterior Cruciate Ligament with Whole Thickness Skin." Vet. Med. Small Animal Clin., V.1, (1961): 246.

26. Marshall, J.L. and S.C. Olsson, "Instability of the Knee. A Long Term Experimental Study in Dogs." J. Bone J. Surg., V.53A, (1971): 1561.

27. Burks, R., Haut, R. and R. Lancaster, "Biomechanical and Histological Observations on the Dog Patellar After Removal of its Central One-Third." Am. J. Sp. Med., In Press.

28. Simon, T. and D. Jackson, "Anterior Cruciate Ligament Allografts." In, ed. D. Jackson, and D. Drez, St. Louis: The C.V. Mosby Company, 1987.

29. Chen, E.H. and J. Black, "Materials Design Analysis of Prosthetic Anterior Cruciate Ligament." J. Biomed. Mat. Res., V.14, (1980): 567.

30. Grood, E.S., "Cruciate Ligament Prosthesis: Strength, Creep and Fatigue Properties." J. Bone J. Surg., V.58A, (1976): 1083.

31. James, S.L., Woods, G.W., Housy, C.A., Prewitt, J.M., and D.B. Slocum, "Cruciate Ligament in Reconstruction of the Unstable Knee: A Preliminary Report." Clin. orthop. Rel. Res., V.143, (1970): 90.

32. Grood, E.S., et al., "Strength of the Anterior Cruciate LIgament in Human and Rhesus Monkeys." J. Bone J. Surg., V.58A, (1976): 1074.

33. Meyers, J.F., Grana, W.A., and R.A. Lesker, "Reconstruction of the Anterior Cruciate Ligament in the Dog; Comparison of Results Obtained with Three Different Porous Synthetic Materials." Am. J. Sports Med., V.7, (1979): 85.

34. Rubin, R.M., Marshall, J.L., and J. Wang, "Prevention of Knee Instability: Experimental Model for Prosthetic Anterior Cruciate Ligament." Clin. Orthop. Relat. Res., V.113, (1975): 212.

35. Fitzgerald, E.E., Chu, C.C., and D. Buchanan, "Mechanical Behavior of Bicomponent Braids as Potential Surgical Implants." In, Advances in Biomaterials, Vol. 3, ed. G.D. Winter, D.F. Gibbons, and H. Plank, New York: Wiley and Sons, 1982.

36. Trembley, G. and C. Laurin, "The Challenge of Prosthetic Cruciate Ligament." Clin. Orthop. Rel. Res., v.147, (9180): 88.

37. Bolton, C. and W. Bruchman, "The Gor-Tex Expanded Polytetrafluoroethylene Prosthetic Ligament." Clin. Orthop., V.196, (1985): 202-213.

38. Chen, E. and J. Black, "Materials Design Analysis of the Prosthetic Anterior Cruciate Ligament." J. Biomed. Mater. Res., V.14, (1980): 567-586.

39. Roth, J. and J. Kennedy, "Polypropylene-Braid-Augmented Anterior Cruciate Ligament Reconstruction." In, Prosthetic Ligament Reconstruction of the Knee, ed. M. Friedman and R. Ferkel, Philadelphia: W.B. Saunders Company, 1988.

40. Forster, I.W., Ralis, Z.A., McKibbin, B., and D.H.R. Jenkins, "Biological Reaction to Carbon Fiber Implants." Clin. Orthop. Rel. Res., V.131, (1978): 299.

41. Jenkins, G.H. and C.J. Grigson, "The Fabrication of Artifacts out of Glassy Carbon and Carbon Fiber Reinforced Carbon for Biomedical Applications." J. Biomed. Mat. Res., V.13, (1979): 371.

42. Weiss, A., et al., "Ligament Replacement with an Absorbable Copolymer Carbon Fiber Scaffold - Easy Clinical Experience." Clin. Orthop. Rel. Res., V.196, (1985): 77.

43. Claes, L., et al., "In Vivo and In Vitro Investigation of the Long-Term Behavior and Fatigue Strength of Carbon Fiber Ligament Replacement." Clin. Orthop. Rel. Res., V.196, (1985): 99.

44. Perkins, J., "Shape-Memory-Effect Alloys: Basic Principles." In, Encyclopedia of Materials Science and Engineering, ed. M. Bever, New York: Pergammon Press, 1986.

45. Wayman, C., "Phase Transformations, Nondiffusive." In, Physical Metallurgy, ed. R. Cahn and P. Haaser, Amsterdam: North-Holland Physics Publishing, 1983.

46. Wang, F., et al., "Crystal Structure and a Unique "Martensitic" Transition of NiTi." J. Appl. Phys., V.36, (1965): 3232.

47. Nishiyama, Z., "Martensitic Transformation." New York: Academic Press, 1978.

48. Porter, D. and K. Easterling, "Phase Transformations in Metals and Alloys." Berkshire: Van Nostrand Reinhold, 1981.

49. Wang, F., et al., "The Irreversible Critical Range in the TiNi Transition." J. Appl. Phy., V.39, (1968): 2166.

50. Wu, X. and T. Ko, "The Martensite and R-Phase in Ti-50.3 at % Ni Alloy." Proceedings of the International Conference on Martensitic Transformations (ICOMAT-86), Nara, Japan, August 26-30, 1986.

51. Sandrock, G., "Premartensitic Behavior of the Electrical Resistivity of NiTi." Metall. Trans., V.5, (1974): 299.

52. Sandrock, G., et al., "The Premartensitic Instability in Near-Equiatomic TiNi." Metall. Trans., V.2, (1971): 2769.

53. Tadaki, T., et al., "Thermal Cycling Effects in an Aged Ni-Rich Ti-Ni Shape Memory Alloy." Tran. Jap. Inst. Met., V.28, (1987): 883.

54. Chandra, K. and G. Purdy, "Observation of Thin Crystals of TiNi in Premartensitic States," J. App. Phys., V.39, (1986): 2176.

55. Otsuka, K., et al., "Crystall Structure and Internal Defects of Equiatomic TiNi Martensite." Physica Status Solidia., V.5, (1971): 457.

56. Wasilewski, R., "Elastic Modulus Anomaly in TiNi." Trans. AIME, V.233, (1965): 1691.

57. Hasiguti, R. and K. Iwasaki, "Internal Friction and Related Properties of the TiNi Intermetallic Compound." J. App. Phys., V.39, (1968): 2182.

58. Hanlon, J., et al., "Effect of Martensitic Transformation on the Electrical and Magnetic Properties of NiTi," Trans AIME, V.239, (1967): 1323.

59. Berman, H., et al., "Anomalous Heat Capacity of TiNi." J. App. Phys., V.38, (1967): 4473.

60. Dautovich, D., et al., "Calorimetric Study of a Diffusionless Phase Transition in TiNi." *J. App. Phys.*, V.38, (1967): 4473.

61. Hwang, C., et al., "Transformation Behaviour of a Ti_{50} Ni_{47} Fe_3 Alloy, I. Premartensitic Phenomena and the Incommensurate Phase." *Phil. Mag. A.*, V.47, (1983): 9.

62. Hwang, C., et al., "Transformation Behaviour of a Ti_{50} Ni_{47} Fe_3 Alloy, II. Subsequent Premartensitic Behaviour and the Commensurate Phase." *Phil. Mag. A.*, V.47, (1983): 31.

63. Goo, E. and R. Sinclair, "The B2 to R Transformation in Ti_{50} Ni_{47} Fe_3 and $Ti_{49.5}$ $Ni_{50.5}$ Alloys." *Acta. Met.*, V.33, (1985): 1717.

64. Wayman, C., "Phase Transformations in NiTi-Type Shape Memory Alloys." In, *Proceedings of the International Conference on Martensitic Transformations (ICOMAT-86)*, Nara, Japan, August 26-30, 1986.

65. Goldstein, D., "Nitinol Strain Effects." *Journal of Metals*, V.23, (1987).

66. Miyazaki, S. and C. Wayman, "The Shape Memory Mechanism Associated with the R-Phase Transition in TiNi Single Crystals." In, *Proceedings of the International Conference on Martensitic Transformations (ICOMAT-86)*, Nara, Japan, August 26-30, 1986.

67. Miyazaki, S. and C. Wayman, "The R-Phase Transition and Associated Shape Memory Mechanism in Ti-Ni Single Crystal." *Acta. Met.*, V.36, (1988): 181.

68. Schroeder, T. and C. Wayman, "The Formation of Martensite and the Mechanism of the Shape Memory Effect in Single Crystals of Cu-Zn Alloys." *Acta. Met.*, V.25, (1975): 1375.

69. Kaufman, L. and M. Cohen, "Thermodynamics and Kinetics of Martensitic Transformations." In, *Progress in Metal Physics*, ed. B. Chalmers and R. King, New York: Pergamon Press, 1958.

70. Tong, H. and C. Wayman, "Characteristic Temperature and Other Properties of Thermoelastic Martensites." *Acta. Met.*, V.22, (1974): 887.

71. Tong, H. and C. Wayman, "Thermodynamics of Thermoelastic Martensitic Transformations." *Acta. Met.*, V.23, (1975): 209.

72. Ahlers, M., et al., "Transformation Hardening and Energy Dissipation in Martensitic Beta-Brass." Mat. Sci. Eng., V.27, (1977): 49.

73. Perkins, J. and W. Muesing, "Martensitic Transformation Cycling Effects in Cu-Zn-Al Shape Memory Alloys." Met. Trans. A, V.14, (1983): 33.

74. Perkins, J., "Effects of Austenitic Microstructure on Martensitic Transformation in CuZnAl Shape Memory Alloys." J. dePhys., V.43, No. C-4, (1982): 697.

75. Johnson, W., et al., "P/M Processing and Characterization of Controlled Transformation Temperature NiTi." J. dePhys., V.43, No. C-4, (1982): 285.

76. Nishikawa, N., et al., "Behavior of Welded Part of TiNi Shape Memory Alloy." J. dePhys., V.43, No. C-4, (1982): 839.

77. Kwarciak, J., et al.. "Effect of Thermal Cycling and Ti_2Ni Precipitation on the Stability of the Ni-Ti Alloys." J. Mat. Sci., V.22, (1987): 2341.

78. Mercier, O. and K. Melton. "Theoretical and Experimental Efficiency of the Conversion of Heat into Mechanical Energy Using Shape-Memory Alloys." J. Appl. Phys., V.52, (1981): 1030.

79. Mercier, O. and K. Melton, "Kinetics and Thermodynamics of the Shape-Memory Effect in Martensitic NiTi and $(Ni_{1-x} - Cu_x)$ Ti Alloys." J. Appl. Phys., V.50, (1979): 5747.

80. Wasilewski, R., et al., "On Martensitic Transformation in TiNi." Metal Science J., V.1, (7/1967): 104.

81. Airoldi, G., et al., "Heats of Transformations as a Function of Thermal Cycling in NiTi Alloys." In, Proceedings of the International Conference on Martensitic Transformations (ICOMAT-86), Nora, Japan: August 26-30, 1986.

82. Salzbrenner, R., "Shape Memory Heat Engines." J. Mat. Sci., V.19, (1984): 1827.

83. Kwarciak, J. and H. Morawiec. "Some Interpretation Problems of Thermal Studies of the Reversible Martensitic Transformation." J. Mat. Sci., V.23 (1988): 551.

84. Guenin, G., et al., "Calorimetric Study on the Martensitic Transformation of CuZnAl Alloys." Proceedings of the International Conference on Martensitic Transformations (ICOMAT-86), Nara, Japan: August 26-30, 1986.

85. Salzbrenner, R. and M. Cohen, "On the Thermodynamics of Thermoelastic Martensitic Transformations." Acta. Met., V.27, (1979): 739.

86. Tadaki, T., et al., "Thermal Cycling Effects in an Aged Ni-Rich Ti-Ni Shape Memory Alloy." Trans. Jap. Inst. Met., V.28, (1987): 883.

87. Teer, D. and M. Salama, "The Ion Plating of Carbon." Thin Solid Films, V.45, (1977): 553.

88. Agarwal, N., et al., "Vacuum-Deposited Carbon Coatings." Thin Solid Films, V.40, (1977): 299.

89. Maissel, L.I. and R. Glang, Handbook of Thin Film Technology, New York: McGraw-Hill, 1970.

90. Susamu, F., et al., "Carbon Film Formation by Laser Evaporation and Ion Beam Sputtering." Thin Solid Films, V.92, (1982): 71.

91. Haubold, A., et al., "Carbon in Medical Devices." In, Biocompatibility of Clinical Implant Materials, ed. D. Williams, Florida: CRC Press, 1981.

92. Haubold, A., "Carbons for Biomedical Applications." In, Encyclopedia of Materials Science and Engineering, ed. Michael Beuer, New York: Pergamon Press, 1986.

93. Shim, H., et al., "The Adhesion of Thin Carbon Films to Metallic Substrates." J. Bioeng., V.1, (1976): 45.

94. Agarwal, N., et al., "Adhesion Characteristics of Thin Vacuum Deposited Carbon Films." Extended Abstracts, 13th Biennial Conference on Carbon, Irvine, California, July 18-22, 1977.

95. Foll, F., et al., "Cross-Sectional Transmission Electron Microscopy of Silicon-Silicide Interfaces." J. Appl. Phys., V.52, (1981): 250.

96. Sheng, T. and R. Marcus, "Advances in Transmission Electron Microscope Techniques Applied to Device Failure Analysis." J. Electrochem. Soc., V.127, (1980): 737.

97. The surgical procedure was summarized from: "Application to Use Vertebrate Animals for Research or Teaching." Michigan State University, East Lansing, Michigan, 1989.

98. Private communications with the performing orthopedic surgeon, Dr. Terrance Braden, Michigan State University, East Lansing, Michigan.

99. Private communications with Ms. Jane Walsh, Research Assistant I, Michigan State University, East Lansing, Michigan.

100. Mukherjee, K., "Thermodynamics and Kinetics of Martensitic Transformation." In, International Summer Course on Martensitic Transformations (ICOMAT-82), Leuven, Belgium: August 6-7, 1982.